

AD-A273 868



2

ARMY RESEARCH LABORATORY



# Dynamic Response of S-2 Glass Reinforced Plastic Structural Armor

## A Progress Report

Edited By  
Shun-Chin Chou and Eugenio DeLuca

ARL-SR-5

December 1993

**S** DTIC  
ELECTE  
DEC 17 1993  
**A**

120



93-30538

\*Original contains color  
plates: All DTIC reproduct-  
ions will be in black and  
white\*

Approved for public release; distribution unlimited.

93 12 16 029

**Best  
Available  
Copy**

The findings in this report are not to be construed as an official Department of the Army position unless so designated by other authorized documents.

Citation of manufacturer's or trade names does not constitute an official endorsement or approval of the use thereof.

Destroy this report when it is no longer needed. Do not return it to the originator.

REPORT DOCUMENTATION PAGE			Form Approved OMB No. 0704-0188	
Public reporting burden for this collection of information is estimated to average 1 hour per response, including the time for reviewing instructions, searching existing data sources, gathering and maintaining the data needed, and completing and reviewing the collection of information. Send comments regarding this burden estimate or any other aspect of this collection of information, including suggestions for reducing this burden, to Washington Headquarters Services, Directorate for Information Operations and Reports, 1215 Jefferson Davis Highway, Suite 1204, Arlington, VA 22202-4302, and to the Office of Management and Budget, Paperwork Reduction Project (0704-0188), Washington, DC 20503.				
1. AGENCY USE ONLY (Leave blank)		2. REPORT DATE December 1993		3. REPORT TYPE AND DATES COVERED Progress Report
4. TITLE AND SUBTITLE Dynamic Response of S-2 Glass Reinforced Plastic Structural Armor A Progress Report			5. FUNDING NUMBERS	
6. AUTHOR(S) Edited by Shun-Chin Chou and Eugenio DeLuca				
7. PERFORMING ORGANIZATION NAME(S) AND ADDRESS(ES) U.S. Army Research Laboratory Watertown, Massachusetts 02172-0001 ATTN: AMSRL-MA-PD			8. PERFORMING ORGANIZATION REPORT NUMBER  ARL-SR-5	
9. SPONSORING/MONITORING AGENCY NAME(S) AND ADDRESS(ES) U.S. Army Research Laboratory 2800 Powder Mill Road Adelphi, MD 20783-1197			10. SPONSORING/MONITORING AGENCY REPORT NUMBER	
11. SUPPLEMENTARY NOTES				
12a. DISTRIBUTION/AVAILABILITY STATEMENT Approved for public release; distribution unlimited.			12b. DISTRIBUTION CODE	
13. ABSTRACT (Maximum 200 words) This is a progress report on work conducted in FY93 to define the dynamic response of S-2 glass reinforced plastic laminate under ballistic loading. The work is divided into three parts, a description of ballistic impact damage in monolithic laminates produced by fragment simulators and measurement of target residual compressive strength, determination of material dynamic properties, and measurement and analysis of stress levels in glass reinforced plastic laminates under ballistic impact. Enlargement and extension of the data base constructed herein is planned for FY94. The overall objectives of this effort are to provide design guidelines for application of S-2 glass reinforced plastic in vehicular structures and to define the dynamic behavior of this material for general applications in armor technology.				
14. SUBJECT TERMS Composite material, Dynamic properties, Ballistics, Modeling, Simulation, Delamination			15. NUMBER OF PAGES 120	
			16. PRICE CODE	
17. SECURITY CLASSIFICATION OF THIS REPORT Unclassified	18. SECURITY CLASSIFICATION OF THIS PAGE Unclassified	19. SECURITY CLASSIFICATION OF ABSTRACT Unclassified	20. LIMITATION OF ABSTRACT UL	

# CONTENTS

	PAGE
1. INTRODUCTION AND SCOPE.....	1
2. BALLISTIC IMPACT DAMAGE EVALUATION.....	3
J. Prifti, E. DeLuca, and W. Bethoney	
a. Ballistic Impact Experiments.....	3
b. Computed Tomography Analysis of Delamination .....	5
c. Compressive Strength After Ballistic Impact .....	28
d. Rear Surface Transient Displacement .....	32
e. Summary of Results.....	37
3. DYNAMIC CHARACTERIZATION.....	39
D. P. Dandekar, J. L. Green, and P. Beaulieu	
a. Background .....	39
b. Elastic Constants.....	41
c. Quasi-Static and Medium Strain Rate Tensile and Compressive Properties .....	49
d. High Strain Rate Compression in the Thickness Direction.....	58
e. Summary .....	60
f. Future Work.....	61
4. STRESS WAVE EXPERIMENT AND ANALYSIS UNDER BALLISTIC CONDITIONS .....	63
A. Rajendran, D. Kokidko, and B. Durant	
a. Background .....	63
b. Test Method.....	63
c. Instrumentation and Data Acquisition.....	64
d. Test Results.....	64
e. Preliminary Analysis.....	65
5. SUMMARY OF RESULTS AND FUTURE WORK.....	75
6. APPENDIX .....	79

DISC (CONTINUED) REFLECTED 1

For	
A&I	<input checked="" type="checkbox"/>
ed	<input type="checkbox"/>
on/	
Availability Codes	
Dist	Avail and/or Special
A-1	

## 1. INTRODUCTION AND SCOPE

Since the development of nylon fiber in the 1930's and the inception of flak vests during World War II, the technical community has endeavored to extend the use of high strength, light weight fibers in protective armor. The first use of glass fiber-reinforced plastic (GRP) for armor applications occurred with development of Doron, a laminate of fiberglass and polyester resin, which was employed by the U.S. Marines in their fragmentation vest during the Korean conflict. During the 1960's Goodyear Aerospace in concert with Army engineers discovered that ceramics backed by glass-reinforced plastic results in a weight efficient armor system for stopping armor piercing bullets. More extensive use of fibers and reinforced plastics as armor components occurred with development of the high tenacity fiber Kevlar by Dupont. This led to development of a Kevlar based fragmentation vest and helmet under the PASGT (Personnel Armor Systems for Ground Troops) program conducted by NRDEC and ARL. The utilization of Kevlar was extended to spall liners within the M113 APC and Bradley Fighting Vehicles; most recently S2 glass-reinforced plastics have been accepted for liner applications.

It is most important to note that all fiber and fiber-reinforced plastic armor applications to date have been non load-bearing items or components. With the consideration of glass-reinforced plastic composites for combat vehicle hulls it is imperative that the structural integrity and dynamic response of these composites during and following ballistic impact be determined. The GRP composite systems investigated in this report consist of multiple layers of S2 glass fabric impregnated with Cycom 4102 polyester resin (32% by weight). This GRP laminate system has been employed by ARL/MD for fabrication of the composite hull of Bradley type and a 55 ton prototype composite hull vehicle. This fiber-resin composite system was found to possess the optimal combination of strength and ballistic performance of a glass fiber system. The strength is dependent on the mechanical properties of the S2 glass fiber and strong bonding to the resin, while the ballistic performance favors a relatively weak bond between the glass fiber and the resin. A weak bond allows the fibers to break away from the resin allowing subsequent extension of the fibers thereby utilizing the fibers high tensile and elongation properties. Therefore for GRP structural armor there is always a trade-off between structural strength and ballistic performance.

To date only limited data has been generated to describe the dynamic response, damage, and residual strength of thick GRP laminates due to ballistic loading. This investigation is a first attempt to provide full understanding of the dynamic response of GRP laminates subjected to projectile (fragment) impact and to measure damage and residual compressive strength of laminates after ballistic impact. The report is divided into three chapters that deal, in-turn, with evaluation of ballistic impact damage, material dynamic properties, and combined experimental/computational analysis of stress wave profiles generated by ballistic impact.

The objectives of the first chapter are to describe and quantify ballistic impact damage experienced by S-2 glass-reinforced plastic laminate panels, to measure laminate strength after ballistic impact, and to explore correlation of residual strength with ballistic impact and/or damage parameters. The following chapter describes experiments and procedures to determine certain mechanical properties of the GRP material that include a full set of elastic constants, quasi-static and medium strain rate tensile and compressive properties, and through-thickness, compressive stress-strain data at high strain rate. These properties are required not only for complete characterization of the material but, more important, as input to analytical and computational methods for modeling the dynamic response and behavior of GRP. The final chapter describes a combined experimental and computational approach for predicting stress profiles in thick GRP laminates resulting from fragment ballistic impact. The primary objective of this chapter is to use experimentally measured stress profiles in the GRP laminate to calibrate and verify mathematical simulations of shock/stress transmission through the laminate; this is an important step towards development of an accurate methodology for prediction of GRP response under ballistic impact.

The laminates used throughout this work are identical in composition and construction to S-2 glass fabric-reinforced plastic material used in the prototype combat hulls designed and built by FMC for ARL. The GRP laminates were made up of S-2 glass woven roving in a polyester resin matrix with resin content  $32 \pm 2\%$  by weight; laminates satisfied MIL-L-46197. Glass fabric was provided by Owens Corning in a 5 X 5 balanced construction with weight  $24 \text{ oz/yd}^2 \pm 3\%$  ( $814 \text{ g/m}^2 \pm 3\%$ ); resin coating of the fabric was performed by American Cyanamide using Cycom 4102 polyester resin. The final laminates were manufactured according to the processing schedule of MIL-L-46197.

This progress report summarizes work conducted by the ARL Materials Directorate in FY93. Enlargement and extension of the data base constructed in this work is planned for FY94. The ultimate aim of the effort is first to provide design guidelines for application of S-2 glass-reinforced plastic laminates in ground combat vehicle structures and second to define dynamic behavior and response of this material for general applications in armor technology.

## **2. BALLISTIC IMPACT DAMAGE EVALUATION**

Primary concerns for any armored structure must include the extent of damage and residual integrity of the structure following ballistic attack. Metal-based armored structures generally enjoy a large margin of structural over design. This follows from the structurally generous cross-section of metal required to defeat the ballistic design threat and the fact that ballistic failure modes for metals are localized. Consequently, residual integrity of metal-based armored structures is not a major issue. Glass-reinforced plastic laminates, on the other hand, demonstrate large ballistic damage zones so that extent of damage and residual strength of glass-reinforced plastic based structures must necessarily be a design concern.

### **a. Ballistic Impact Experiments**

The scope of this study was confined to characterization of ballistic impact damage in monolithic laminates of S-2 glass fabric-reinforced plastic produced by fragment-simulating projectiles. Ballistic damage resulting from impact by projectiles other than fragments and damage experienced by a GRP laminate that is the rear or backup component for applique armor are subjects for future work. However, a preliminary experiment was conducted to examine damage to a GRP laminate acting as backup component in an applique type design; specifically a fragment impact test was conducted on a two-component armor system consisting of a titanium alloy (MIL-A-46077) frontal plate backed by the GRP laminate.

Each of the GRP laminate targets tested was subjected to a single fragment impact. Test parameters for the monolithic laminate targets included fragment mass, strike velocity, and laminate thickness. Tests were conducted with fragment simulators of mass 207 grains (12.7 mm in caliber) and 830 grains (20 mm in caliber) at 0° oblique impact. Strike velocity was varied but, in all cases, kept below the limit velocity of the test laminate to produce only partial penetration of the target. Except in the case of the titanium-faced GRP laminate target and a monolithic GRP laminate of thickness 2.95", a minimum of two replicate tests were conducted for each strike velocity.

Fragments were launched using rifled barrels of 8' length with twist 1/15 for the 12.7 mm barrel and 1/24 for the 20 mm barrel. Fragment velocity and yaw measurements were made from orthogonal radiographs taken 44" from the target face. A drag correction was applied to the measured velocity to obtain the strike velocity. Projectile yaw did not exceed 1.5° for any test shot.

The GRP laminate targets were supported by a rigid, vertical steel frame with an 18"-diameter circular opening. The target was centered on the circular opening and held to the frame by clamps located at each of the four corners of the target. A .020"-thick 2024-T6 aluminum alloy sheet 18" X 18" in size was sandwiched between the rear face of the GRP laminate and the front face of the target holder to measure the maximum transient displacement of the laminate rear surface.



Table 2.1 summarizes the individual test shots conducted in this work. Since test laminates received but a single shot, test panels are identified by the shot identification or T number.

Table 2.1 Summary of Ballistic Tests

Panel No.	S-2 GRP Laminate Panel Size (in)	Ply Count	Fragment Mass (grains)	Strike Velocity (ft/sec)
T44-93-1	20x20x1.73	69	207	1912
T44-93-2	20x20x1.73	69	207	2025
T44-93-3	20x20x1.73	69	207	3022
T44-93-4	20x20x1.73	69	207	2946
T44-93-5	20x20x1.73	69	207	3938
T44-93-6	20x20x1.73	69	207	3958
T 7-93-1	20x20x1.64	63	830	1522
T 7-93-2	20x20x1.63	63	830	1581
T28-93-1	20x20x1.71	67	830	1256
T28-93-2	20x20x1.73	67	830	1180
T28-93-3	20x20x1.68	67	830	1257
T26-93-1	20x20x1.73	67	830	1729
T26-93-2	20x20x1.68	67	830	1865
T26-93-3	20x20x1.68	67	830	1753
T27-93-1	20x20x1.70	67	830	2459
T27-93-2	20x20x1.69	67	830	2559
T27-93-3	20x20x1.68	67	830	2450
T45-93-1*	20x20x1.72	69	830	4100
T45-93-2	23x23x2.95	118	830	4109

\*Frontal titanium plate 14" X 14" X .83" clamped to GRP laminate

Following ballistic test, the GRP laminates were shipped to Ogden Air Logistics Center at Hill AFB, Utah where computed tomography (CT) was conducted to measure internal delamination. Panels were then returned to Materials Directorate for measurement of compressive strength. These results are described in the following sections.

#### **b. Computed Tomography Analysis Of Delamination**

Computed tomography (CT) inspection was used to locate and quantify internal delamination resulting from ballistic impact for each GRP laminate identified in Table 2.1. Scans of the panel cross-sectional area normal to the thickness axis were taken at planes along the thickness direction. Scans were taken with a 2.0 mm slice thickness uniformly spaced 2.0 mm along the entire panel thickness; a total of nineteen or twenty scans was used for each panel. Since the CT image obtained for each scan is a representation of x-ray attenuation in the slice plane and, in this case, since the attenuation is due almost entirely to density, the CT image is a density map of the slice plane. The area in the CT image identified as low density is attributed here to delamination in the slice plane. Delaminated area displayed symmetry about the impact point and, to a first approximation, can be considered as circular. Percent delamination for each slice was obtained by simply dividing the delaminated area identified in the slice plane by the panel area. Details of CT inspection including system and scan parameters and imagery analysis is contained in Appendix A.

Results of the CT inspection for each GRP laminate are contained in Figures 2.1 through 2.19. Percent delamination for each 2.0 mm slice is shown as a function of slice location from the impact face; slice location is taken to be at the midplane of the 2.0 mm slice. The extent of delamination in slices along the thickness direction for each GRP laminate penetrated by a fragment simulator displays the same general pattern, namely a fall to a minimum value followed by a rise to a maximum value at the rear face of the laminate. For the titanium-faced target, extent of delamination of the GRP laminate rises almost monotonically from a minimum value at the front face of the GRP laminate to a maximum value at its rear face. Delamination profiles through the thickness direction show good reproducibility for replicate experiments. In instances wherein the fragment simulator was imbedded in the GRP laminate, the scan or slice containing the front face of the projectile is identified in Figures 2.1 through 2.19.

Table 2.2 tabulates depth of fragment penetration, percent delamination averaged over all slices, and delaminated volume for each GRP laminate; these results are taken from Figures 2.1 through 2.19. Delaminated volume is simply the product of panel total volume and average fraction delamination. Depth of penetration was obtained using the expression  $dop (mm) = (1/2)(t-2n) + 2m + 1$  where  $t$  is the panel thickness in mm,  $n$  is the total number of slices taken on the panel (19 or 20), and  $m$  is the slice number, counting from the impact face, that contains the tip of the fragment. Delaminated volume for all test panels except T45-93-1 is shown in Figure 2.20 as a function of fragment mass and strike velocity. Clearly, each graph of Figure 2.20 applies only up to the limit velocity of the GRP laminate. Fragment depth of penetration in GRP laminate is plotted versus strike velocity for the 207 grain and 830 grain fragments in Figure 2.21.

Figure 2.1 - Delamination Profile of Test Panel T44-93-1

Slice	% Delam
1	4.60%
2	2.53%
3	1.83%
4	1.01%
5	0.85%
6	0.97%
7	1.54%
8	1.68%
9	1.93%
10	2.27%
11	2.69%
12	3.08%
13	3.29%
14	3.43%
15	3.96%
16	5.37%
17	6.34%
18	8.02%
19	9.11%
20	10.71%

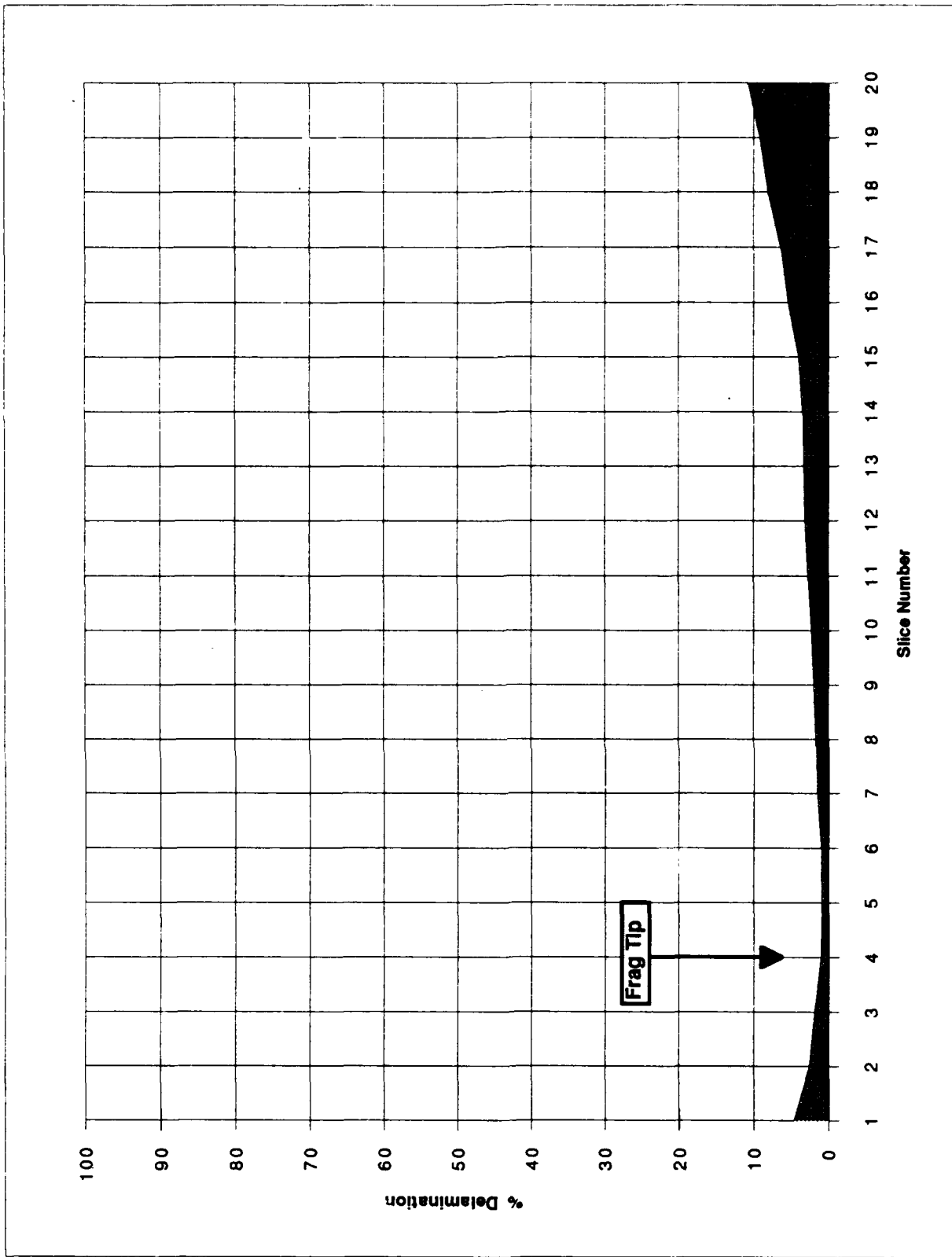


Figure 2.2 - Delamination Profile of Test Panel T44-93-2

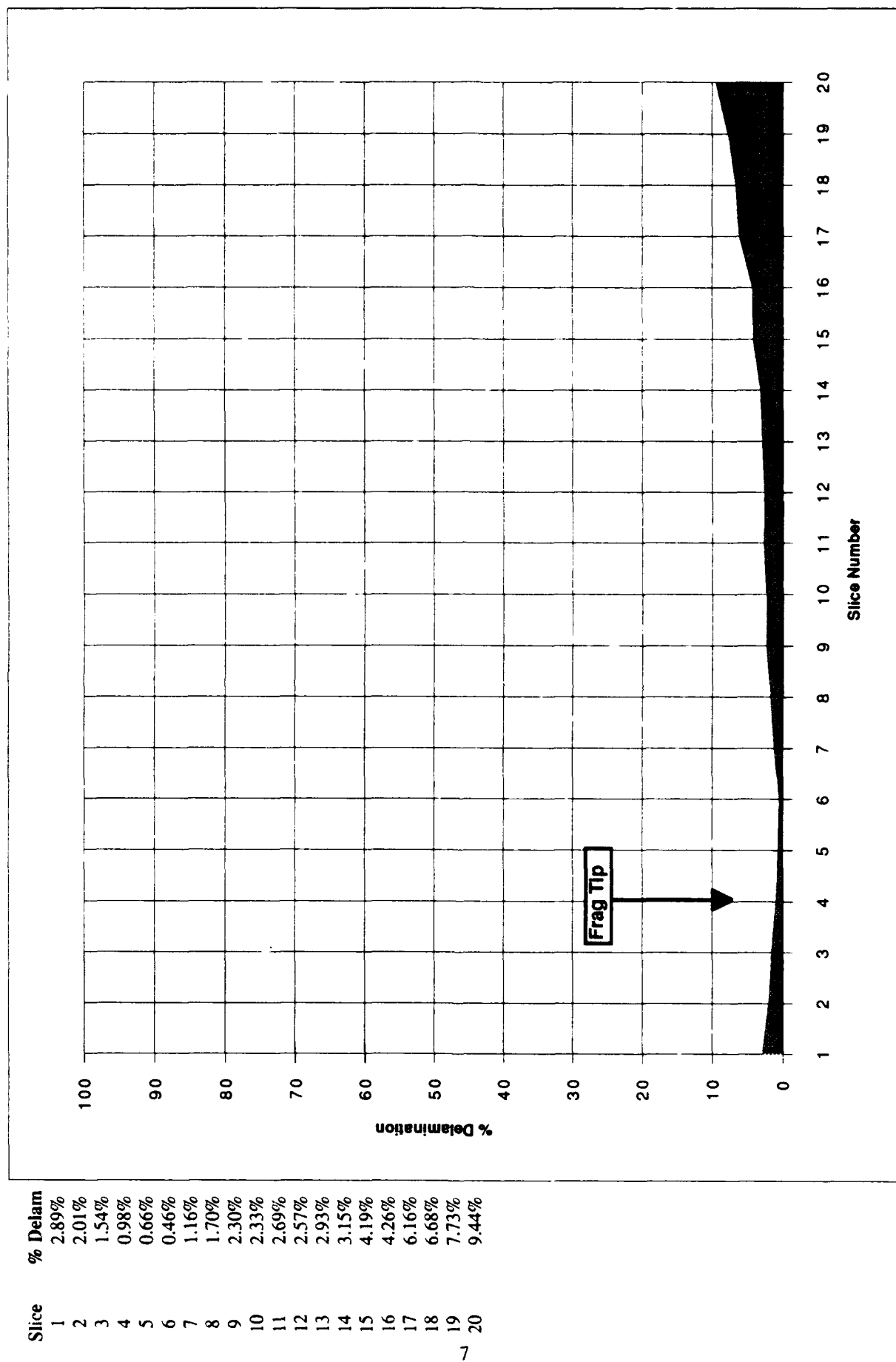


Figure 2.3 - Delamination Profile of Test Panel T44-93-3

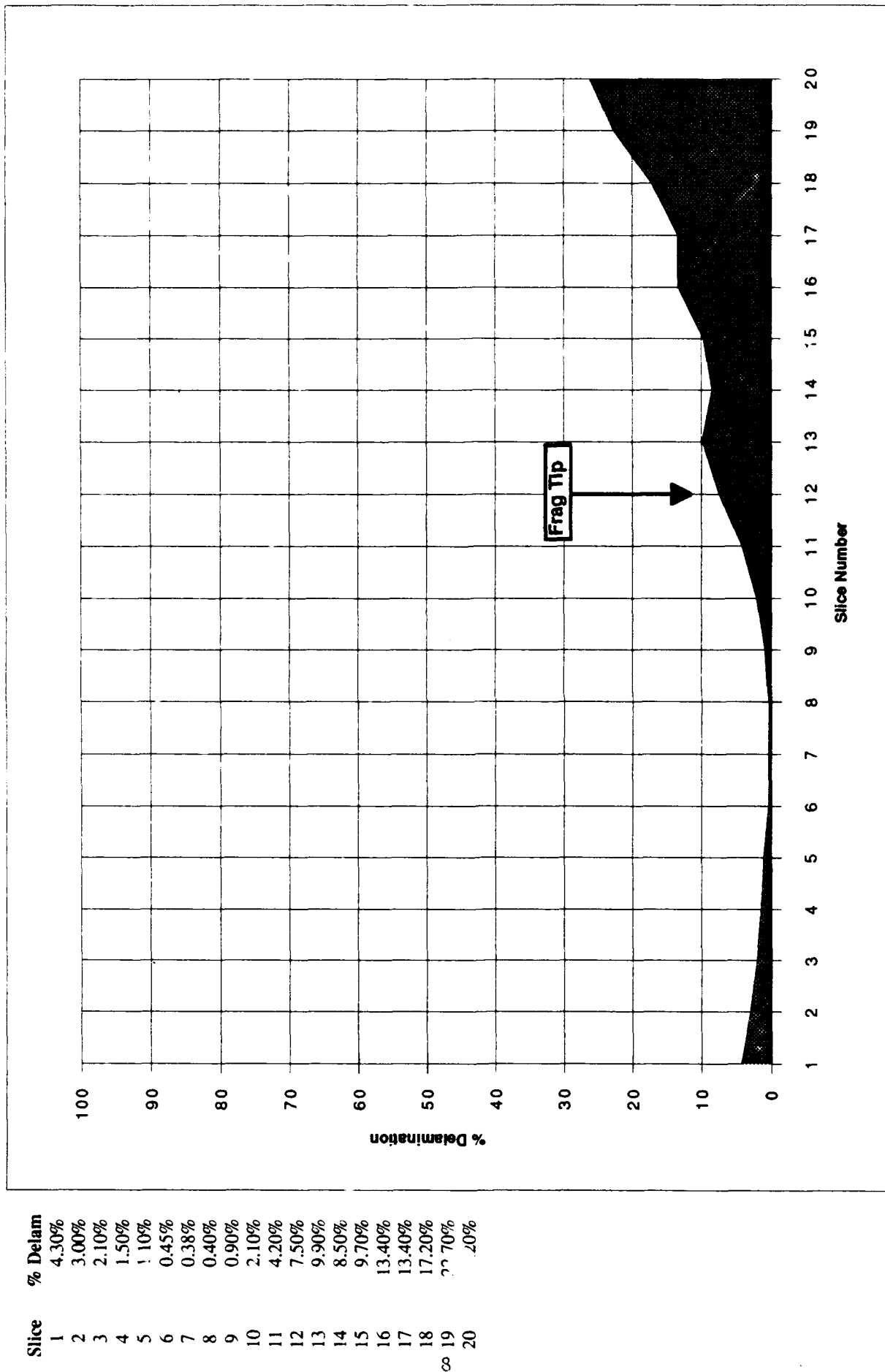


Figure 2.4 - Delamination Profile of Test Panel T44-93-4

Slice	% Delam
1	5.73%
2	3.16%
3	2.16%
4	1.64%
5	1.31%
6	0.65%
7	0.36%
8	0.36%
9	0.76%
10	1.55%
11	4.81%
12	6.83%
13	8.05%
14	9.71%
15	11.02%
16	11.20%
17	12.10%
18	15.06%
19	17.14%
20	22.68%

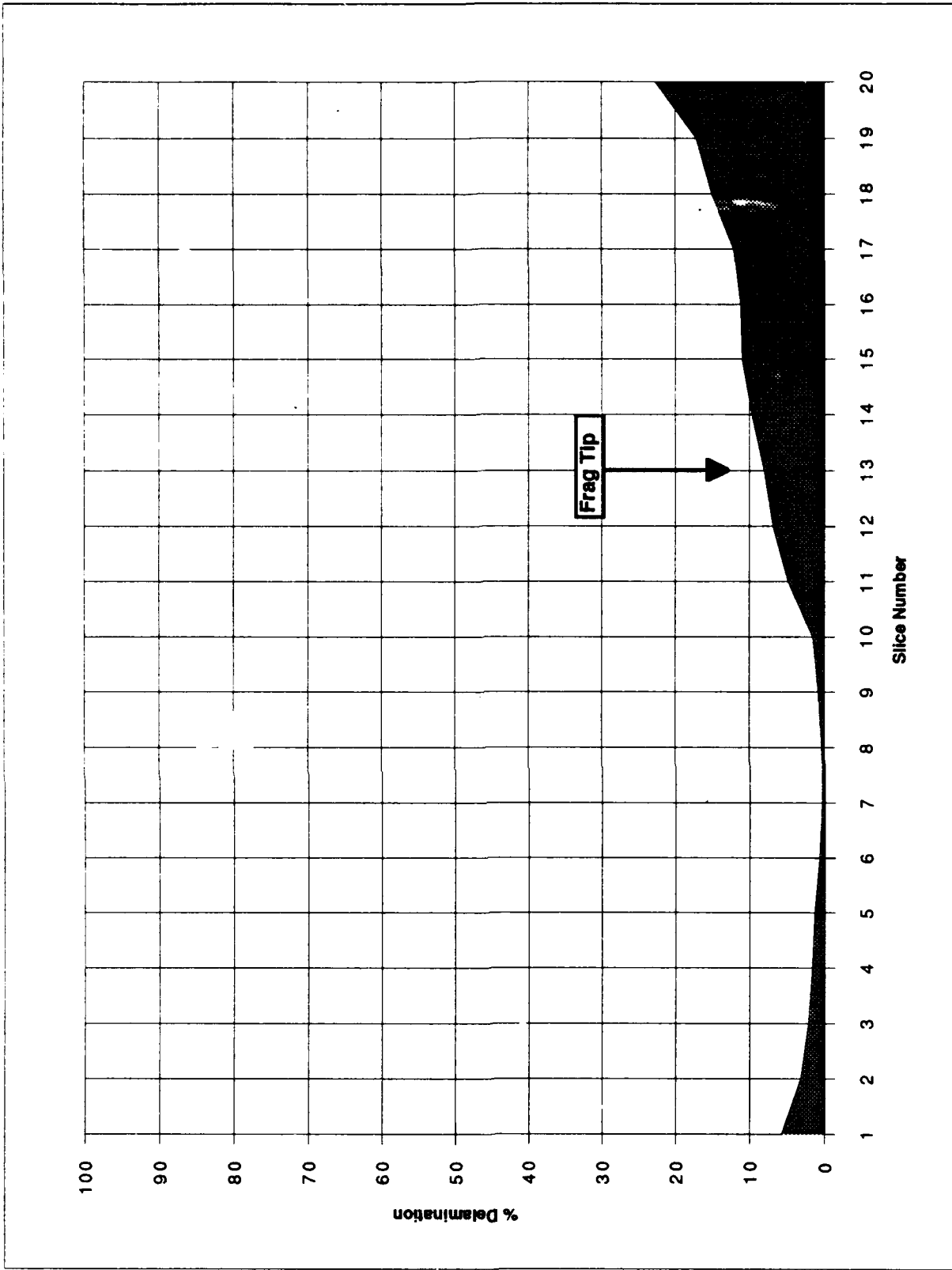


Figure 2.5 - Delamination Profile of Test Panel T44-93-5

Slice	% Delam
1	7.82%
2	5.69%
3	3.70%
4	2.71%
5	2.31%
6	1.56%
7	1.14%
8	0.76%
9	0.79%
10	1.42%
11	2.10%
12	3.56%
13	7.15%
14	13.50%
15	16.45%
16	28.78%
17	34.73%
18	37.07%
19	45.42%
20	55.84%

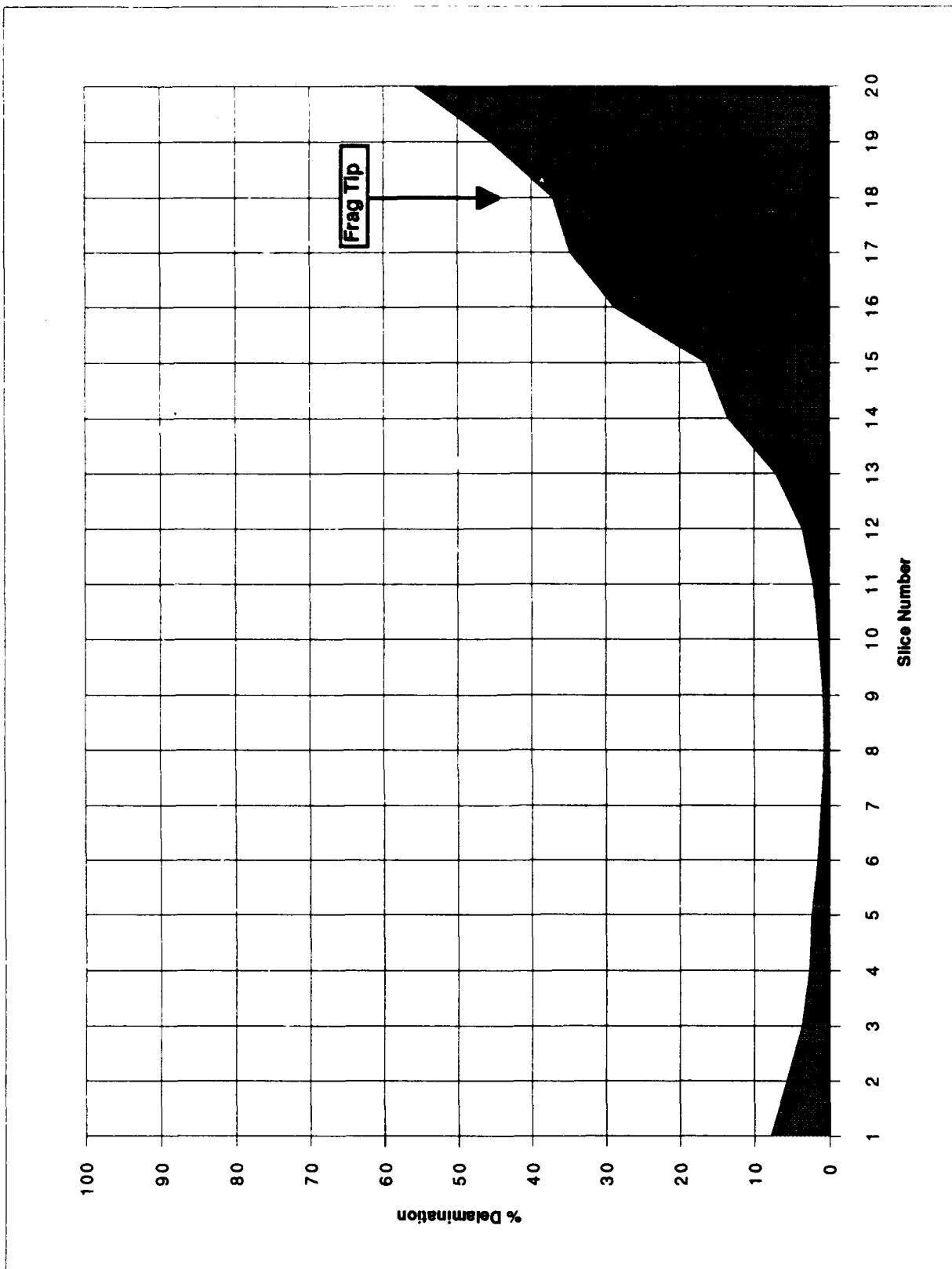


Figure 2.6 - Delamination Profile of Test Panel T44-93-6

Slice	% Delam
1	8.00%
2	5.59%
3	3.65%
4	2.56%
5	2.13%
6	1.54%
7	1.13%
8	0.74%
9	0.68%
10	1.07%
11	1.84%
12	3.61%
13	5.59%
14	10.64%
15	14.61%
16	22.33%
17	36.85%
18	40.57%
19	45.66%
20	57.07%

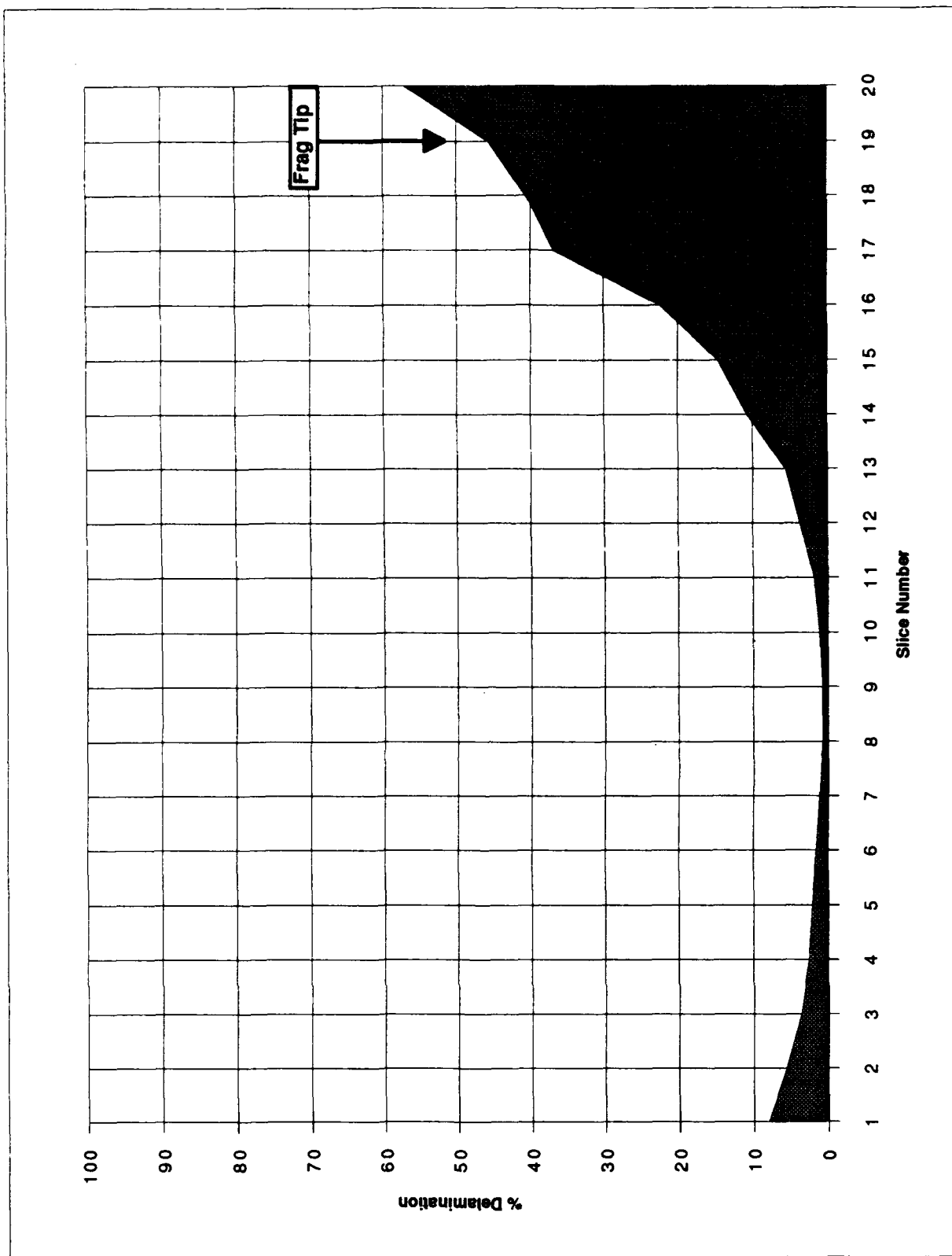




Figure 2.7 - Delamination Profile of Test Panel T7-93-1

Slice	%Delam
1	5.36%
2	3.77%
3	2.18%
4	1.11%
5	1.96%
6	3.75%
7	5.76%
8	8.82%
9	9.78%
10	9.81%
11	10.22%
12	10.40%
13	12.22%
14	13.13%
15	13.81%
16	17.16%
17	19.03%
18	21.82%
19	25.74%

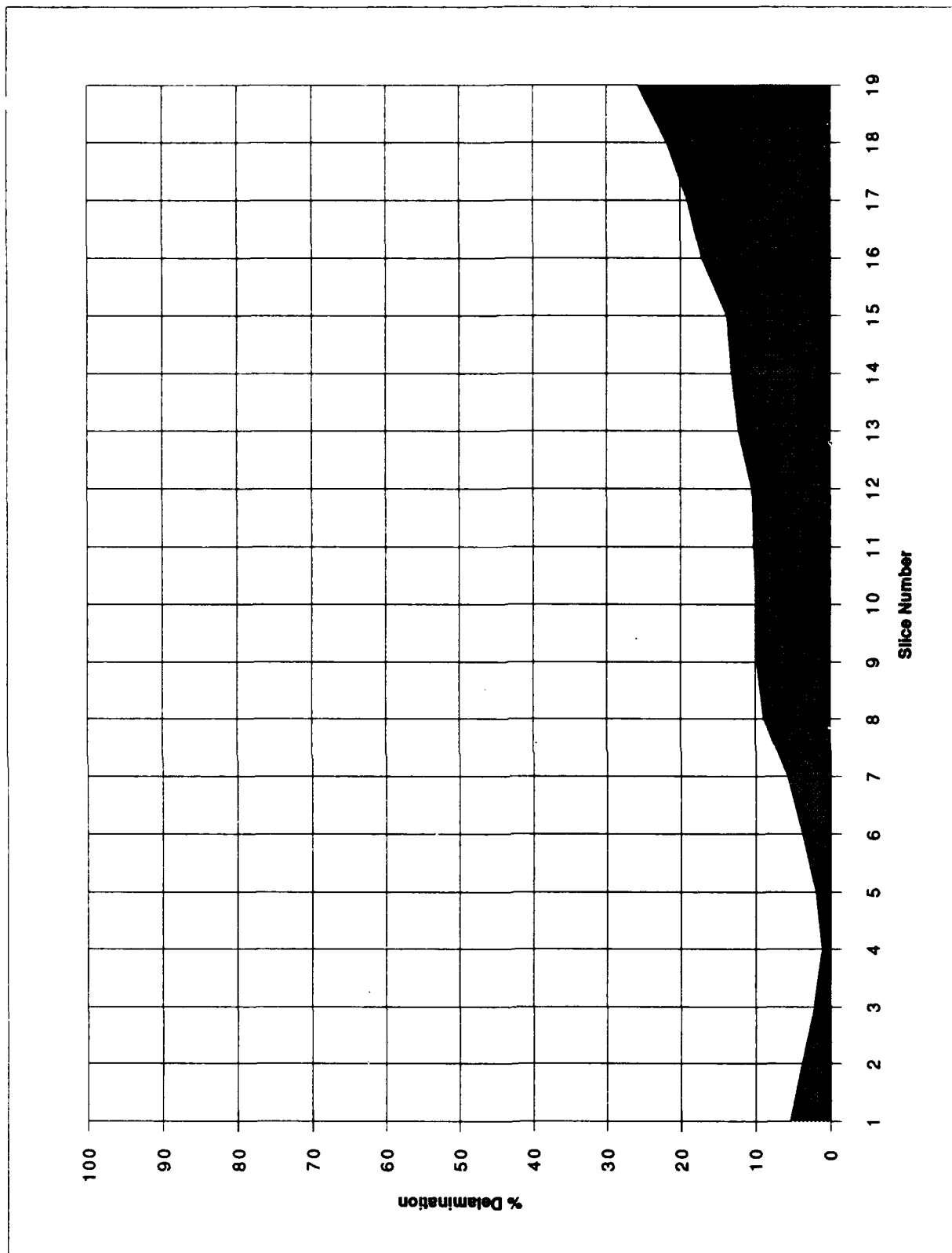


Figure 2.8 - Delamination Profile of Test Panel T7-93-2

Slice	% Delam
1	6.29%
2	4.38%
3	2.84%
4	1.08%
5	0.96%
6	1.99%
7	3.44%
8	6.26%
9	9.48%
10	9.13%
11	11.05%
12	11.89%
13	12.87%
14	15.36%
15	17.45%
16	19.38%
17	20.01%
18	23.42%
19	28.91%

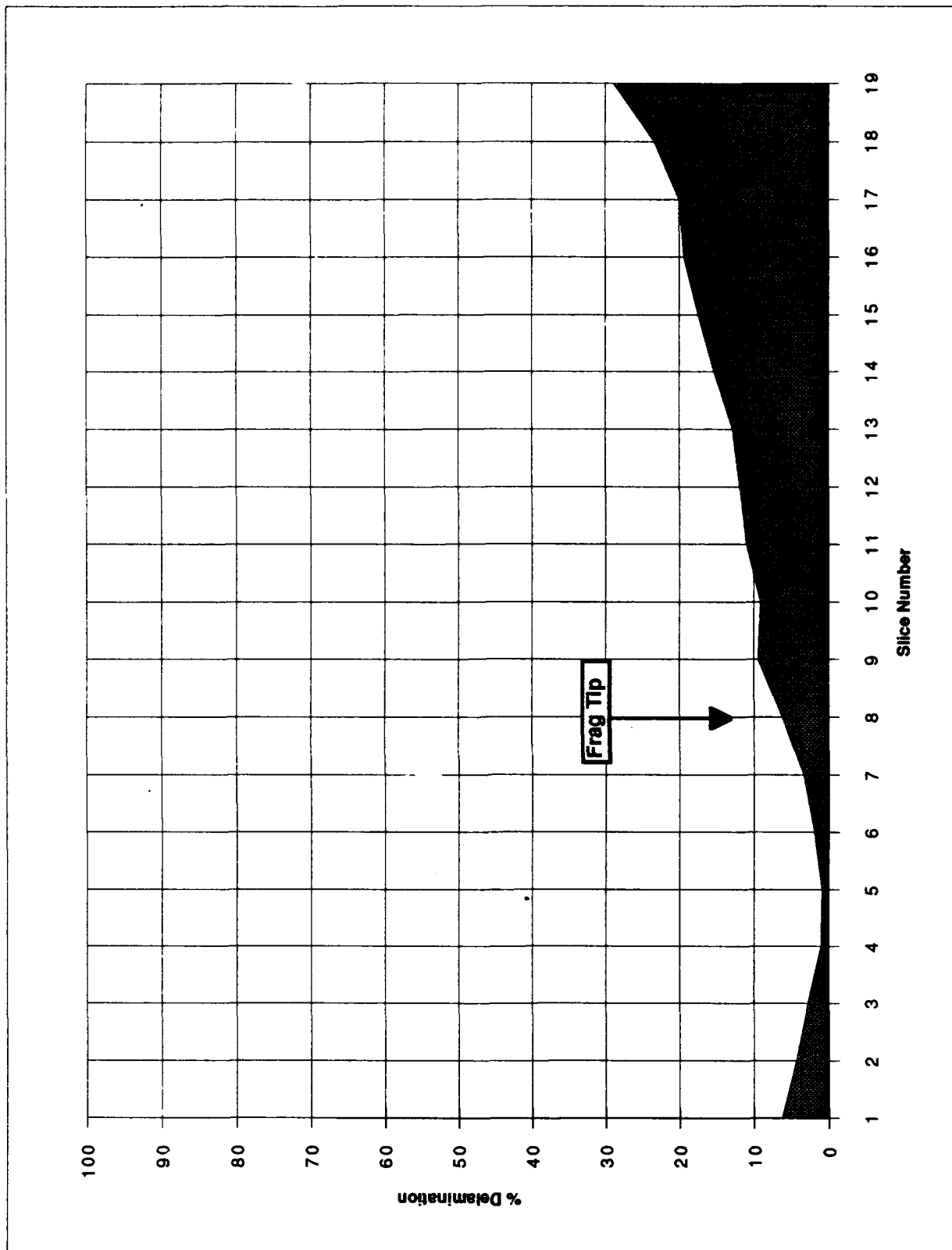


Figure 2.9 - Delamination Profile of Test Panel T28-93-I

Slice	% Delam
1	4.42%
2	2.60%
3	1.42%
4	0.89%
5	2.48%
6	4.00%
7	3.90%
8	4.87%
9	4.83%
10	7.50%
11	6.48%
12	8.36%
13	9.68%
14	9.60%
15	9.65%
16	12.60%
17	8.09%
18	15.54%
19	20.54%
20	18.43%

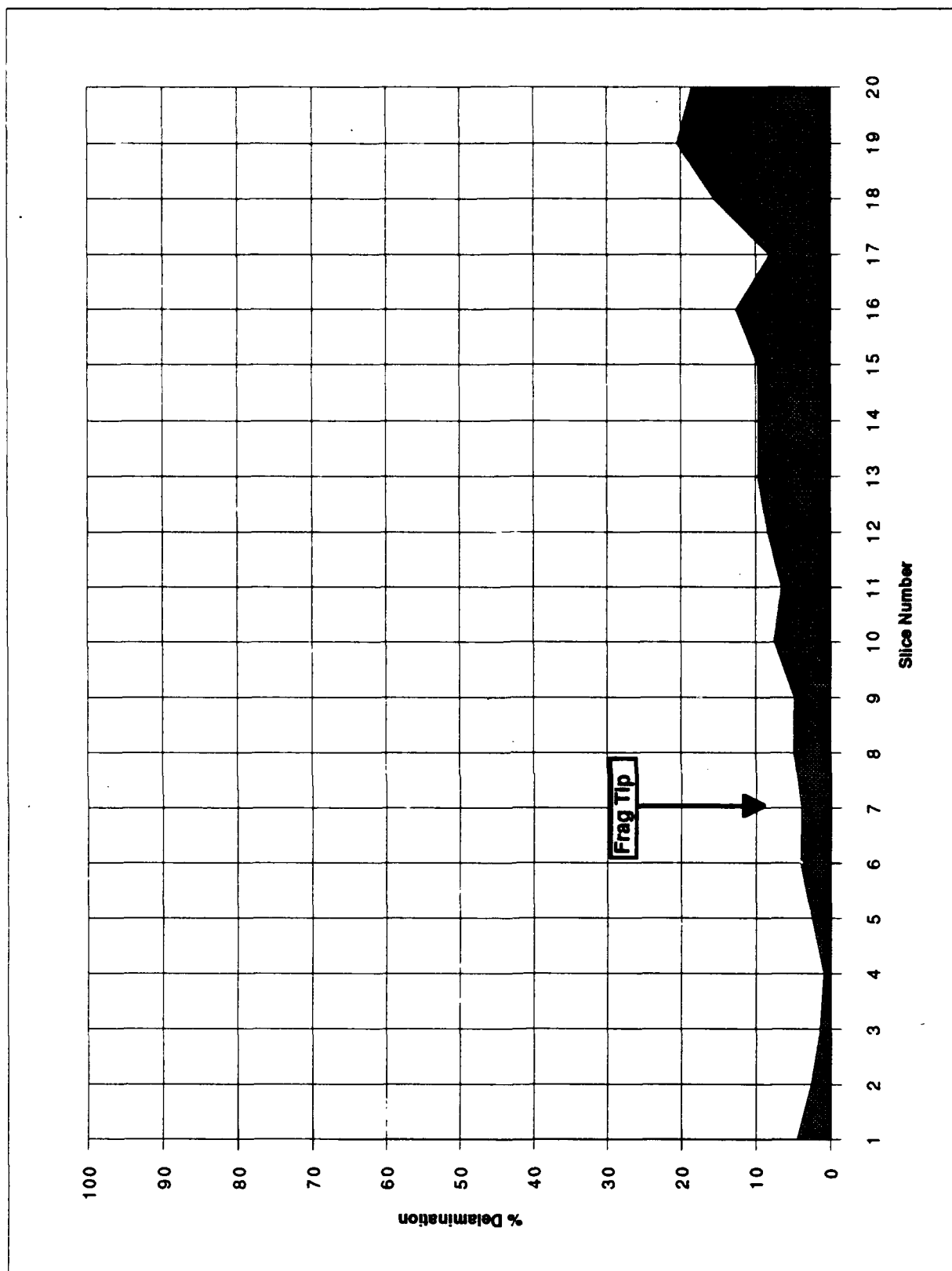


Figure 2.10 - Delamination Profile of Test Panel T28-93-2

Slice	% Delam
1	2.95%
2	2.27%
3	1.56%
4	1.55%
5	3.34%
6	4.61%
7	4.13%
8	4.56%
9	4.90%
10	5.97%
11	7.47%
12	7.70%
13	8.22%
14	9.68%
15	8.99%
16	12.41%
17	10.60%
18	14.87%
19	20.68%
20	22.40%

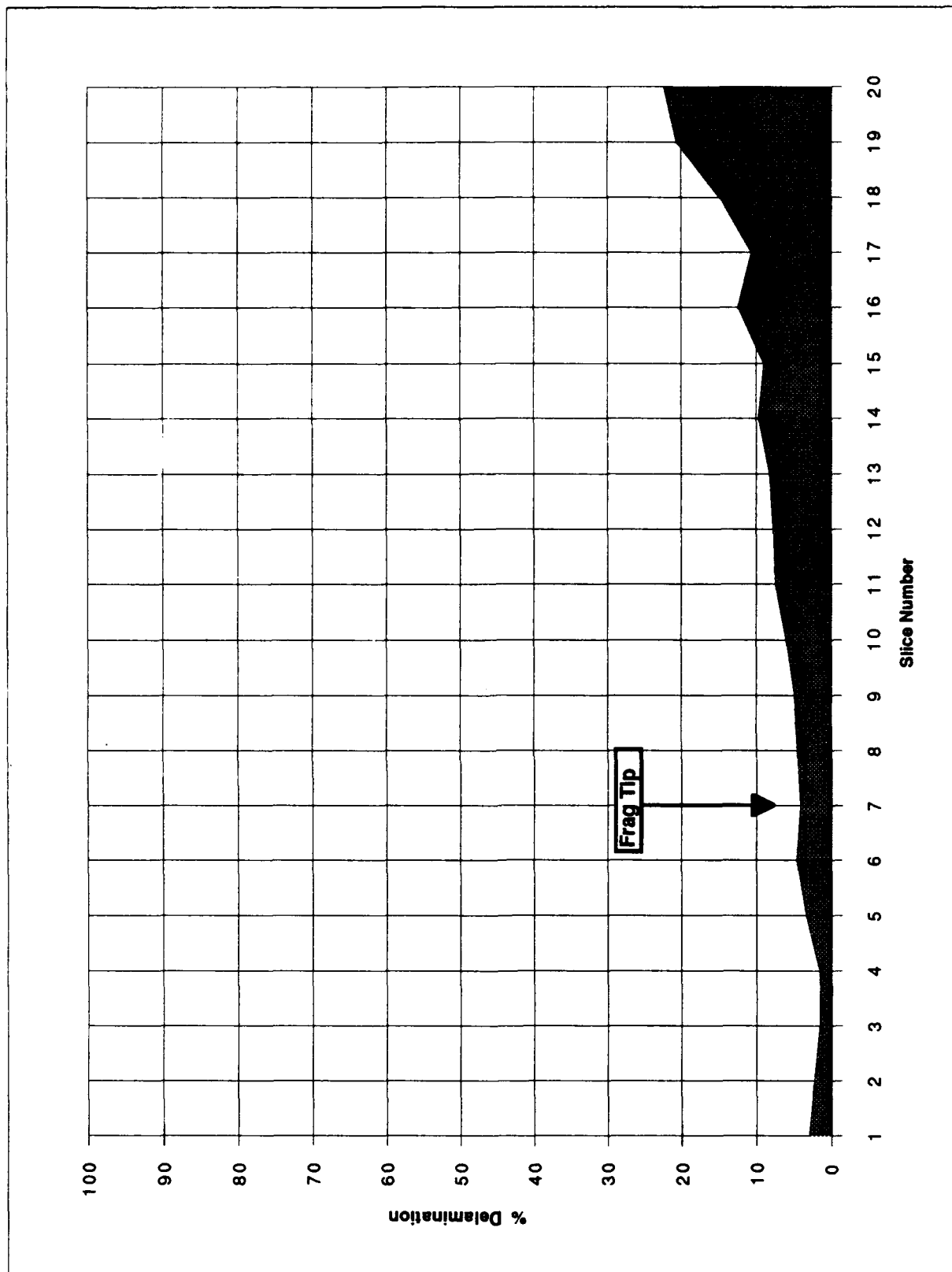


Figure 2.11 - Delamination Profile of Test Panel T28-93-3

Slice	% Delam
1	2.84%
2	2.13%
3	1.50%
4	1.30%
5	3.15%
6	4.71%
7	4.20%
8	5.87%
9	6.91%
10	7.75%
11	7.01%
12	6.79%
13	7.71%
14	8.52%
15	9.56%
16	8.99%
17	11.66%
18	17.91%
19	26.07%

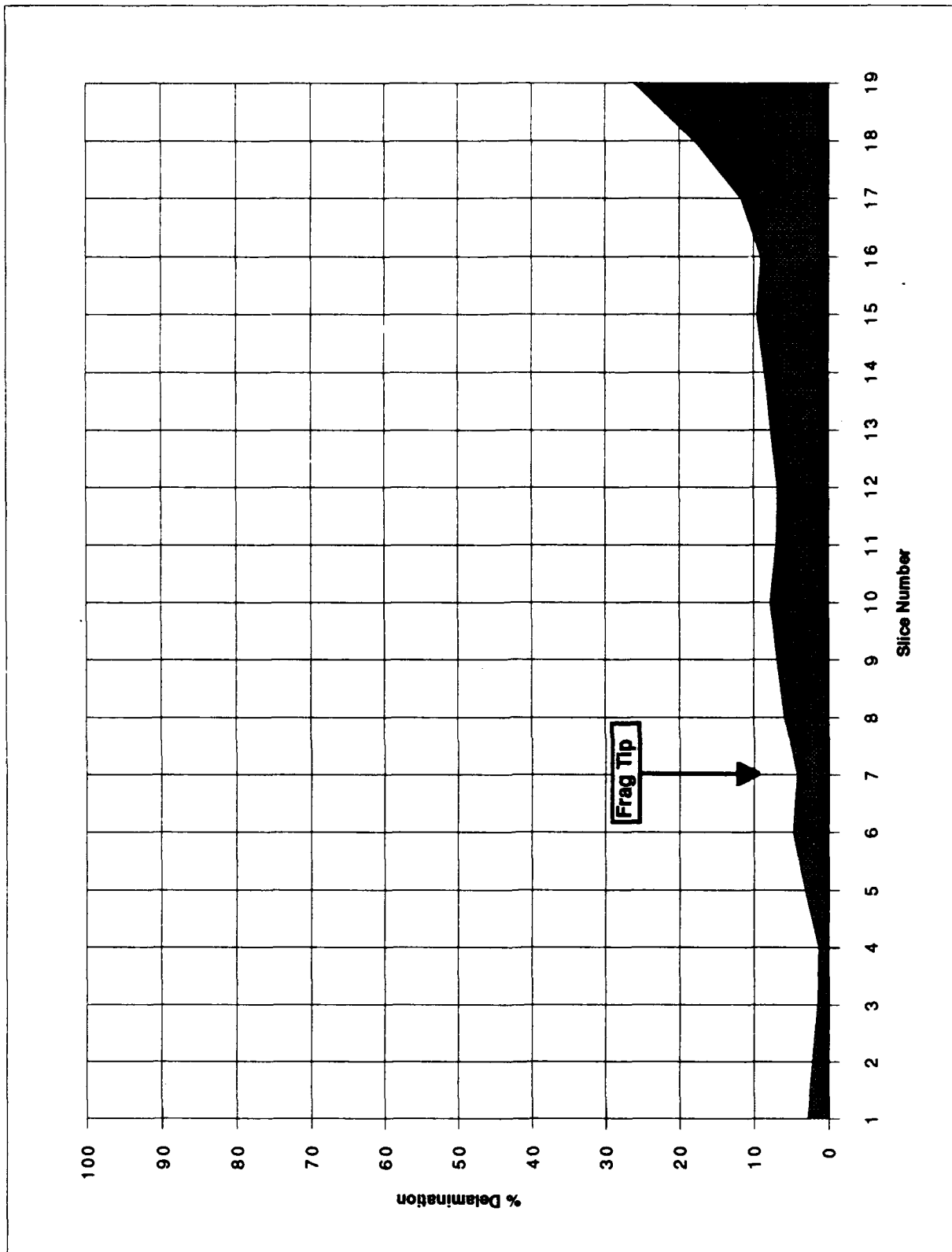


Figure 2.12 - Delamination Profile of Test Panel T26-93-1

Slice	% Delam
1	5.51%
2	3.54%
3	2.56%
4	1.83%
5	1.25%
6	1.32%
7	2.57%
8	5.12%
9	9.62%
10	12.43%
11	12.94%
12	12.78%
13	15.05%
14	16.78%
15	16.45%
16	22.94%
17	19.41%
18	32.96%
19	26.09%
20	36.68%

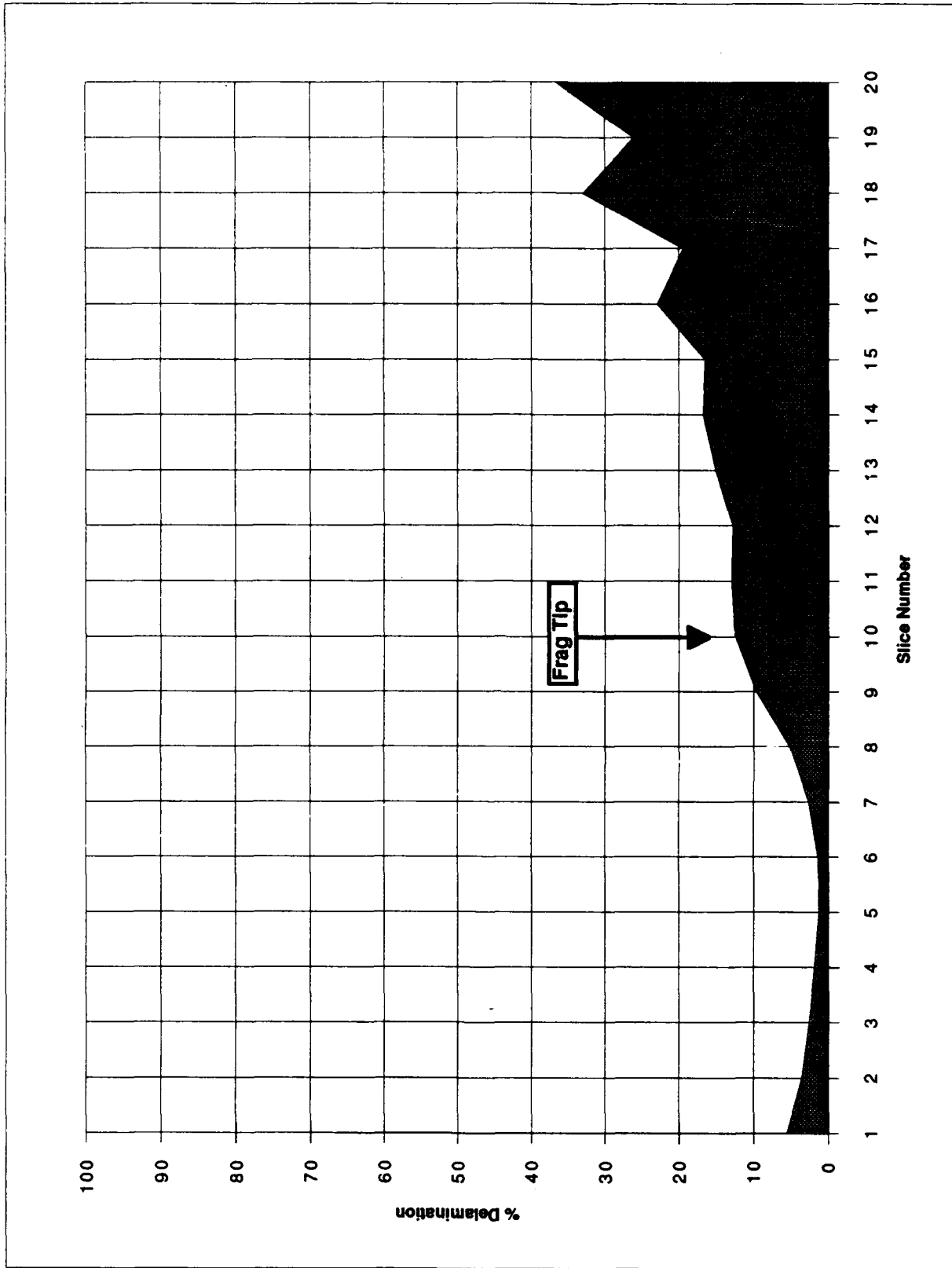


Figure 2.13 - Delamination Profile of Test Panel T26-93-2

Slice	% Delam
1	3.94%
2	2.79%
3	2.11%
4	1.00%
5	1.02%
6	2.07%
7	3.08%
8	7.04%
9	15.61%
10	20.74%
11	19.33%
12	22.04%
13	21.07%
14	22.56%
15	31.47%
16	38.38%
17	39.87%
18	48.29%
19	43.16%

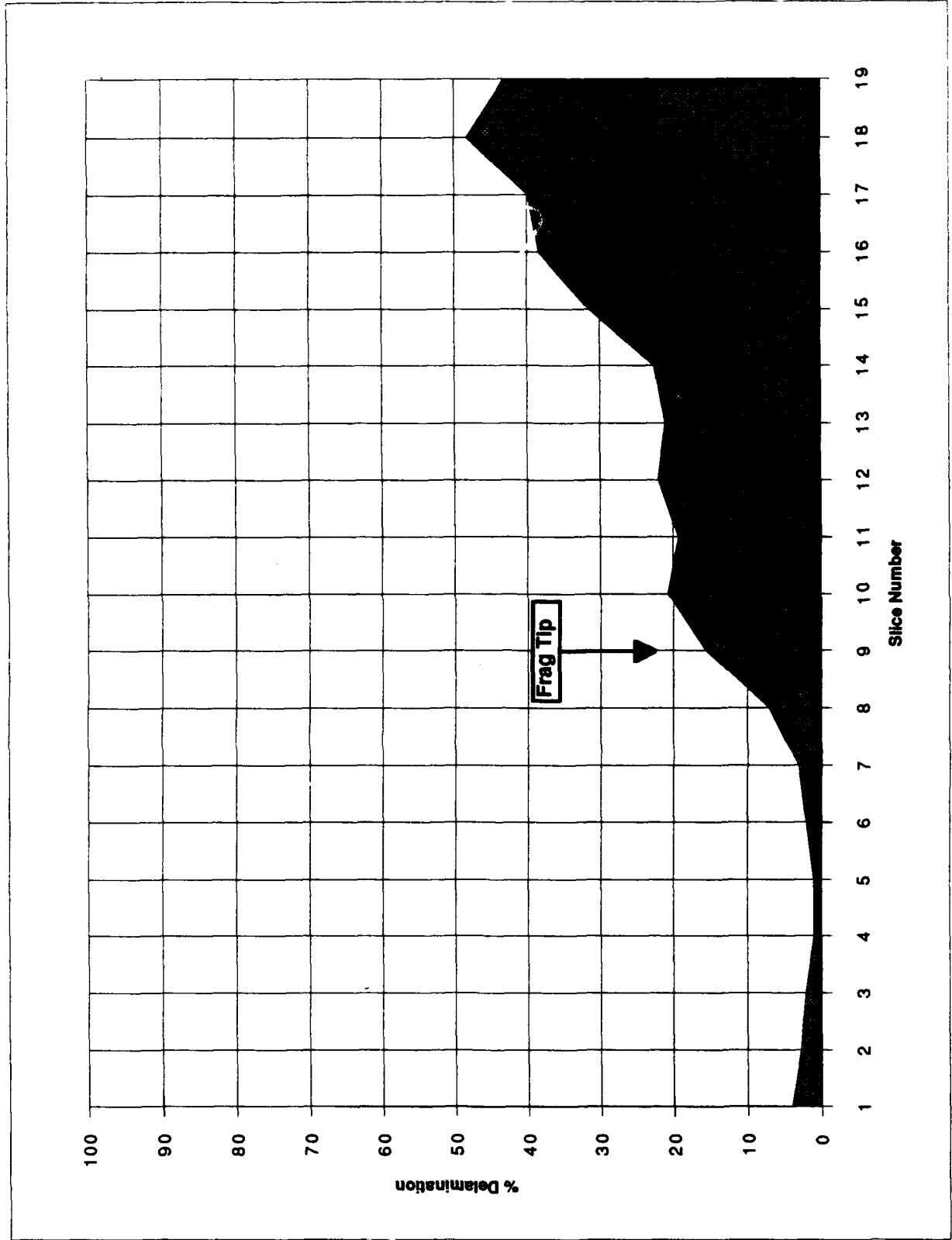


Figure 2.14 - Delamination Profile of Test Panel T26-93-3

Slice	% Delam
1	7.49%
2	4.69%
3	3.01%
4	1.84%
5	1.01%
6	1.76%
7	3.57%
8	7.21%
9	15.09%
10	17.21%
11	18.04%
12	17.71%
13	21.76%
14	24.06%
15	27.50%
16	28.21%
17	31.96%
18	36.27%
19	35.89%

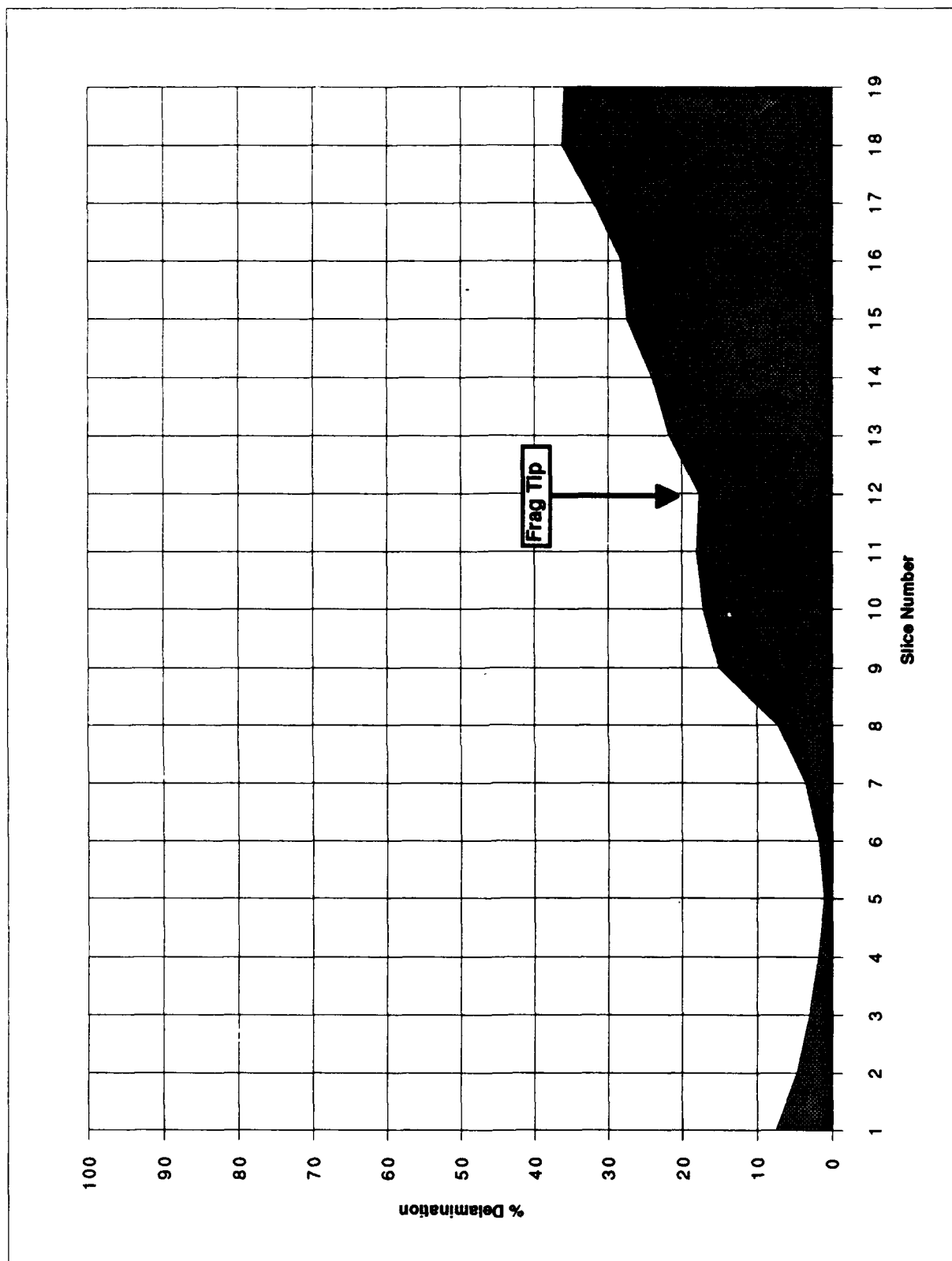




Figure 2.15 - Delamination Profile of Test Panel T27-93-1

Slice	% Delam
1	9.84%
2	5.12%
3	4.17%
4	3.26%
5	2.34%
6	1.37%
7	0.85%
8	1.09%
9	2.29%
10	9.37%
11	13.32%
12	17.70%
13	30.73%
14	45.91%
15	63.77%
16	76.02%
17	62.65%
18	68.59%
19	72.48%
20	71.18%

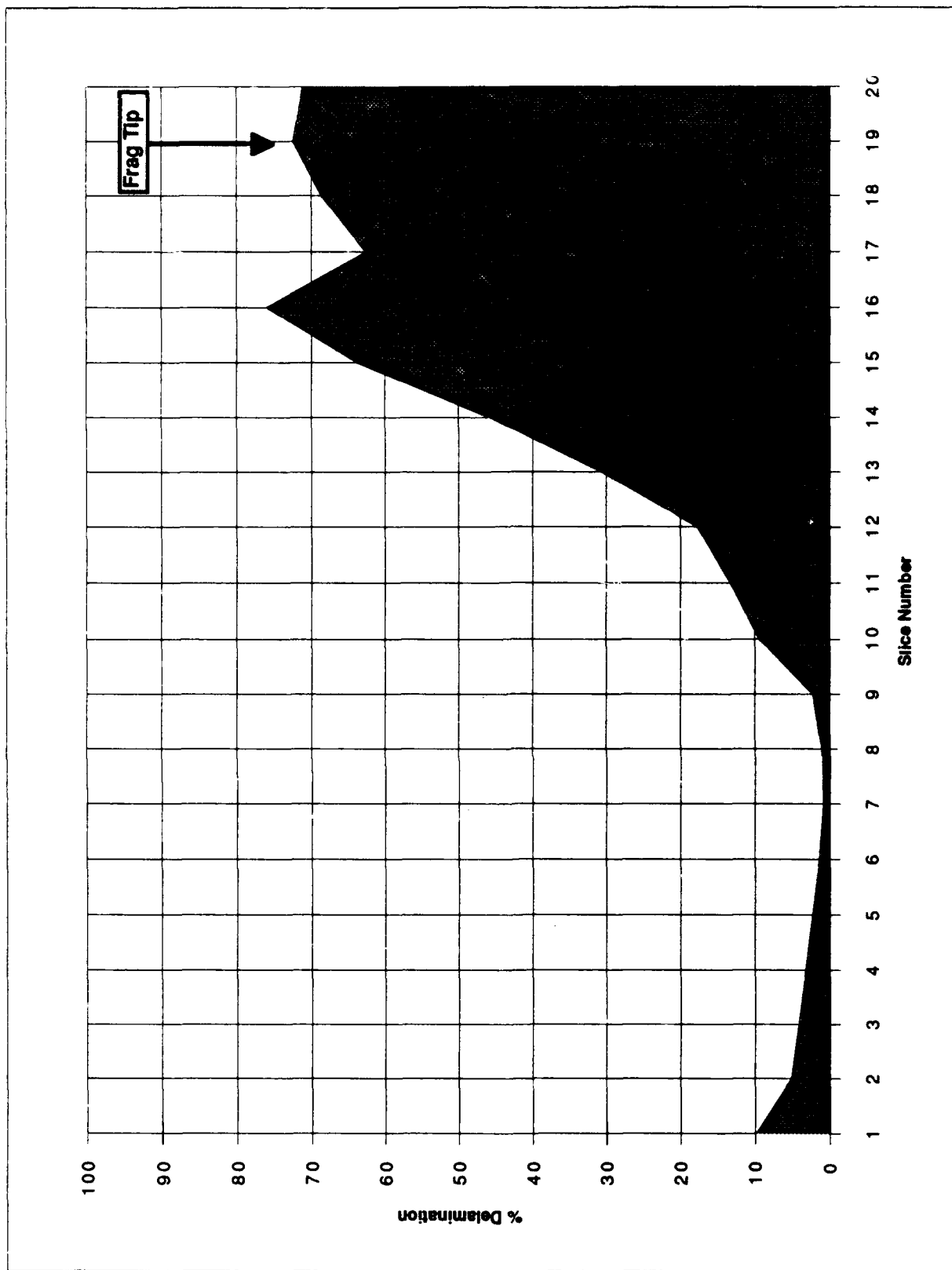


Figure 2.16 - Delamination Profile of Test Panel T27-93-2

Slice	% Delam
1	9.12%
2	6.19%
3	4.60%
4	3.36%
5	2.33%
6	1.76%
7	1.39%
8	1.72%
9	2.65%
10	5.68%
11	7.91%
12	12.84%
13	24.91%
14	30.48%
15	41.69%
16	73.67%
17	77.40%
18	81.55%
19	72.87%
20	74.46%

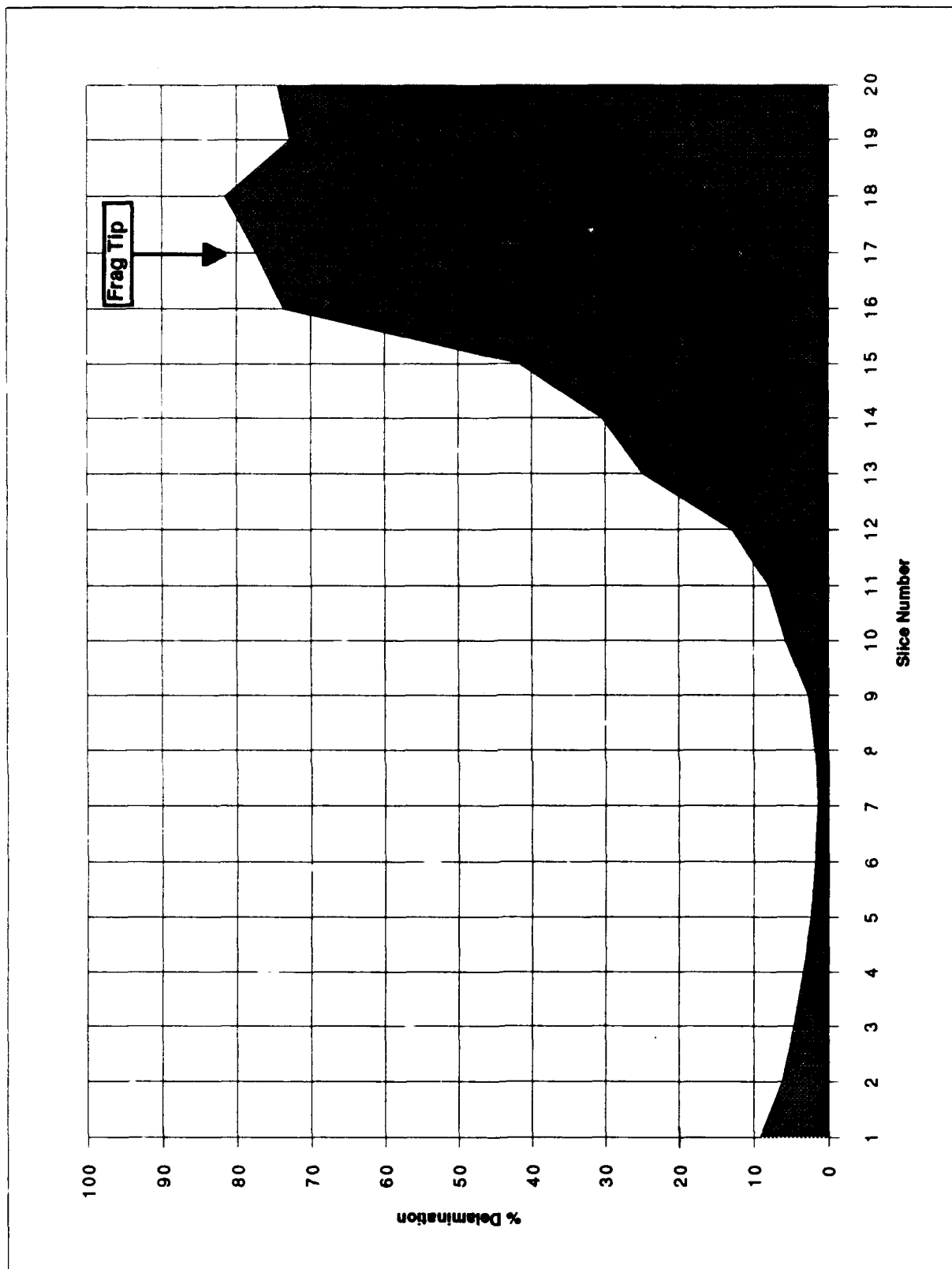
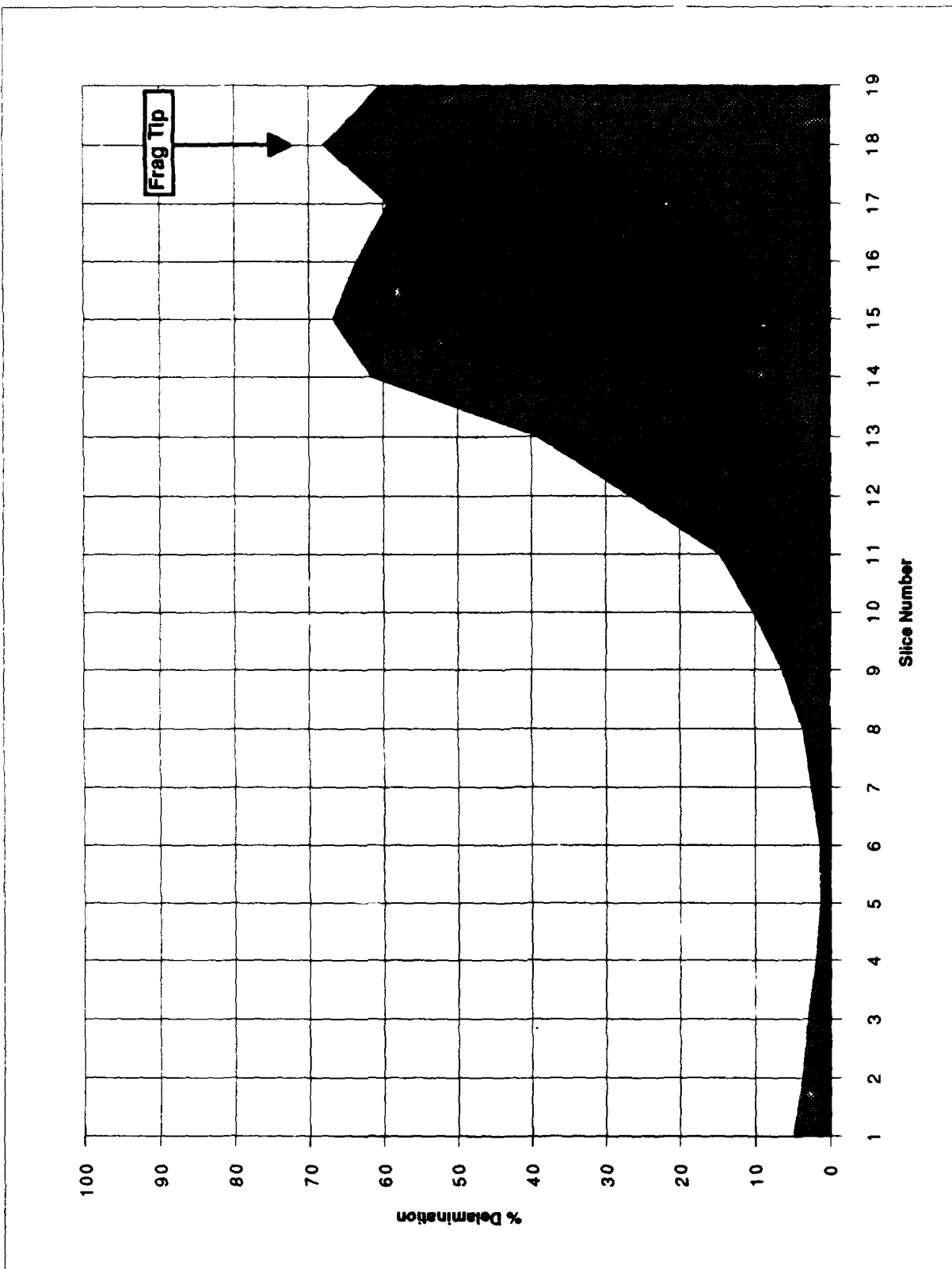
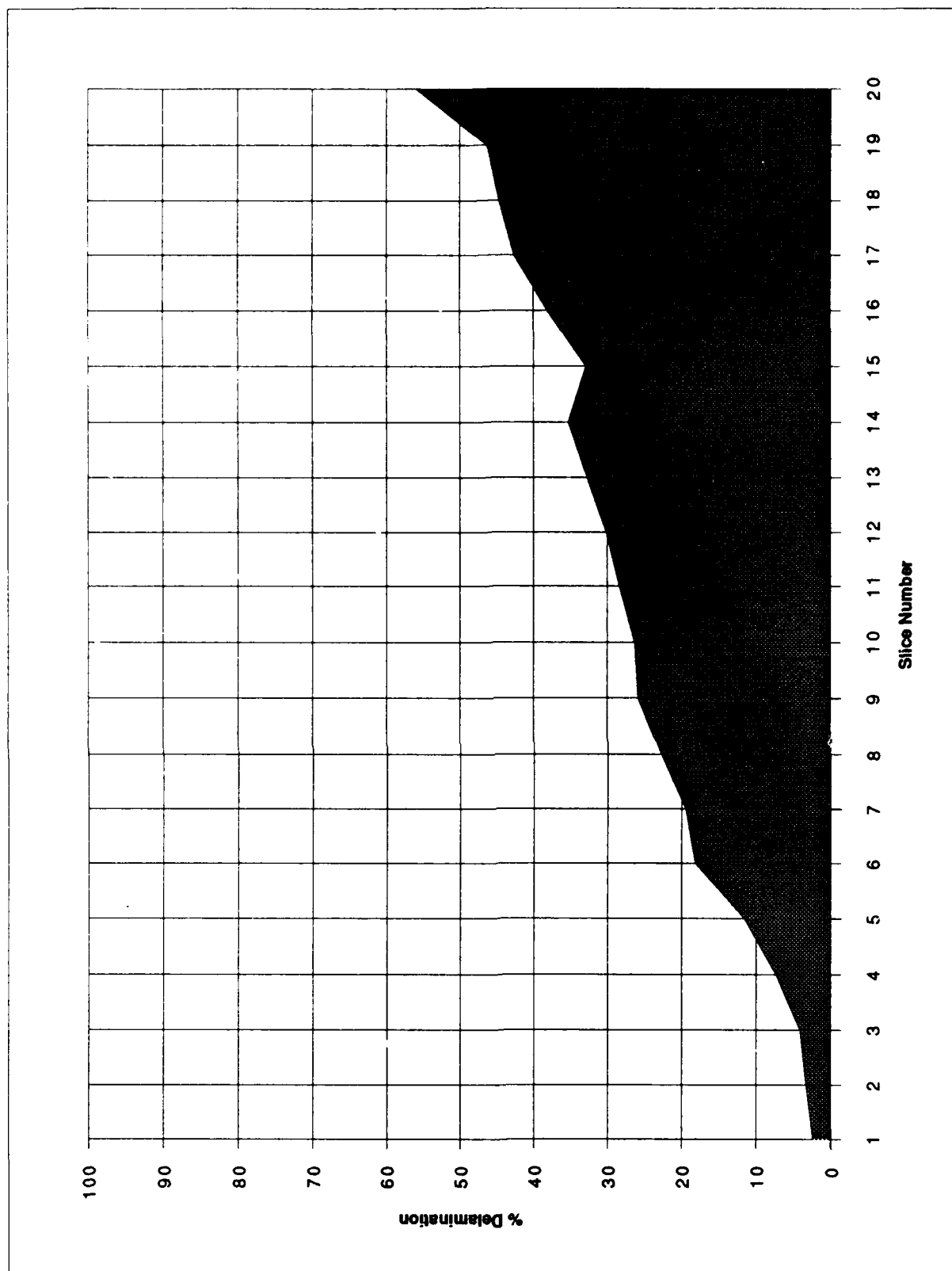


Figure 2.17 - Delamination Profile of Test Panel T27-93-3



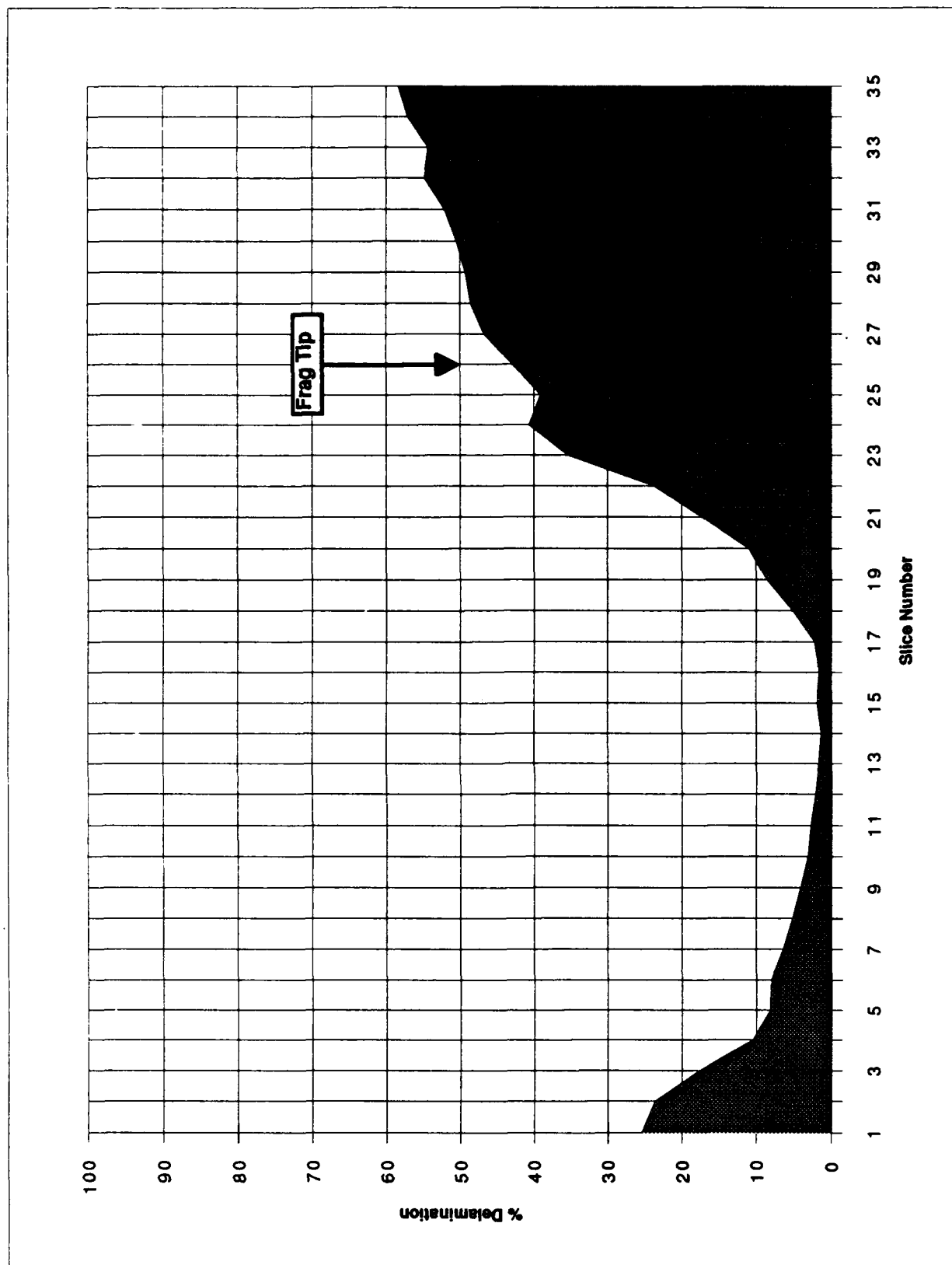
Slice	% Delam
1	4.97%
2	3.74%
3	2.98%
4	1.96%
5	1.32%
6	1.40%
7	2.62%
8	3.72%
9	6.36%
10	10.24%
11	14.67%
12	26.67%
13	39.23%
14	61.63%
15	66.91%
16	63.65%
17	59.36%
18	68.04%
19	60.45%

Figure 2.18 - Delamination Profile of Test Panel T45-93-1



Slice	% Delam
1	2.39%
2	3.34%
3	4.16%
4	7.33%
5	11.54%
6	18.16%
7	19.47%
8	22.77%
9	25.85%
10	26.30%
11	28.38%
12	30.16%
13	32.75%
14	35.29%
15	32.94%
16	38.15%
17	42.65%
18	44.75%
19	46.36%
20	55.96%

Figure 2.19 - Delamination Profile of Test Panel T45-93-2



Slice	%Delam
1	25.43%
2	23.63%
3	17.63%
4	10.48%
5	8.19%
6	8.03%
7	6.43%
8	5.19%
9	4.13%
10	3.13%
11	2.76%
12	2.17%
13	1.75%
14	1.43%
15	1.93%
16	1.64%
17	2.24%
18	5.14%
19	8.60%
20	11.01%
21	17.21%
22	23.76%
23	35.35%
24	40.64%
25	39.07%
26	42.83%
27	46.69%
28	48.57%
29	49.23%
30	50.49%
31	52.08%
32	54.82%
33	54.31%
34	57.07%
35	58.40%

Table 2.2 Damage Data For GRP Laminates

Panel No.	Panel <sup>1</sup> Thickness (in)	Fragment Mass (grains)	Strike Velocity (ft/sec)	Depth of Penetration (mm)	Average Delamination (%)	Delaminated Volume (in <sup>3</sup> )
T44-93-1	1.73	207	1912	8.6	3.76	26.02
T44-93-2	1.73	207	2025	8.6	3.29	22.77
T44-93-3	1.73	207	3022	24.6	7.45	51.55
T44-93-4	1.73	207	2946	26.6	6.81	47.13
T44-93-5	1.73	207	3938	36.6	13.63	94.32
T44-93-6	1.73	207	3958	38.6	13.29	91.97
T 7-93-1	1.64	830	1522	N/A	10.31	67.63
T 7-93-2	1.63	830	1581	16.3	10.85	70.74
T28-93-1	1.71	830	1256	14.6	7.79	53.28
T28-93-2	1.73	830	1180	14.6	7.94	54.94
T28-93-3	1.68	830	1257	15.6	7.61	51.14
T26-93-1	1.73	830	1729	20.6	12.89	89.20
T26-93-2	1.68	830	1865	19.6	18.19	122.24
T26-93-3	1.68	830	1753	25.6	16.01	107.59
T27-93-1	1.70	830	2459	38.6	28.10	191.08
T27-93-2	1.69	830	2559	34.6	26.83	181.37
T27-93-3	1.68	830	2450	37.6	26.31	176.80
T45-93-1 <sup>2</sup>	1.72	830	4100	N/A	26.44	181.91
T45-93-2	2.95	830	4109	53.5	23.47	366.26

1. All panels measure 20" X 20" in size except for T45-93-2 which measures 23" X 23".

2. Frontal titanium plate 14" X 14" X .83" clamped to GRP laminate.

—  $y = -46.869 + 0.034547x$   $R = 0.98195$

- - -  $y = -58.95 + 0.091386x$   $R = 0.98637$

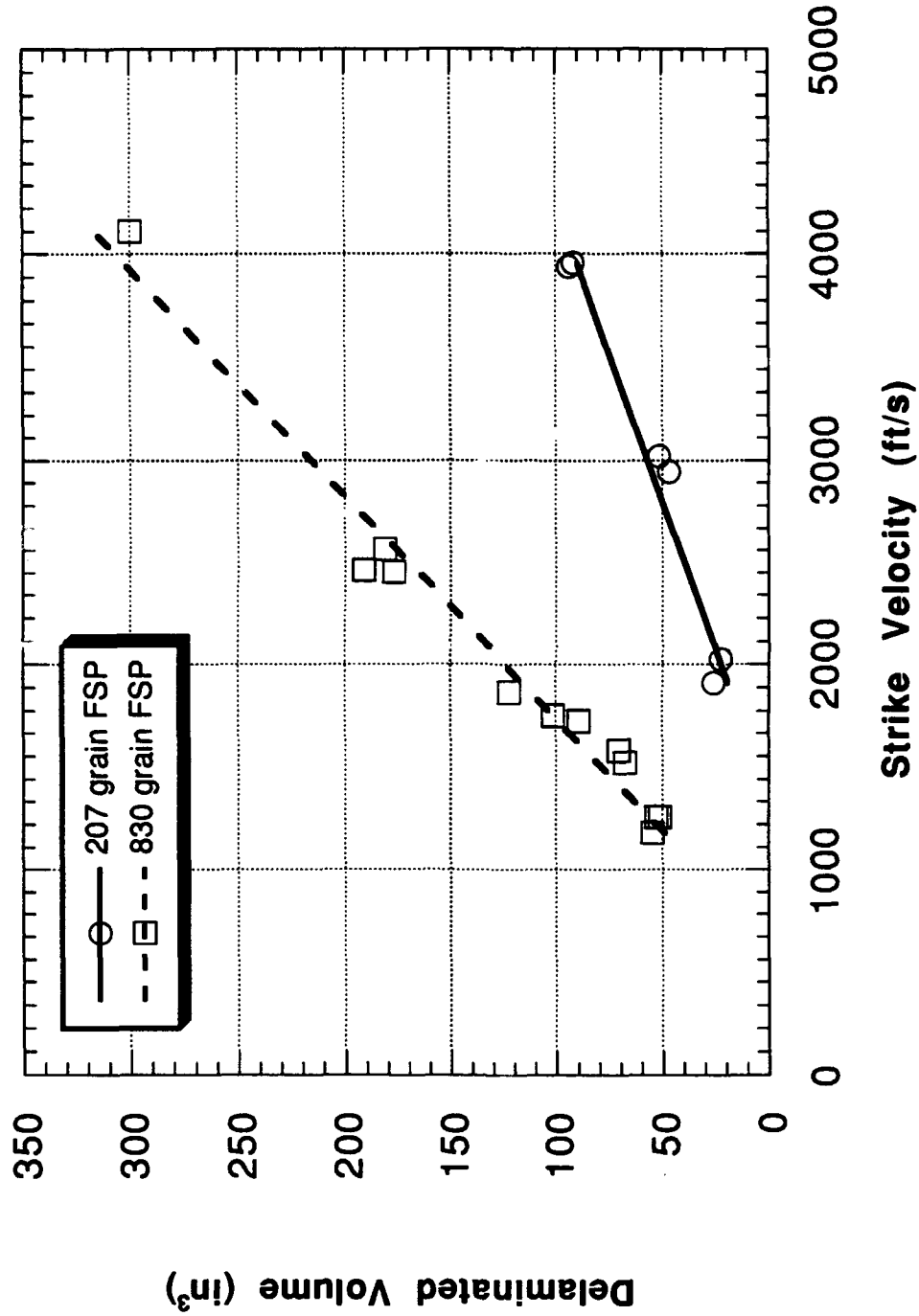


Figure 2.20 - Effect of Fragment Mass and Strike Velocity on Delaminated Volume of GRP Panel

—  $y = -19.439 + 0.014619x$   $R = 0.99195$   
 - -  $y = -2.8596 + 0.014535x$   $R = 0.96421$

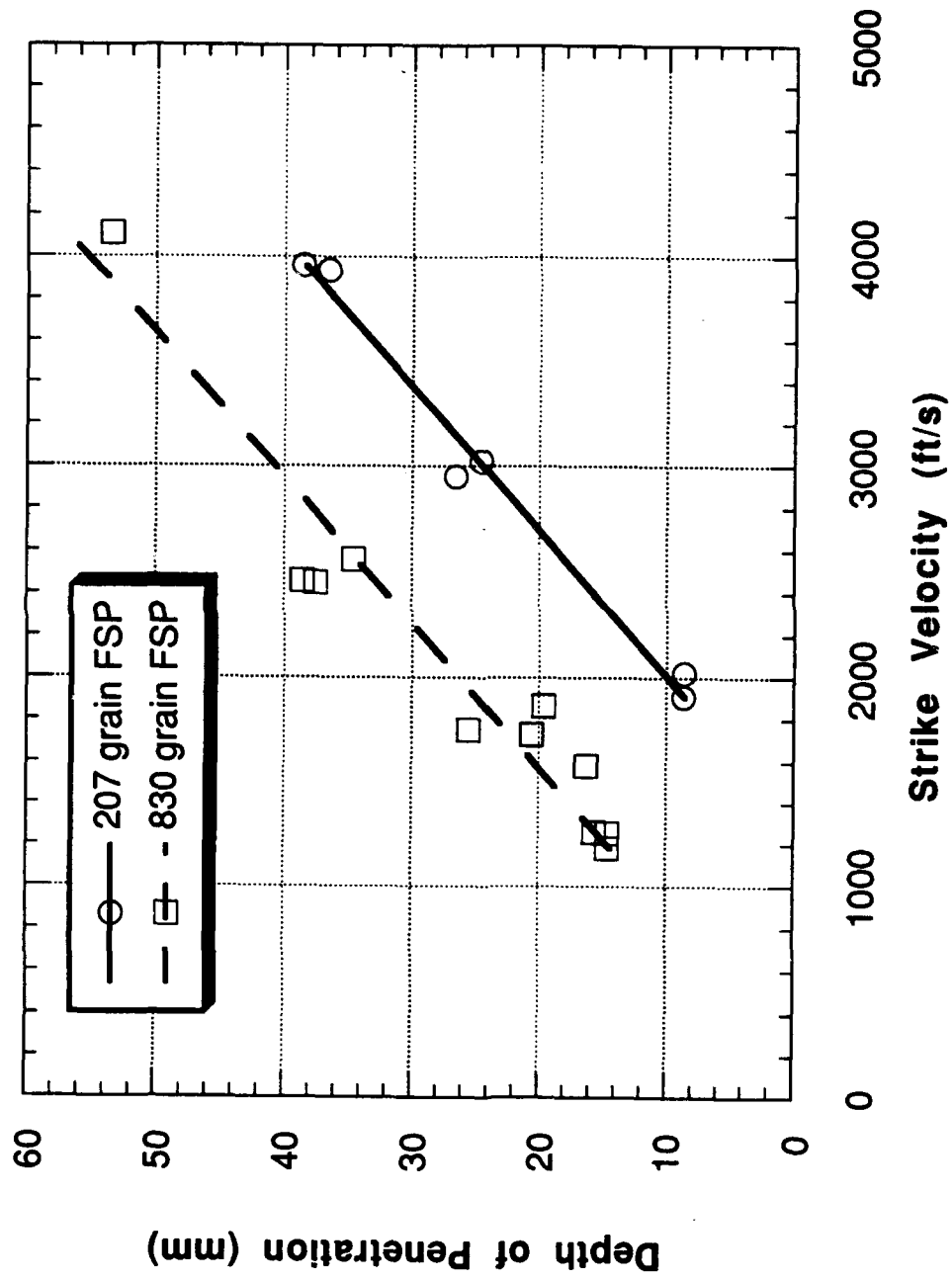


Figure 2.21 - Effect of Fragment Mass and Strike Velocity on Depth of Penetration in GRP



### c. Compressive Strength After Ballistic Impact

The compression test was chosen to measure residual strength of the GRP laminates after ballistic impact rather than a tensile or fatigue test. Testing of composite panels in compression constitutes the worst case loading condition; laminate failure modes under compressive loading are matrix controlled.

The fixture used in the compression test was a modified version of a compression test fixture developed by NASA. The specimen was gripped on the top, bottom, and sides. The side supports help keep the specimen from buckling. A small space at the top of the specimen between the sides and the upper fixture leaves room for the panel to compress unrestrained. All fixturing was made from 6061 T-6 aluminum alloy. Loads were applied to the fixture and specimen using a 600 kip universal test machine.

Prior to testing damaged panels, compression testing was conducted on undamaged S2-glass fabric reinforced laminates. Tests were conducted on panels ranging in thickness from approximately 1.0" to 1.7". Panel size for the nominal 1.0"-thick laminate was 20" X 20"; panels of thickness greater than 1.0" measured 10" X 20" in size to accommodate the maximum load of the test machine. For all tests (both undamaged and damaged panels) the loading axis was parallel with the panel long side. Since the fabric reinforcement is of balanced weave and delamination zones in the damaged panels are axisymmetric, no distinction was made in the two possible loading directions for any panel.

One control panel was photoelastically coated to determine if the loading was uniform across the cross sectional area of the specimen. There was no evidence of non-uniform loading. The load and time history was measured during each test; the maximum load was considered the failure load.

Compression test data for the undamaged laminates is tabulated in Table 2.3 and shown in Figure 2.22. The nominal strength was computed by dividing the maximum load by the entire cross-sectional area of the panel normal to the loading axis. Figure 2.22 shows that the laminate nominal compressive strength falls within a band over the thickness range examined. Mean strength for each pair of 10" X 20" panels and overall mean strength for all panels tested satisfy the minimum required value of 20 ksi specified in MIL-L-46197. Also, variation in length of the panel load-bearing side from 10" to 20" does not appear to affect laminate nominal compressive strength.

Compressive test data for all of the ballistically damaged laminates of Table 2.2 is contained in Table 2.4. Compressive strength of the GRP laminates after ballistic impact shows good reproducibility for replicate experiments.

**Table 2.3 Compression Test Data For Undamaged GRP Laminates**

<b>Laminate ID</b>	<b>Thickness (in)</b>	<b>Size (in)</b>	<b>Ply Count</b>	<b>Failure Load (lb)</b>	<b>Nominal Strength (psi)</b>
1378-A4	0.965	20x20	38	449500	23290
1378-C1A	1.370	10x20	53	260100	18985
1378-C1B	1.370	10x20	53	296100	21613
1378-C2A	1.400	10x20	53	338000	24143
1378-C2B	1.400	10x20	53	317500	22679
1378-B10-1A	1.650	10x20	67	386600	23430
1378-B10-1B	1.650	10x20	67	355400	21539

mean = 22240

sample standard deviation = 1723

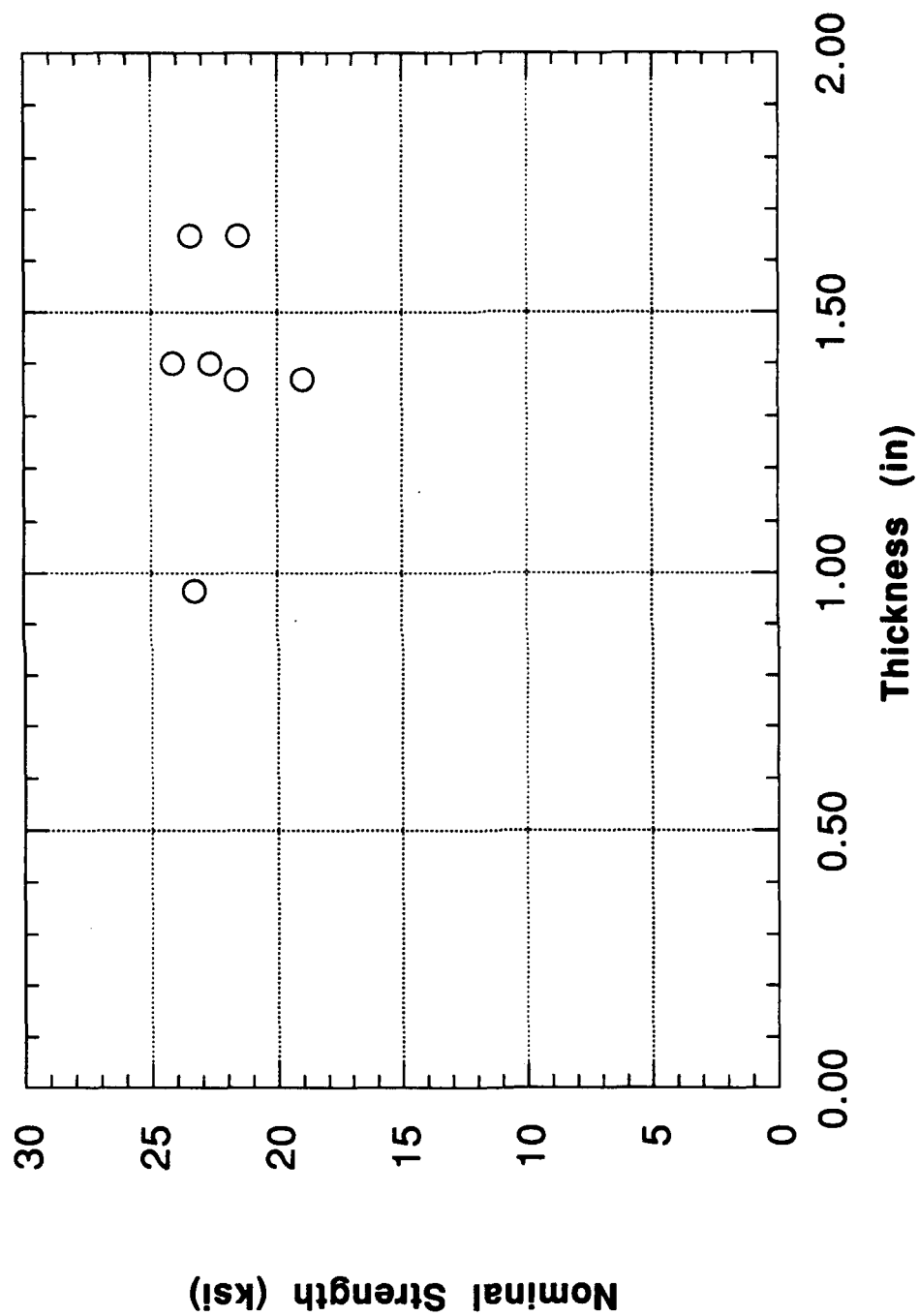


Figure 2.22 - Nominal Compressive Strength of Undamaged GRP Panels

Table 2.4 Compression Test Data For Ballistically Damaged GRP Laminates

Panel No.	Fragment Mass (grains)	Strike Velocity (ft/sec)	Failure Load (lb)	Nominal Strength (psi)
T44-93-1	207	1912	421100	12031
T44-93-2	207	2025	431800	12337
T44-93-3	207	3022	334700	9563
T44-93-4	207	2946	360400	10297
T44-93-5	207	3938	342400	9783
T44-93-6	207	3958	343500	9814
T 7-93-1	830	1522	304600	9230
T 7-93-2	830	1581	293000	8879
T28-93-1	830	1256	314000	8971
T28-93-2	830	1180	335700	9591
T28-93-3	830	1257	313300	8951
T26-93-1	830	1729	258400	7382
T26-93-2	830	1865	263300	7523
T26-93-3	830	1753	248000	7086
T27-93-1	830	2459	227500	6500
T27-93-2	830	2559	222000	6343
T27-93-3	830	2450	233000	6657
T45-93-1*	830	4100	261000	7457
T45-93-2	830	4109	487300	7182

\*Frontal titanium plate 14" X 14" X .83" clamped to GRP laminate

The nominal compressive strength of panels 20" X 20" X 1.7" in size after ballistic impact is shown in Figure 2.23 as a function of fragment mass and strike velocity. An initial, sharp drop in compressive strength with strike velocity is seen for both fragment sizes. However, compressive strength tends to level out at an asymptotic value of approximately 10 ksi for strike velocities greater than 3000 ft/sec in the case of the 207 grain fragment and approximately 7 ksi for strike velocities greater than 2000 ft/sec in the case of the 830 grain fragment. It is of interest to note that internal damage (delaminated volume) continues to increase linearly for strike velocities above 3000 ft/sec in the case of the 207 grain fragment and 2000 ft/sec in the case of the 830 grain fragment (Figure 2.20), while compressive strength remains virtually constant. This increase in delaminated volume with strike velocity holds only up to the panel limit velocity.

The compressive strength for the 1.7"-thick GRP laminate T45-93-1 showed a post-impact value comparable to laminate T26-93-2. The latter experienced direct impact with the 830 grain fragment at 1865 ft/sec; the former was the rear component of a titanium-faced binary target and, as such, experienced only minor penetration by the fragment and a titanium plug at the residual velocity of the fragment after it passed through the titanium plate. The implication, here, is that a GRP laminate acting as backup component for a metallic armor applique can suffer internal damage (loss of strength) without experiencing direct impact or projectile penetration.

Figure 2.24 shows nominal residual compressive strength for each GRP laminate tested in this work as a function of average percent delamination experienced by the panel. Average delamination as low as five percent reduces the panel compressive strength by approximately fifty percent; however, compressive strength falls off slowly as average delamination increases above five percent. A critical question for future work is whether the results of Figure 2.24 apply to panels of size other than tested here.

#### **d. Rear Surface Transient Displacement**

Measurement of rear surface maximum, transient displacement for the GRP laminate of each test shot was taken from the permanent deformation of a .020"-thick aluminum witness sheet placed directly behind the laminate. The aluminum witness sheet experienced the same transient displacement as the rear surface of the GRP laminate but, unlike the laminate, retained the maximum displacement profile as the permanent deformation. Measurements taken from flash radiographs of the rear surface displacement of reinforced plastic laminates struck by fragment simulators has shown this techniques to provide good accuracy. Rear surface displacement data is tabulated in Table 2.5; results for the GRP laminates of nominal thickness 1.7" are shown in Figure 2.25.

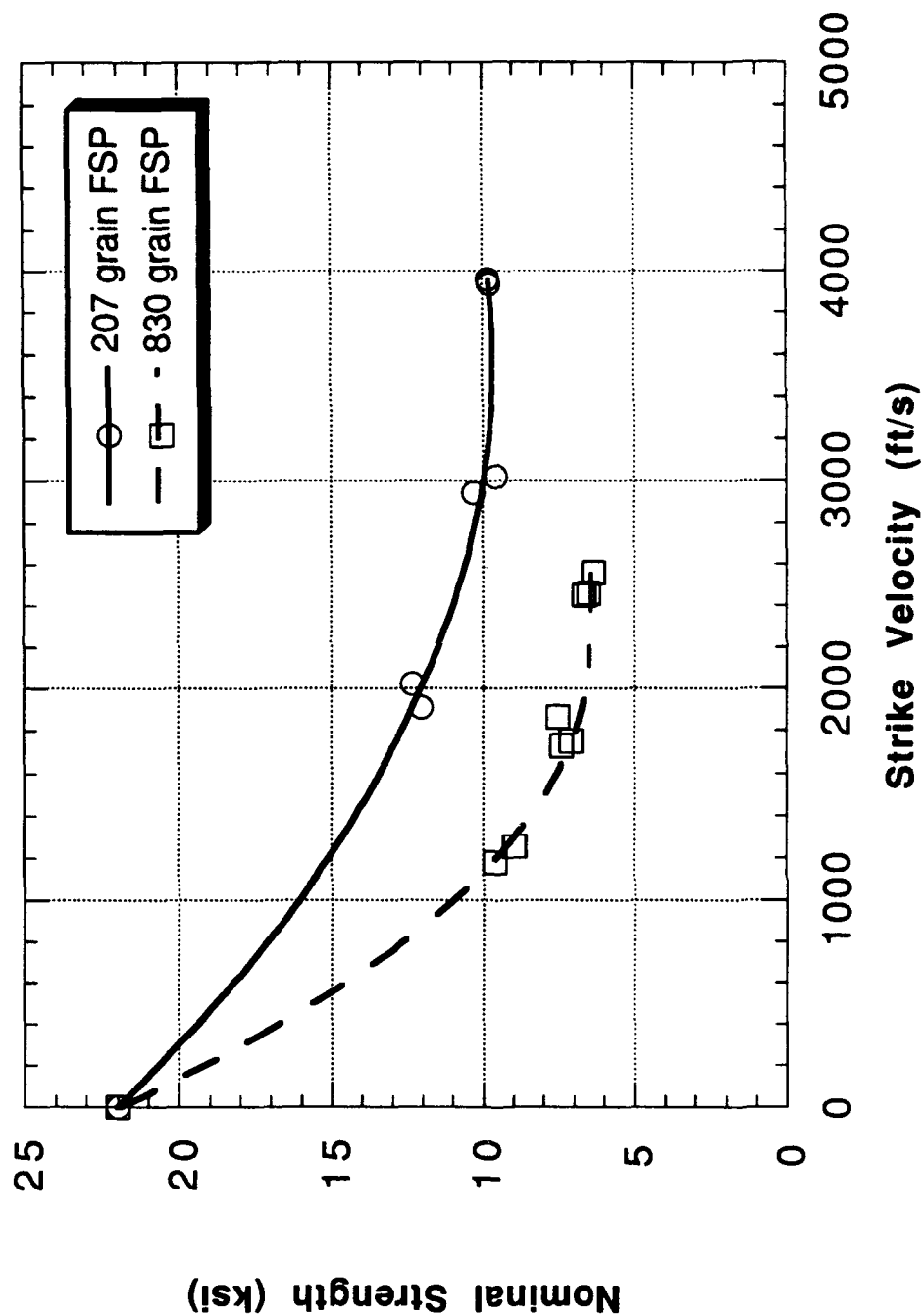


Figure 2.23 - Effect of Fragment Mass and Strike Velocity on Nominal Residual Compressive Strength of GRP Panels of Size 20"x 20" x 1.7"

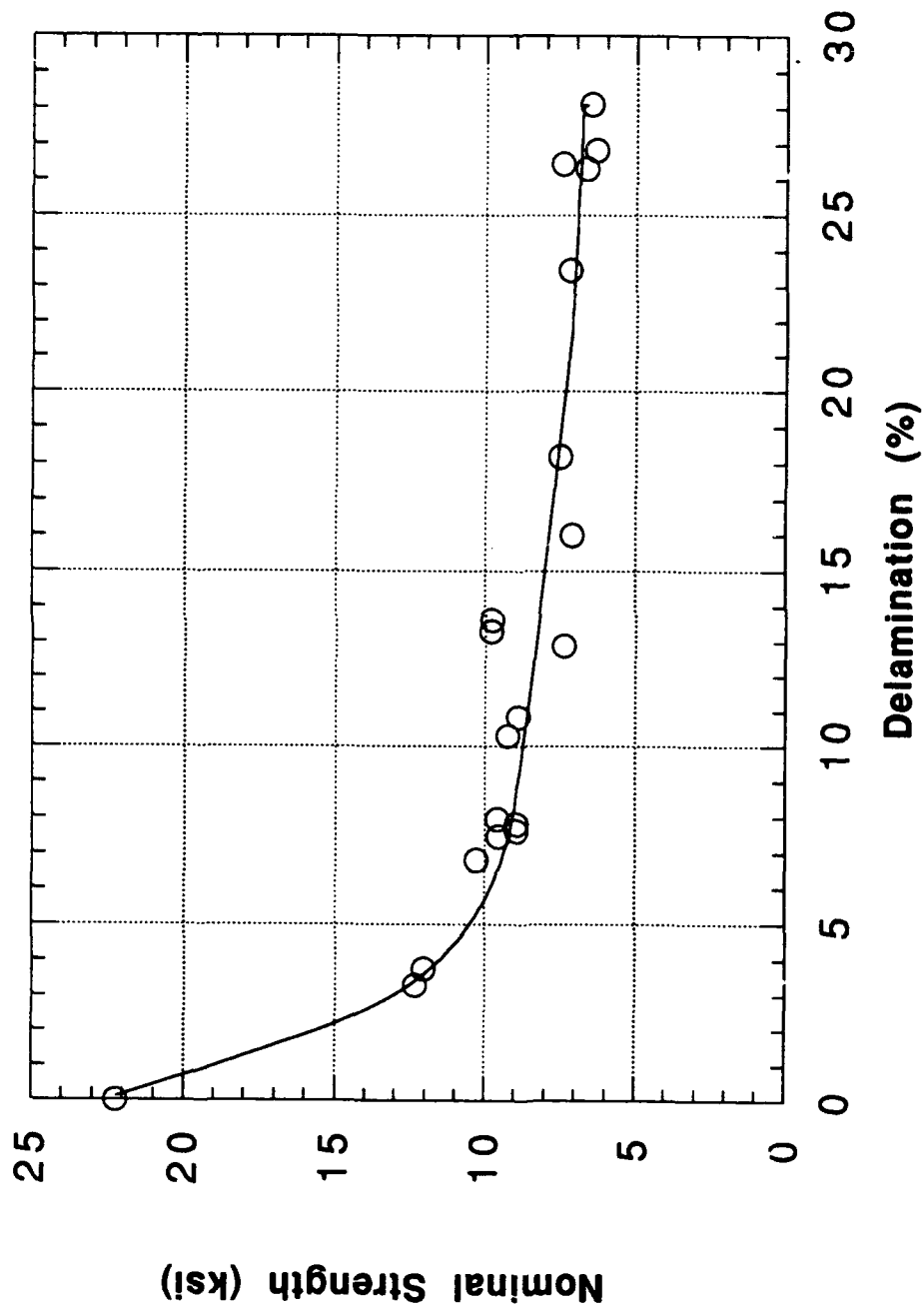


Figure 2.24 - Effect of GRP Panel Average Delamination on Nominal Residual Compressive Strength

Table 2.5 Rear Surface Displacement Of GRP Laminates

Panel No.	Panel <sup>1</sup> Thickness (in)	Fragment Mass (grains)	Strike Velocity (ft/sec)	Rear Surface Max Transient Displacement	
				(in)	(mm)
T44-93-1	1.73	207	1912	3/16	4.8
T44-93-2	1.73	207	2025	5/32	4.0
T44-93-3	1.73	207	3022	11/32	8.7
T44-93-4	1.73	207	2946	3/8	9.5
T44-93-5	1.73	207	3938	21/32	16.7
T44-93-6	1.73	207	3958	11/16	17.5
T 7-93-1	1.64	830	1522	3/8	9.5
T 7-93-2	1.63	830	1581	5/16	7.9
T28-93-1	1.71	830	1256	3/16	4.8
T28-93-2	1.73	830	1180	3/16	4.8
T28-93-3	1.68	830	1257	3/16	4.8
T26-93-1	1.73	830	1729	3/8	9.5
T26-93-2	1.68	830	1865	1/2	12.7
T26-93-3	1.68	830	1753	7/16	11.1
T27-93-1	1.70	830	2459	13/16	20.6
T27-93-2	1.69	830	2559	1	25.4
T27-93-3	1.68	830	2450	7/8	22.2
T45-93-1 <sup>2</sup>	1.72	830	4100	21/32	16.7
T45-93-2	2.95	830	4109	31/32	24.6

1. All panels measure 20" X 20" in size except for T45-93-2 which measures 23" X 23".

2. Frontal titanium plate 14" X 14" X .83" clamped to GRP laminate.



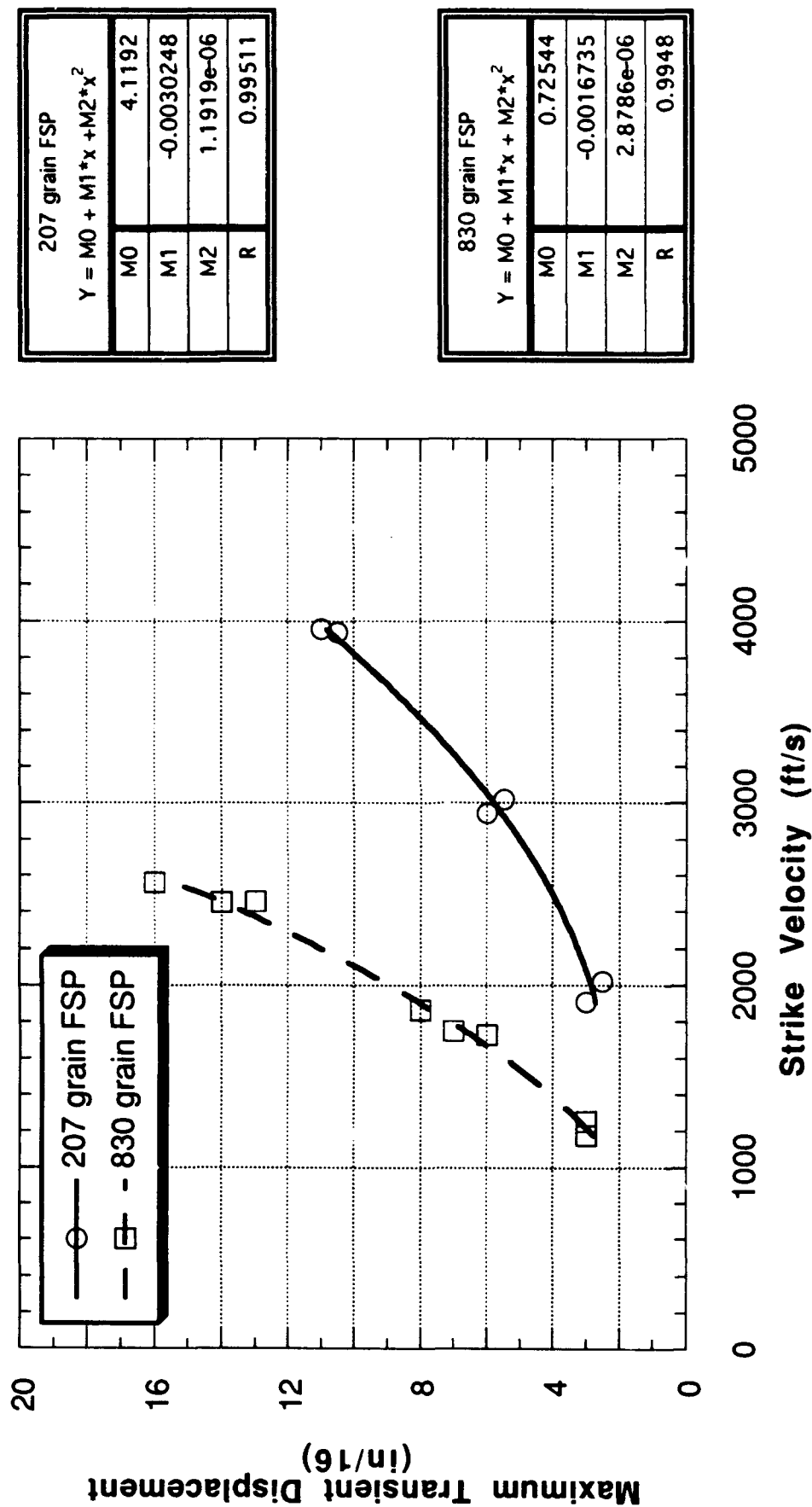


Figure 2.25 - Effect of Fragment Mass and Strike Velocity on Rear Surface Deformation of GRP Panels with 1.7" Nominal Thickness

## e. Summary of Results

Computed tomography inspection of glass-reinforced plastic panels has been shown to provide detailed, quantitative data on internal delamination resulting from fragment ballistic impact.

Fragment ballistic experiments conducted on S-2 glass-reinforced plastic panels demonstrate correlation of panel delamination volume with fragment mass and strike velocity. Replicate experiments show excellent reproducibility of results.

Corollary results include measurement of fragment depth of penetration in S-2 glass-reinforced plastic laminate and maximum displacement of laminate rear surface during fragment impact. These results were obtained to assist development of dynamic behavior simulation models for the laminate material.

Compression testing of both undamaged and ballistically damaged S-2 glass-reinforced plastic panels shows that test results are reproducible for replicate experiments and that compressive strength of single-thickness panels after fragment impact can be related to fragment mass and strike velocity; compressive strength after fragment impact did not correlate with impact kinetic energy.

The most important result of this chapter is a proposed correlation of compressive strength of S-2 glass-reinforced plastic panels after ballistic impact with panel average delamination. The correlation shows an immediate drop in compressive strength to approximately 50% of the undamaged value for as little as 5% average delamination. However, compressive strength falls off slowly as delamination increases above five percent. Future work will further test this result.

A preview experiment consisting of a fragment impact on a titanium-faced glass-reinforced plastic panel shows that glass-reinforced plastic laminates can suffer extensive delamination and loss of strength without direct impact by a kinetic energy threat. Induced ballistic damage to glass-reinforced laminates behind applique armor is a major topic for follow-on work.

The objectives defined for this study have been satisfied. This work has also provided a clear and logical set of follow-on questions and issues as well as the experimental methods to pursue these issues.

### 3. DYNAMIC CHARACTERIZATION

#### (a) . Background:

The development of armor systems is a complex process which requires performance of ballistic experiments as well as computer simulations of ballistic events in order to fully understand the performance of armor material. Simulations are conducted using wave propagation / finite element codes; such codes require dynamic properties of materials for carrying out analysis of ballistic events. Thus, a knowledge of the response of glass reinforced plastic (GRP), under dynamic loading is essential to develop a better understanding of its performance as a structural armor material. This chapter describes experiments performed to measure the mechanical properties of GRP under quasi-static and dynamic loading. It is divided into three sections that describe the experiments performed (i) to define the material model with a full set of elastic constants, (ii) to obtain deformation curves for compressive and tensile loading under quasi-static and medium strain rates ( $10^{-4}$  to  $1 \text{ s}^{-1}$ ), and (iii) deformation under compression at high strain rate. The results of these experiments are discussed and summarized in the last section of this chapter.

For purpose of this chapter, the thickness direction along the fiber axis was designated as the z or  $\langle 001 \rangle$  direction; the other two orthogonal directions were designated as x or  $\langle 100 \rangle$  and y or  $\langle 010 \rangle$  directions. Ultrasonic wave velocities were measured in  $\langle 100 \rangle$ ,  $\langle 010 \rangle$ ,  $\langle 001 \rangle$ ,  $\langle 110 \rangle$ ,  $\langle 101 \rangle$ , and  $\langle 011 \rangle$  directions to determine the nine independent elastic constants for a 3-D orthotropic material. Orientations are shown in Figure 3.1.

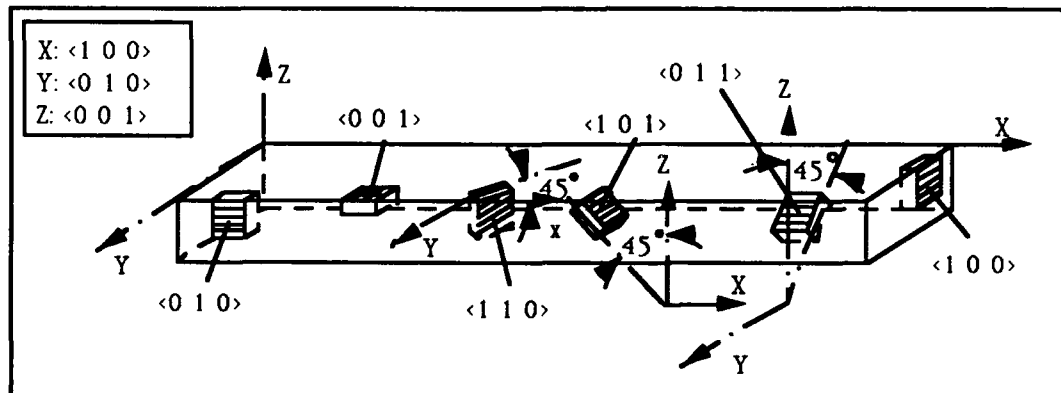


Figure 3.1 GRP specimen orientations.

Photomicrographs in the  $\langle 100 \rangle$  and  $\langle 001 \rangle$  orientations of GRP show that the material is not homogeneous or uniform with respect to fiber weave geometry and contains voids, (Figure 3.2) Consequently, density variation must be considered in determination of elastic constants.

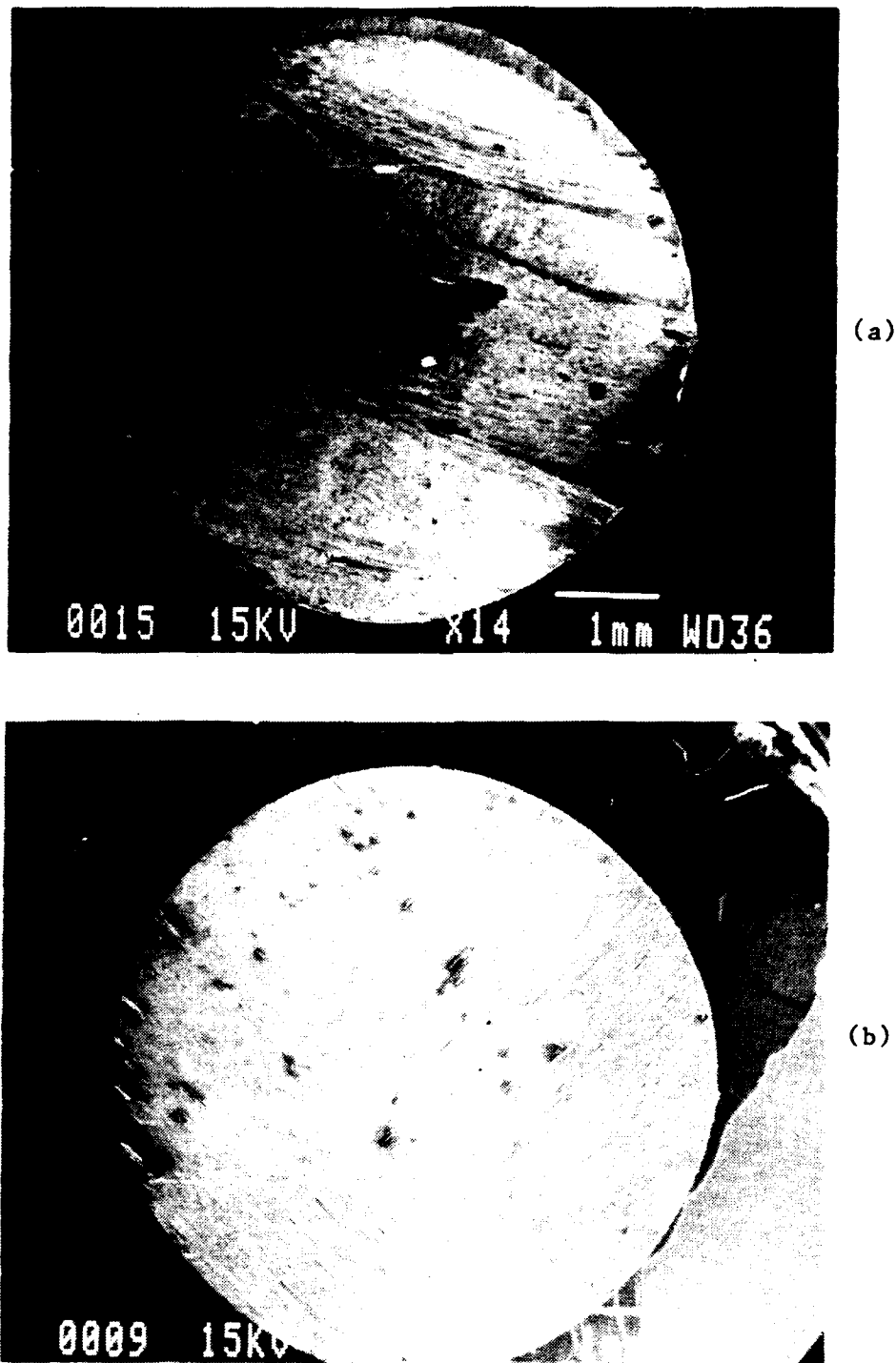


Figure 3.2 Photomicrographs of typical specimens (a) Orientation  $\langle 110 \rangle$  , (b) Orientation  $\langle 001 \rangle$ .

Specimen densities were measured using Archimedes method Densities of GRP composite specimens used in this chapter are tabulated in Table 3.1. Numbers in square brackets are the number of test specimens. A statistical analysis of the density data showed no significant difference in density with respect to specimen orientation or shape; hence the value of  $1.949 \pm 0.030 \text{ Mg/m}^3$  is used when needed.

Table 3.1 Densities of GRP specimens in ( $\text{Mg/m}^3$ ).

SPECIMEN ORIENTATION	COMPRESSION SPECIMENS						ULTRASONIC SPECIMENS		
	RECTANGULAR			CIRCULAR					
<100>	1.956 ±	0.015	[15]	1.948 ±	0.008	[5]	1.955 ±	0.007	[4]
<010>	1.964 ±	0.033	[13]	1.967 ±	0.010	[5]	1.958 ±	0.011	[4]
<001>	1.938 ±	0.014	[12]	1.932 ±	0.010	[5]	1.926 ±	0.034	[4]
<110>	-			-			1.946 ±	0.048	[4]
<101>	-			-			1.964 ±	0.004	[4]
<011>	-			-			1.968 ±	0.026	[4]
AVERAGE VALUES	1.950 ±	0.031	[40]	1.947 ±	0.030	[15]	1.952 ±	0.036	[24]
$1.949 \pm .030 \text{ Mg/M}^3$									

#### (b). Elastic Constants:

##### Experimental Procedure

Elastic constants of GRP are obtained from phase velocities of ultrasonic waves. Phase velocity is defined as the velocity of individual cycles in a continuous wave, and is given by

$$V = f\lambda = \omega/k \quad (3.1)$$

where  $V$  is the phase velocity,  $f$  is the frequency of the ultrasonic wave,  $\lambda$  is the wavelength,  $\omega$  is the angular frequency  $2\pi f$ , and  $k$  is the wave number  $2\pi/\lambda$ . If the phase velocity is non-dispersive, i.e., it does not vary with frequency, then elastic waves remain unchanged traveling through the thickness of specimen. The implication is that the elastic constants are not frequency dependent.

At an ultrasonic frequency, with wavelength being much smaller than specimen cross-sectional dimension, but larger than the fiber diameter and spacing the phase velocity, ( $V$ ) is given by

$$V = (C/\rho)^{1/2} \quad (3.2)$$

where C is the appropriate elastic constant.

This relation is based on the propagation of a plane wave front. The wave fronts are considered to be planar when the dimension of the specimen in the wave propagation direction is less than the Fresnel limit (F), i.e.,

$$L = F r^2 / \lambda \quad (3.3)$$

where L is the specimen length and r is the radius of the transducer. The Fresnel region will be greatest for the case of longitudinal waves. The number of cycles (N) of delay of the wave traveling in the specimen is  $N = L/\lambda$ . From (3.3) the Fresnel region requirement is met for those frequencies such that

$$N \geq (L/r)^2 \quad (3.4)$$

Since shear wavelength is shorter than longitudinal wavelength at the same frequency, only longitudinal wavelength is used to calculate thickness requirements for specimens used in ultrasonic wave experiments. For these experiments a frequency range of between 0.2 and 2 MHz was used, with a 1.27 cm radius transducer. Wave velocity measurements could not be made at higher frequencies due to the limitation of the transducers frequency response. Using equation 3.3 with a frequency of 0.2 MHz and transducer radius of 1.27 cm., the Fresnel region is 9.76 mm. Therefore, specimens used were 3.2 mm and 9.5 mm thick to insure a plane wave through the specimen. Lateral cross section of the specimen were square with a side of 37 mm to be compatible with transducer dimensions.

Phase velocity measurements were made at frequencies between 0.2 MHz and 2 MHz. For these phase velocity measurements, an image superposition method [3.1] similar to the pulse - echo overlap method [3.2] was used. The image superposition method employs bursts of ultrasonic vibrations rather than continuous waves. The bursts consist of a continuous wave amplitude modulated by sinusoidal pulses synchronized with the wave. The repetition rate of the pulses is 1/2048 times the frequency of the continuous wave. The pulse duration is made long enough to encompass many cycles of the wave in order to make it as monochromatic as possible. Images of the pulses are superposed by control of the timing of pulses relative to the timing of oscilloscope sweeps. The control of timing is done by means of digital circuitry.

Phase velocity data is obtained by comparing the phase of individual cycles as they enter and leave a specimen. This is done by adjusting the advance of bursts applied to the specimen so that lead time equals travel time of individual cycles. Then the images of individual cycles coincide as they are presented alternately on the oscilloscope.

These measurements are done with two pairs of identical transducers. Two methods were adopted to obtain wave number as a function of frequency. In the first method, one pair is coupled together, and the other pair is separated by and coupled to a specimen. In the second method, each pair of transducers is coupled to one of two specimens of the same orientation but differing in thicknesses to generate wave number vs frequency data. In both methods, one transducer of each pair is connected in parallel to the signal source. The other two transducers are connected to the two signal inputs of the oscilloscope through two preamplifiers.

The signal frequency is started at the lowest frequency at which the travel time through the specimen is the inverse of that frequency. From that point, the frequency is gradually increased and recorded along with the number of cycles of delay needed to keep the images superimposed. An additional record may be kept of the number of cycles needed to match the envelope of the burst for group velocity determination.

For each set of data,  $n/L$  (number of cycles/specimen length, i.e.,  $1/l$ ) was plotted vs frequency. The data generated in this manner for GRP were found to vary linearly. Hence, it was not necessary to adjust the phase velocity data so as to bring the intercept to the origin. The details of this technique are given in Reference [3.1].

The lay-up of GRP prepregs suggested that the lowest symmetry the cured material could have is orthotropic. This implied that it could have at the most 9 independent elastic constants for a 3D orthotropic medium. The elastic constants matrix  $[C]$  for an orthotropic material is

$$[C] = \begin{bmatrix} C_{11} & C_{12} & C_{13} & 0 & 0 & 0 \\ C_{12} & C_{22} & C_{23} & 0 & 0 & 0 \\ C_{13} & C_{23} & C_{33} & 0 & 0 & 0 \\ 0 & 0 & 0 & C_{44} & 0 & 0 \\ 0 & 0 & 0 & 0 & C_{55} & 0 \\ 0 & 0 & 0 & 0 & 0 & C_{66} \end{bmatrix} \quad (3.5)$$

The elastic compliance matrix  $[S]$  is the inverse of matrix  $[C]$ .

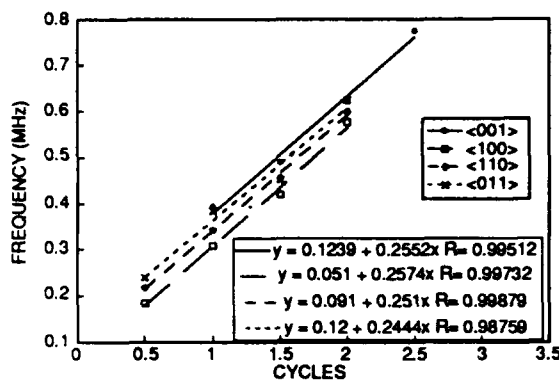
The nature of ultrasonic velocities and their relations to the elastic constants are given in Table 3.2. These relations are obtained from the Christoffel relations for wave propagation in an orthorhombic, i.e., orthotropic solid [3.3]. In this table, L and S denote longitudinal and shear waves, respectively, and prefix Q denotes the quasi nature of these respective waves.

Table 3.2 Wave velocity types and relations to elastic constants ( $C_{ij}$ ) of an orthotropic composite as expressed by the products of density ( $\rho$ ) and squared wave velocity ( $V$ ).

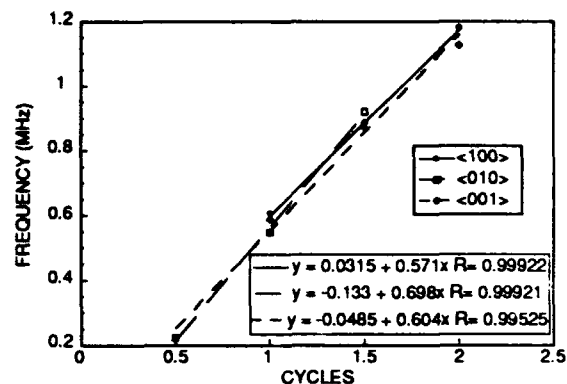
Wave Velocities					
Mode	Direction of		Wave Velocity	$\rho V^2$	Eq.
	Propagation	Particle Motion			
L	$\langle 100 \rangle$	$\langle 100 \rangle$	$V_1$	$C_{11}$	3.6
S	$\langle 100 \rangle$	$\langle 010 \rangle$	$V_2$	$C_{66}$	3.7
S	$\langle 100 \rangle$	$\langle 001 \rangle$	$V_3$	$C_{55}$	3.8
L	$\langle 010 \rangle$	$\langle 010 \rangle$	$V_4$	$C_{22}$	3.9
S	$\langle 010 \rangle$	$\langle 100 \rangle$	$V_5$	$C_{66}$	3.10
S	$\langle 010 \rangle$	$\langle 001 \rangle$	$V_6$	$C_{44}$	3.11
L	$\langle 001 \rangle$	$\langle 001 \rangle$	$V_7$	$C_{33}$	3.12
S	$\langle 001 \rangle$	$\langle 100 \rangle$	$V_8$	$C_{55}$	3.13
S	$\langle 001 \rangle$	$\langle 010 \rangle$	$V_9$	$C_{44}$	3.14
QL	$\langle 110 \rangle$	$\langle 110 \rangle$	$V_{10}$	$0.5 C_{66} + 0.25 (C_{11} + C_{22}) +$ $0.5 [(C_{12} + C_{66})^2 + 0.25 (C_{22} - C_{11})^2]^{1/2}$	3.15
QS	$\langle 110 \rangle$	$\langle 110 \rangle$	$V_{11}$	$0.5 C_{66} + 0.25 (C_{11} + C_{22}) -$ $0.5 [(C_{12} + C_{66})^2 + 0.25 (C_{22} - C_{11})^2]^{1/2}$	3.16
S	$\langle 110 \rangle$	$\langle 001 \rangle$	$V_{12}$	$0.5 (C_{55} + C_{44})$	3.17
QL	$\langle 101 \rangle$	$\langle 101 \rangle$	$V_{13}$	$0.5 C_{55} + 0.25 (C_{11} + C_{33}) +$ $0.5 [(C_{13} + C_{55})^2 + 0.25 (C_{11} - C_{33})^2]^{1/2}$	3.18
QS	$\langle 101 \rangle$	$\langle 101 \rangle$	$V_{14}$	$0.5 C_{55} + 0.25 (C_{11} + C_{33}) -$ $0.5 [(C_{13} + C_{55})^2 + 0.25 (C_{11} - C_{33})^2]^{1/2}$	3.19
S	$\langle 101 \rangle$	$\langle 010 \rangle$	$V_{15}$	$0.5 (C_{66} + C_{44})$	3.20
QL	$\langle 011 \rangle$	$\langle 011 \rangle$	$V_{16}$	$0.5 C_{44} + 0.25 (C_{22} + C_{33}) +$ $0.5 [(C_{23} + C_{44})^2 + 0.25 (C_{22} - C_{33})^2]^{1/2}$	3.21
QS	$\langle 011 \rangle$	$\langle 011 \rangle$	$V_{17}$	$0.5 C_{44} + 0.25 (C_{22} + C_{33}) -$ $0.5 [(C_{23} + C_{44})^2 + 0.25 (C_{22} - C_{33})^2]^{1/2}$	3.22
S	$\langle 011 \rangle$	$\langle 100 \rangle$	$V_{18}$	$0.5 (C_{66} + C_{55})$	3.23

Within the range of frequency of measurements none of the wave velocity modes showed dispersion. Figure. 3.3 shows consistency of the phase velocities through a plot of frequency vs. wave number for some of the velocity modes.





(a) Longitudinal Mode



(b) Shear Mode

## Results

The measured values of wave velocities in 24 different specimens of GRP composites are given in Table 3.3. The results are used:

- (i) to show the extent of variability in the measurement of wave velocities in different specimens of the GRP composite,
- (ii) to determine the symmetry of GRP composite and the number of independent elastic constants required to describe its elastic behavior,
- (iii) to determine the values of the independent elastic constants from these wave velocity measurements, and
- (iv) to compare the elastic constants obtained from the higher ultrasonic frequency measurements with those from quasi-static conditions.

Table 3.3 shows that variation in the values of even the pure longitudinal and shear modes of propagation along  $\langle 100 \rangle$ ,  $\langle 010 \rangle$ , and  $\langle 001 \rangle$  directions exceed the estimated errors for this type of experiment. It is also noticed that within the error of measurement variation in density of GRP specimens with the same orientation do not affect the values of wave velocities.

Table 3.3 Ultrasonic wave velocities and density of GRP specimens.

PAIR	COMBINATION		VELOCITIES AND PROPAGATION					
	SPEC No.	DENSITY (g/cc)	LENGTH (mm)	(km/sec) LONGITUDINAL		SHEAR POLARIZATION		SHEAR POLARIZATION
1a-2	1-1	1.960	2.920					
		1.955	9.552	4.04		1.58		1.57
1a-1	1-1	1.948	3.185	4.15				
		1.949	9.552	4.13		1.43		1.42
1a-2	1-2	1.960	2.920	4.16				
		1.949	9.523	3.82 <010>		1.60 <100>		1.57 <001>
				$4.04 \pm .284$ V <sub>4</sub>		$1.53 \pm .186$ V <sub>5</sub>		$1.52 \pm .173$ V <sub>6</sub>
2a-1	2-1	1.929	3.105					
		1.928	9.509	3.21		1.57		1.55
2-2	2a-2	1.945	9.541					
		1.904	3.133	3.21		1.36		1.43
2a-2	2-1	1.904	3.133					
		1.928	9.509	3.22 <001>		1.63 <100>		1.62 <010>
				$3.21 \pm .012$ V <sub>7</sub>		$1.52 \pm .284$ V <sub>8</sub>		$1.53 \pm .192$ V <sub>9</sub>
3a-1	3-1	1.959	3.212	4.05				
		1.956	9.558	3.98		1.72		1.70
3a-2	3-2	1.955	3.154	3.86				
		1.950	9.538	4.03 <100>		1.63 <010>		1.56 <001>
				$3.98 \pm .170$ V <sub>1</sub>		$1.68 \pm .127$ V <sub>2</sub>		$1.63 \pm .198$ V <sub>3</sub>
4a-1	4b-1	1.972	9.556					
		1.919	3.366	3.80		1.55		2.36
4a-2	4b-2	1.960	9.566					
		1.935	3.348	3.86 <110>		1.37 <001>		2.19 <110>
				$3.83 \pm .085$ V <sub>10</sub>		$1.46 \pm .255$ V <sub>12</sub>		$2.28 \pm .240$ V <sub>11</sub>
5a-1	5-1	1.967	3.206					
		1.962	9.565	3.44		1.64		1.58
5a-2	5-2	1.965	3.210					
		1.964	9.561	3.45 <101>		1.64 <010>		1.56 <101>
				$3.45 \pm .028$ V <sub>13</sub>		$1.64 \pm .014$ V <sub>15</sub>		$1.57 \pm .028$ V <sub>14</sub>
6a-2	6-2	1.982	3.183					
		1.960	9.521	3.41		1.51		1.52
6a-1	6-1	1.976	3.168					
		1.954	9.519	3.43 <011>		1.55 <100>		1.60 <011>
				$3.42 \pm .028$ V <sub>16</sub>		$1.53 \pm .056$ V <sub>18</sub>		$1.56 \pm .11$ V <sub>17</sub>

For example, the values of longitudinal and shear velocity modes in  $\langle 001 \rangle$  directions do not vary significantly even when the densities of the specimens vary between 1.904 and 1.945 Mg/m<sup>3</sup> or when these measurements are carried out on a pair of these specimens with varying densities. Hence, the average value of a specific velocity mode is assumed to be the representative value for that mode. Values of the various velocity modes in GRP composite are given in Table 3.4.

Table 3.4 Velocity modes measured in GRP composite.

Wave Velocities				
Direction of				
Mode	Propagation	Particle Motion		km/s
L	$\langle 100 \rangle$	$\langle 100 \rangle$	V <sub>1</sub>	3.98±0.170
S	$\langle 100 \rangle$	$\langle 010 \rangle$	V <sub>2</sub>	1.68±0.127
S	$\langle 100 \rangle$	$\langle 001 \rangle$	V <sub>3</sub>	1.63±0.198
L	$\langle 010 \rangle$	$\langle 010 \rangle$	V <sub>4</sub>	4.04±0.284
S	$\langle 010 \rangle$	$\langle 100 \rangle$	V <sub>5</sub>	1.53±0.186
S	$\langle 010 \rangle$	$\langle 001 \rangle$	V <sub>6</sub>	1.52±0.173
L	$\langle 001 \rangle$	$\langle 001 \rangle$	V <sub>7</sub>	3.21±0.012
S	$\langle 001 \rangle$	$\langle 100 \rangle$	V <sub>8</sub>	1.52±0.284
S	$\langle 001 \rangle$	$\langle 010 \rangle$	V <sub>9</sub>	1.53±0.192
QL	$\langle 110 \rangle$	$\langle 110 \rangle$	V <sub>10</sub>	3.83±0.085
QS	$\langle 110 \rangle$	$\langle 110 \rangle$	V <sub>11</sub>	2.28±0.240
S	$\langle 110 \rangle$	$\langle 001 \rangle$	V <sub>12</sub>	1.46±0.213
QL	$\langle 101 \rangle$	$\langle 101 \rangle$	V <sub>13</sub>	3.45±0.028
QS	$\langle 101 \rangle$	$\langle 101 \rangle$	V <sub>14</sub>	1.57±0.028
S	$\langle 101 \rangle$	$\langle 010 \rangle$	V <sub>15</sub>	1.64±0.014
QL	$\langle 011 \rangle$	$\langle 011 \rangle$	V <sub>16</sub>	3.43±0.028
QS	$\langle 011 \rangle$	$\langle 011 \rangle$	V <sub>17</sub>	1.56±0.113
S	$\langle 011 \rangle$	$\langle 100 \rangle$	V <sub>18</sub>	1.53±0.056

This table indicates that following equalities hold among the various velocity modes in GRP composite.

$$V_1^2 = V_4^2 \quad (3.24)$$

$$V_2^2 = V_5^2 \quad (3.25)$$

$$V_3^2 = V_6^2 = V_8^2 = V_9^2 = V_{12}^2 \quad (3.26)$$

$$V_{15}^2 = 0.5 (V_2^2 + V_3^2) = V_{18}^2 \quad (3.27)$$

$$V_{10}^2 + V_{11}^2 = V_2^2 + V_1^2 \quad (3.28)$$

$$V_{13}^2 + V_{14}^2 = V_3^2 + 0.5 (V_1^2 + V_7^2)$$

$$= v_{16}^2 + v_{17}^2 \quad (3.29)$$

The implication of equations (3.24) - (3.29) is that the symmetry of the GRP composite is that of a transversely isotropic material. A material with this symmetry has six independent elastic constants. These are  $C_{11}$ ,  $C_{33}$ ,  $C_{44}$ ,  $C_{66}$ ,  $C_{12}$ , and  $C_{13}$ . There is no unique method to calculate the values of these six elastic constants from the eighteen velocity modes measured in GRP composite. One of the more reliable methods is adopted here to calculate these six elastic constants by first determining diagonal terms,  $C_{11}$ ,  $C_{33}$ ,  $C_{44}$ , and  $C_{66}$  from pure modes. Explicitly,  $C_{11}$  from  $v_{11}^2$  and  $v_{14}^2$ ,  $C_{33}$  from  $v_{77}^2$ ,  $C_{44}$  from  $v_{33}^2$ ,  $v_{66}^2$ ,  $v_{88}^2$ ,  $v_{99}^2$ , and  $C_{66}$  from  $v_{22}^2$  and  $v_{55}^2$ . The non diagonal constant  $C_{12}$  is then calculated from  $v_{10}^2$  and  $v_{13}^2$ . Also,  $C_{13}$  from  $v_{11}^2$ . The values of the six elastic constants calculated in the above manner are displayed in Table 3.5.

Tables 3.5 Values of elastic constants ( $C_{ij}$ ) and elastic compliances ( $S_{ij}$ ) of GRP composite.

Elastic constants	GPa	Elastic compliances	GPa <sup>-1</sup>
$C_{11}$	$31.55 \pm 3.8$	$S_{11}$	$0.045039 \pm .012$
$C_{33}$	$20.12 \pm 0.40$	$S_{33}$	$0.062074 \pm .0128$
$C_{44}$	$4.63 \pm 1.22$	$S_{44}$	$0.2160 \pm .05$
$C_{66}$	$4.94 \pm 1.31$	$S_{66}$	$0.2024 \pm .06$
$C_{12}$	$15.86 \pm 4.53$	$S_{12}$	$-0.01869 \pm .0082$
$C_{13}$	$9.75 \pm 3.83$	$S_{13}$	$-0.012766 \pm .0077$

In the calculations of the elastic constants the average value of the specimens density was used, i.e.,  $1.949 \text{ Mg/m}^3$ . The values of elastic compliance  $S_{ij}$  were obtained by inverting the matrix  $[C]$ . Finally, the values of the elastic compliances given in Table 3.5 yield the following estimates of Young's modulus in  $\langle 001 \rangle$  and  $\langle 100 \rangle$  directions  $16.1 \pm 3.3$ , and  $22.2 \pm 5.96$  GPa, respectively. The estimates of Poisson's ratios  $\nu_{12}$ ,  $\nu_{13}$ , and  $\nu_{31}$  are calculated to be  $0.41 \pm 0.14$ ,  $0.28 \pm 0.22$ , and  $0.20 \pm 0.14$ , respectively.

### **(c).Quasi-Static and Medium Strain Rate Tensile and Compressive Properties:**

This section deals with the experimental program to determine deformation of GRP composite under uniaxial compression and tension at two strain rates. The two strain rates are  $10^{-4} \text{ s}^{-1}$  and  $1 \text{ s}^{-1}$ . A medium strain rate machine (MSRM) [3.4] was used to carry out these experiments. The orientation of specimens used in tension experiments were  $\langle 100 \rangle$  and  $\langle 010 \rangle$ , see Figure 3.1. Compression experiments were conducted in three directions  $\langle 100 \rangle$ ,  $\langle 010 \rangle$ , and  $\langle 001 \rangle$ . The facilities, test procedures and results are described in the following paragraphs.

#### **Experimental Procedure**

The tension and compression tests were carried out in the Medium Strain Rate Machine (MSRM). The MSRM has a 140,000 pounds static load capacity. There are two operating modes: close loop mode and open loop mode. In the closed loop mode, the MSRM has the same characteristics typical of servo-hydraulic controlled test machines. A strain / load / displacement rate up to  $1 \text{ s}^{-1}$  can be achieved in the closed loop mode. In the open loop mode, the hydraulic fluid is replaced by nitrogen gas. A fast-acting valve is used to release the gas from the top or bottom of an actuating piston creating a pressure differential which moves the piston. The loading rate in the open loop mode is controlled by the gas pressure, stroke of the piston, and the orifice size selected for the fast-acting valve. A nominal rate of up to  $50 \text{ s}^{-1}$  can be achieved depending on the ductility of the specimen. Stress and strain measurements were made by means of load cells, strain gages, and linear variable differential transformer (LVDT). The strain gages are used to measure a max strain up to 5%. The LVDT was used to measure displacements corresponding to strains in the specimen above 5%. The LVDT displacement measurements together with the specimens gage length and a correction factor were used to obtain strains greater than 5%. The LVDT data was corrected for compliance of the test fixtures by measuring the displacement of the fixtures without specimen. A computer with a fast data acquisition card and a digital oscilloscope were used to control the MSRM and record load, strain, displacement, and time during the conduction of experiments. For all experiments conducted the measurement errors from the strain and load systems were less than 2.0 percent .

Tension and compression testing was conducted at strain rates of  $10^{-4} \text{ s}^{-1}$  and  $1 \text{ s}^{-1}$ . The tension tests were conducted in accordance with ASTM D3095 standard, Figure 3.4 is a sketch of the tension specimen.

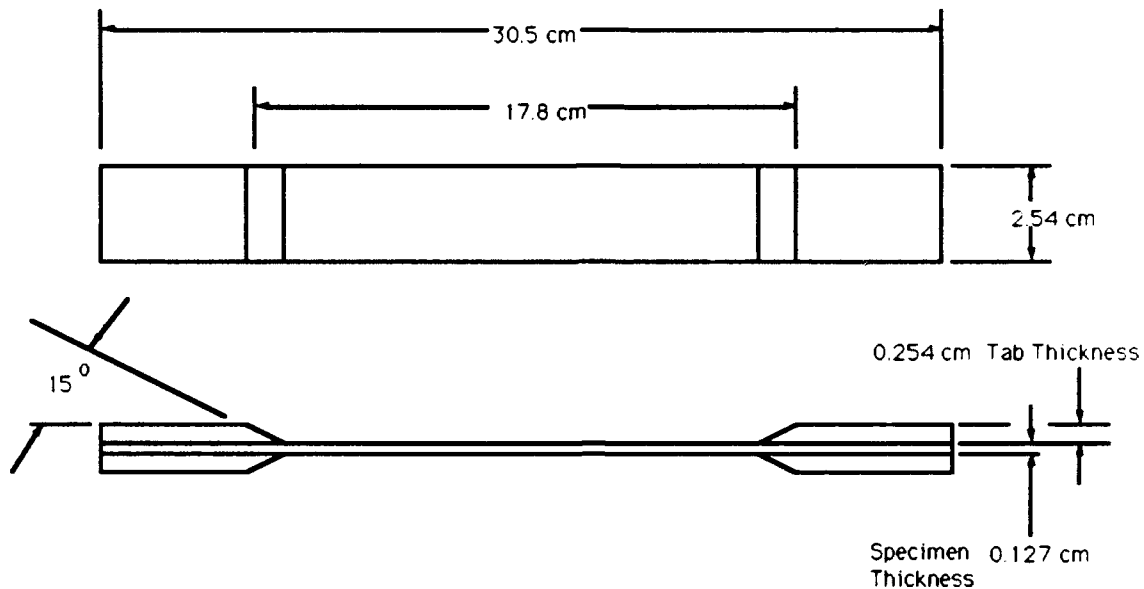


Figure 3.4 A sketch of tension specimens (ASTM D3095)

All specimens were strain gaged using standard techniques. The gages used were an overlay bi-axial gage, Micro-Measurements CEA-13-062WT-350. The gages were bonded to the specimens with BLH Permabond 910 adhesive.

No ASTM standard specimen configuration exists for compression tests of a thick laminate composites. Also thickness of specimen material in the  $\langle 001 \rangle$  direction was limited to a maximum dimension of 4.32 cm. Hence, the specimen chosen was the same as the one used by Fazle et al. [3.5]. This specimen geometry has a square cross section of  $6.45 \text{ cm}^2$ , with a length of 3.81 cm. In addition a traditional right circular cylinder specimen was used. The cylindrical specimen has a diameter of 1.91 cm, with a length of 3.81 cm. Both specimen geometries retain thick composite dimensions. Sketches of these two specimen geometries are given Figure 3.5.

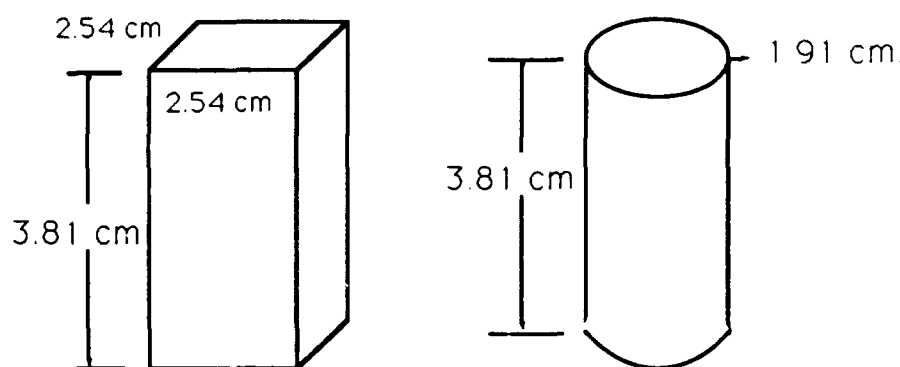


Figure 3.5. Specimen geometries for compression experiments.

Compressive strains were monitored by at least two bi-axial gages bonded on two orthogonal surfaces of GRP specimens. Specimen faces in contact with the loading plates were lubricated with Teflon to reduce frictional effects.

#### Compression Results

The goals of these compression experiments were two fold. The first goal was to determine if the stress - strain loci of GRP is sensitive to strain rate. The second goal was to extract from experimental data a mathematical form of these stress-strain loci which could easily be used to aid in computer simulations. In order to obtain these two goals, three problems had to be resolved; is the square cross - sectional specimen any better or worse then the cylindrical specimen; does specimen density and loading direction have any effect. Once these questions were resolved the effect of strain rate could be investigated and a curve fitted to the stress strain loci. The first experiments would resolve the specimen geometry, density variation and loading direction dilemma by using two groups of specimens one from the  $\langle 010 \rangle$  direction the other from the  $\langle 100 \rangle$  direction. The specimen groups chosen had both square cross - sectional and cylindrical specimens, within each group the specimen density was similar, for the  $\langle 010 \rangle$  group the average density was 1.964 (.005), and for the  $\langle 100 \rangle$  group the average density was 1.949 (.006). To minimize variables in experiments all tests were conducted at a strain rate of  $10^{-5} \text{ s}^{-1}$ . The average stress - strain loci with error bars for these experiments are in Figures 3.6 and 3.7.

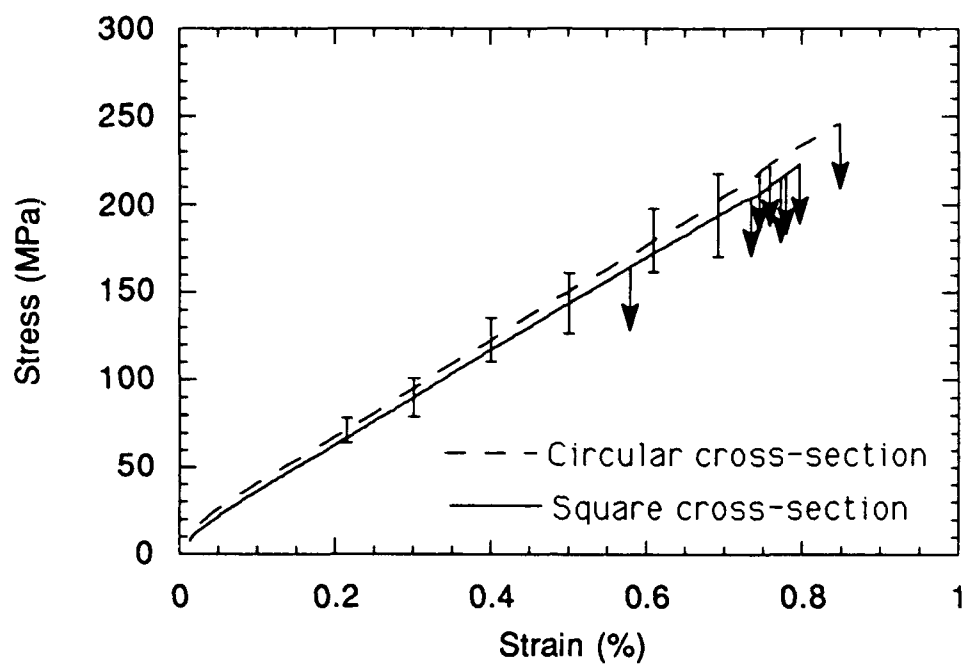


Figure 3.6 Comparison of <100> direction square and circular cross-section specimens. Arrows indicate failure stress for each specimen.

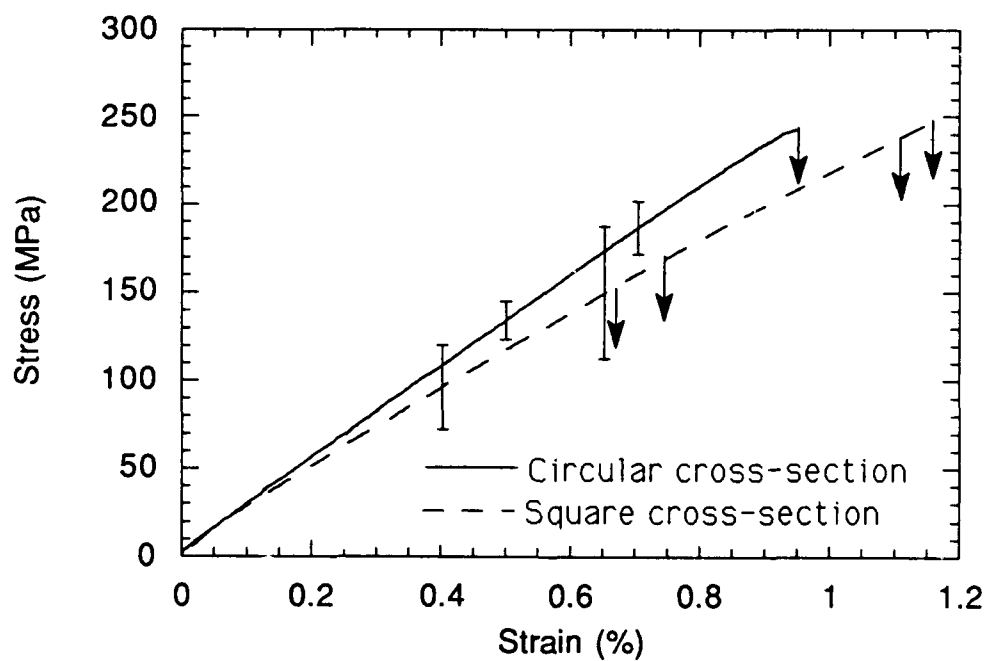


Figure 3.7 Comparison of <010> direction square and circular cross-section specimens. Arrows indicate failure stress for each specimen.



The scatter in these stress-strain loci varies from ~10-15 % even though stress and strain are measured with a precision of  $\pm 2$  %. The failure stresses were calculated from load measurements made with a calibrated load cell. For these two groups of specimens the scatter in failure stress was ~40%, indicating that the material variability was much greater than any inaccuracies imposed by load measurement. The average failure stress for the  $\langle 010 \rangle$  direction is  $212.9 \pm 23.2$  MPa, and  $210.3 \pm 46.2$  MPa for the  $\langle 100 \rangle$  direction. The strain measurements were made using strain gages on two orthogonal faces. For the  $\langle 010 \rangle$  and  $\langle 100 \rangle$  direction specimens one face was parallel to the ply lay-up direction, the other was perpendicular to it, see Figure 3.1. The face that was perpendicular to ply lay-up always had a 12% larger strain reading. The  $\langle 010 \rangle$  direction specimen strains were measured in the  $\langle 001 \rangle$  and  $\langle 100 \rangle$  planes. The average strains for  $\langle 001 \rangle$  and  $\langle 100 \rangle$  planes were  $.65 \pm .19$  % and  $.83 \pm .14$  % respectively. For the  $\langle 100 \rangle$  direction specimen strains were measured in the  $\langle 001 \rangle$  and  $\langle 010 \rangle$  planes. The average strains measured in the  $\langle 001 \rangle$  and  $\langle 010 \rangle$  planes were  $.76 \pm .18$  % and  $.89 \pm .04$  % respectively. With this high level of scatter in the stress - strain loci, failure stress and failure strain cannot be distinguished between the square cross-section specimens from the cylindrical specimens, nor the  $\langle 010 \rangle$  direction specimens from the  $\langle 100 \rangle$  direction specimens. Although density within each group was similar, inherent variations in the GRP panels caused specimens between the groups to have different densities,  $1.949 \pm .006$  Mg/m<sup>3</sup> for  $\langle 100 \rangle$  and  $1.964 \pm .005$  Mg/m<sup>3</sup> for  $\langle 010 \rangle$ . Since these two groups results are indistinguishable we concluded that density variations less than  $0.02$  Mg/m<sup>3</sup>, need not be considered in analysis of the data. It is assumed that the specimen geometry and density variations will not effect results in  $\langle 001 \rangle$  direction. Therefore all other experiments used the cylindrical specimen.

The effect of compressive loading a specimen in the  $\langle 001 \rangle$  direction was determined next. The cylindrical specimen was compressed at a constant strain rate of  $10^{-4}$ /sec. The average failure stress for  $\langle 001 \rangle$  direction was  $628 \pm 30.4$  MPa and this is an increase of almost 300 % compared to the average of  $210.3 \pm 46.2$  MPa for the  $\langle 100 \rangle$  direction. The average failure strain was  $7.57 \pm .61$  %, an increase of almost 7 times compared to  $\langle 010 \rangle$  and  $\langle 100 \rangle$  directions. The average modulus for  $\langle 001 \rangle$  was  $12.2 \pm .081$  MPa. The stress - strain loci was found to have a small non linearity, ie., a knee at ~150 MPa.

At this point the issue of specimen geometry, density variation, and the effect of loading direction for the  $\langle 100 \rangle$ ,  $\langle 010 \rangle$ , and  $\langle 001 \rangle$  directions have been addressed. The effort will focus on, strain rate sensitivity of GRP and mathematical representation of test data. To address the strain rate sensitivity, compressive loading of GRP specimens in the  $\langle 100 \rangle$ ,  $\langle 010 \rangle$  and  $\langle 001 \rangle$  directions was conducted at a strain rate of 1/sec. All measuring techniques were the same as for static experiments. The results of all compression experiments are given

in Table 3.6. The table lists density, strain rate, failure strain, failure stress, modulus and poisson's ratio for each specimen tested. Specimen geometry is indicated by specimen number; "-c-" for cylindrical and a "-s-" for square cross sectional specimens.

Table 3.6 Results of compression experiments on GRP composite specimens with square and circular cross-section with three different orientations.

Specimen Number	Density	Strain Rate	Failure Strain	Failure Strain	Failure Stress	Modulus	Modulus	Poisson's ratio	Poisson's ratio
	(Mg/m <sup>3</sup> )	(sec <sup>-1</sup> )	(%)	(%)	(MPa)	(GPa)	(GPa)		
			<001>	<100>		<001>	<100>	<001>	<100>
Y-c-10	1.964	5.3e-05	0.88	1.03	243.2	29.2	25.9	0.35	0.07
Y-c-12	1.970	1.18	0.73	0.86	296.5	24.5	19.2	0.34	0.18
Y-c-13	1.961	1.84	0.66	0.91	304.1	34.2	28.1	0.30	0.12
Y-s-1	1.958	2.7e-05	0.88	1.11	249.2	34.6	24.0		0.06
Y-s-4	1.963	2.7e-05	0.76	1.06	151.9	19.1	14.2	0.31	0.09
Y-s-5	1.970	2.8e-05	0.84	1.17	238.6	28.5	21.1	0.31	0.10
Y-s-14	1.967	2.3e-05	0.45	0.64	168.5	43.0	25.8		
			<001>	<010>		<001>	<010>	<001>	<010>
X-c-5	1.947	6.8e-05	0.84	0.93	245.1	26.3	25.4	0.35	0.11
X-c-7	1.943	4.3e-05	0.62	0.77	216.4	36.4	32.8	0.34	0.16
X-c-4	1.953	2.1e-05	0.81	0.89	221.7	27.2	27.3	0.33	0.11
X-c-6	1.948	1.69	0.95	1.04	293.6	29.2	29.6	0.33	0.20
X-c-10	1.951	1.67		0.99	324.1	31.1		0.36	
X-s-3	1.957	2.1e-05	0.53	0.78	204.2		26.4		0.23
X-s-8	1.952	2.8e-05	0.41	0.90	213.8	36.8	28.5	0.36	0.09
X-s-12	1.949	2.8e-05	0.73	0.83	215.7	30.2	26.1	0.30	0.14
X-s-14	1.941	3.1e-05	0.84	1.00	223.1	27.4	21.1	0.33	0.12
X-s-15	1.933	1.5e-05	0.38	0.54	163.4	47.5	24.6		
Z-c-2	1.931	1.8e-04	6.96		603.3	13.1		0.17	
Z-c-19	1.932	2.1e-04	7.59		618.7	11.6		0.23	
Z-c-21	1.931	1.9e-04	8.17		662.0	11.8		0.24	
Z-c-8	1.929	1.21	8.20		761.0	14.7		0.17	
Z-c-15	1.931	1.46	7.46		658.4	13.0			
Z-c-20	1.935	0.99	8.00		703.3	13.3		0.25	

For all three directions increasing the strain rate from 10<sup>-5</sup> s<sup>-1</sup> to 1 s<sup>-1</sup> caused a small increase in average failure stress. Because the scatter for the <100>, <010> and <001> directions is so large, and the number of experiments are limited, to consider this difference more than a trend would be poor judgment. There was also a small increase in the initial modulus for the <001> direction, which is typical of a polyester resin under dynamic

loading. The average stress-strain curves with failure locations are plotted in Figures 3.8 and 3.9 for all three directions.

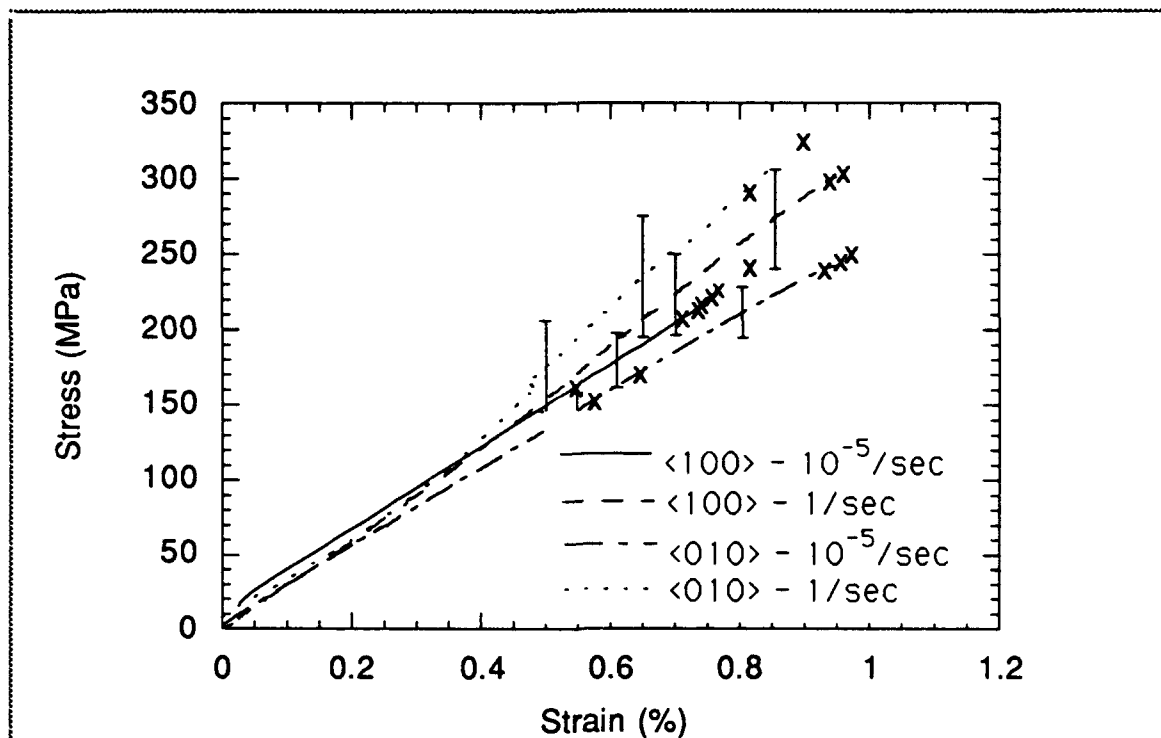


Figure 3.8 Orientation and strain rate effect for <100> and <010> directions.

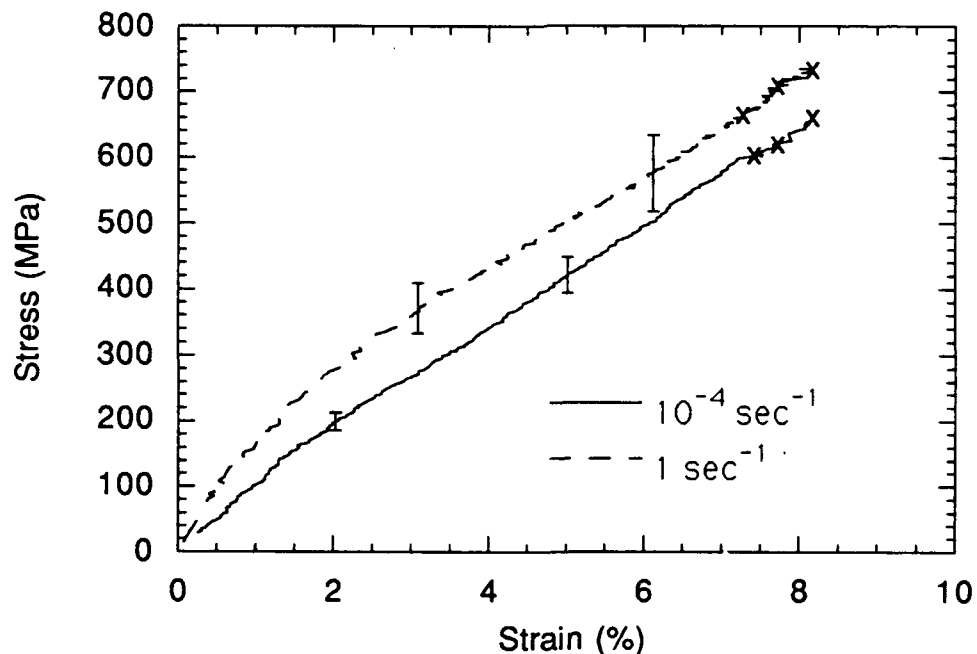


Figure 3.9 The <001> orientation strain rate effect.

The "x" symbols in these figures are the failure points for each specimen. With an increase in strain rate for the  $\langle 100 \rangle$  direction the average failure stress increased from  $210.3 \pm 46.2$  MPa to  $303.3 \pm 5.4$  MPa, and for the  $\langle 010 \rangle$  direction the increase was from  $212.9 \pm 23.2$  MPa to  $308.8 \pm 21.6$  MPa. For these two directions there appears to be a strain rate effect since the errors in failure do not overlap. For the  $\langle 001 \rangle$  direction the increase was from  $628 \pm 30.4$  MPa to  $707.6 \pm 51.4$  MPa, although the average values of failure stress are different there is an overlapping of their errors. This makes the increases in failure stress suspect, and more experiments need to be conducted to establish limits for data scatter. The failure strain and modulus for all directions were not effected by the increase in strain rate. For the  $\langle 100 \rangle$  and  $\langle 010 \rangle$  direction the average value of strain and modulus were  $0.81 \pm 20\%$  and  $28.3 \pm 6.7$  GPa respectively. For the  $\langle 001 \rangle$  the average values of failure strain and modulus were  $7.73 \pm .48\%$  and  $12.9 \pm 1.1$  GPa respectively. Table 3.7 list average values of density, strain rate, failure strain, failure stress, modulus, and poisson's ratio.

For applications, i.e., simulation, which do not find the small increases in failure stress obtained in the  $1 \text{ s}^{-1}$  experiments of interest the data has been placed into two groups the  $\langle 001 \rangle$  group and  $\langle 100 \rangle$  plus  $\langle 010 \rangle$  group. These two groups consist of data at both strain rates and both square cross-section and cylindrical specimens. Using the least squares fit, the  $\langle 100 \rangle$  plus  $\langle 010 \rangle$  data was fitted with a linear curve,

$$\sigma \text{ (MPa)} = 2.59 + 307 (\epsilon) (\%) \quad (3.30)$$

The average failure stress and failure strain was  $234 \pm 49$  MPa and  $0.81 \pm 0.20 \%$  respectively. The same treatment of data was applied to  $\langle 001 \rangle$  results to yield the linear relationship;

$$\sigma \text{ (MPa)} = 42.7 + 83 (\epsilon) (\%) \quad (3.31)$$

with average failure stress and strain of  $668 \pm 58$  MPa and  $7.73 \pm 0.48 \%$  respectively.

Table 3.7. Summary of results from compression experiments on GRP composite specimens at strain rates between  $10^{-5} \text{ s}^{-1}$  to  $1 \text{ s}^{-1}$ .

Specimen Orientation	Density (g/cm <sup>3</sup> )	Strain Rate (sec <sup>-1</sup> )	Failure Strain (%)	Failure Strain (%)	Failure Stress (MPa)	Moduli (GPa)	Moduli (GPa)	Poisson's Ratio	Poisson's Ratio
			<001>	<010>		<001>	<010>	<001>	<010>
<100>	1.947 ±0.008	3.19e-05 ±1.68e-05	0.76±0.18	0.89 ±0.04	210±46	30.9 ±8.8	22.2 ±4.9	0.34±.02	0.14±.05
<100>	1.950 ±0.002	1.68±0.14	0.70±0.05	1.0±0.21	300±5	29.4 ±6.9	23.7 ±6.3	0.35±.02	0.20
<010>	1.964 ±0.005	3.16e-05 ±1.2e-05	0.65±0.19	0.83 ±0.14	213±23	33.1 ±7.7	26.5 ±3.3	0.32±.02	0.08±.02
<010>	1.966 ±0.006	1.5±.47	0.95	1.02 ±0.04	309±22	30.1 ±1.3	29.6	0.32±.03	0.15±.04
<001>	1.931 ±0.006	1.9e-04	7.57±0.61		628±30	12.2 ±0.81		0.21±.04	
<001>	1.932 ±0.003	1.22±.235	7.89±0.38		708±51	13.7 ±0.91		0.21±.06	

#### Tension Results

Table 3.8 gives, failure stress, modulus and Poisson's ratio for GRP under tension. Due to premature failure of strain gages at approximately 138 MPa and 0.8 percent strain, and inability of LVDT to accurately measure small strains in specimen, no failure strains were recorded. It was assumed premature failure of strain gages was due to fiber failure under gages. There is a difference in failure stress between the <100> and <010> directions. The <100> failure stress is ~ 100 MPa less than the <010> direction. The failure stress increases for both <100> and <010> directions with increasing strain rate. For both <100> and <010> directions the average failure stress increased ~110 MPa.

Table 3.8. Results of tension experiments on GRP with two different orientations.

Specimen Number	Strain Rate (sec <sup>-1</sup> )	Failure Stress (MPa)	Modulus (GPa)	Poisson's Ratio
X-3P-1-14	1.0e-04	467.0	21.9	0.09
X-3P-1-17	1.0e-04	474.6	23.9	0.07
X-3P-1-10	1.0	611.4	22.7	0.23
X-3P-1-13	1.0	595.1	26.7	0.21
Y-3p-1-3	1.0e-04	564.1	19.5	-
Y-3p-1-5	1.0e-04	569.5	20.9	-
Y-3p-1-2	1.0	635.8	20.5	-
Y-3p-1-4	1.0	703.0	14.5	0.14

**(d). High Strain Rate Compression in The Thickness Direction:**

This section deals with the high strain rate experimental program. There were five high strain rate experiments conducted in the thickness or <001> orientation. The high strain rate compression tests were conducted using a Split Hopkinson Pressure Bar (SHPB). The bar consists of a striker, gun barrel, gas reservoir, input bar and output bar. A specimen is placed between the input and output bars. Nitrogen gas is compressed to a pressure required to obtain the desired striker velocity. Upon release, the gas expands down the gun barrel propelling the striker. The striker impacts the input bar causing a stress pulse to propagate through the bar. When the pulse reaches the specimen, some of it is reflected and some of it is transmitted due to the impedance mismatch between the specimen and the bars. These pulses are recorded by strain gages placed on the bars and transferred to computer for analysis. The stress and strain are obtained from the recorded pulses by the following relations

$$\sigma = E_b \frac{A_b}{A_s} \epsilon_t(t) \quad (3.32)$$

$$\dot{\epsilon} = \frac{-2C_l}{L} \epsilon_r(t) \quad (3.33)$$

where

$\sigma$  = stress

$\dot{\epsilon}$  = strain rate

$E_b$  = Young's modulus of bar

$C_l$  = longitudinal sound velocity of bar

$A_b$  = Cross sectional area of bar

$L$  = specimen length

$A_s$  = Cross sectional area

$\epsilon_r$  = reflected pulse as function of time

$\epsilon_t$  = transmitted pulse as a function of time

Strain is obtained by integrating the strain rate vs time trace (Eq.3.33). This data is then converted to true stress and true strain.

As described in the earlier section, the medium rate tests show that only the through thickness direction, shows same observable strain rate dependence, or in-elasticity in compression. Therefore, this was the only direction deemed worthwhile for conducting Split Hopkinson Pressure Bar experiments. Five experiments were conducted. In these experiments two pulse widths were used to strain the specimen either to failure or below failure as indicated in Table 3.9. Two tests were replicated to insure repeatability. The specimens were right circular discs. Of the five specimens four were 0.6 cm in diameter and 0.3 cm thick. The remaining one was 1.5 cm in diameter and 0.75 cm thick. The choice of these two geometries was to investigate the effect of scale.

Table 3.9 Conditions of Split Hopkinson Pressure Bar experiments in <001> direction of GRP composite.

Specimen	Pulse width	Diameter
Zs-1	80 $\mu$ sec	1.5 cm
Z207	80 $\mu$ sec	0.6 cm
Z208	80 $\mu$ sec	0.6 cm
Z211	40 $\mu$ sec	0.6 cm
Z212	40 $\mu$ sec	0.6 cm

## Results

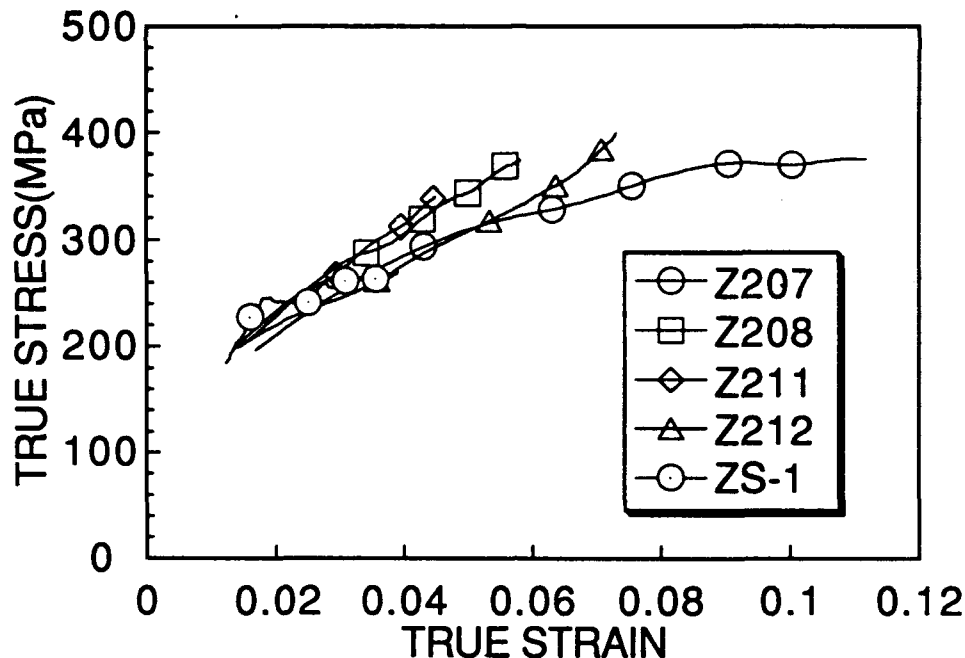


Figure 3.10 Stress - Strain for GRP Composite in the  $\langle 001 \rangle$  direction.

The results of the five experiments performed on GRP composite in the  $\langle 001 \rangle$  directions are shown in Figure 3.10. Only the non-linear portion of the curve is shown. As seen from the figure, no effect of scale is seen for the two geometries tested. Determination of failure is made by examining the transmitted and reflected pulses. Upon failure, due to the free surface created in the specimen, the pulses drop sharply to zero. This occurred only in the case of specimen Z2-7. From this specimen, failure stress and strain were calculated to be 374 MPa and 0.11, respectively.

**(e) . Summary:**

The results of experiments performed on GRP show that:

- (i) It deforms like a transversely isotropic composite.
- (ii) Directional sensitivity

Stress - strain loci under compression in the transversely isotropic plane i.e., in  $\langle 100 \rangle$  and in  $\langle 001 \rangle$  directions up to the respective failure strains in these directions are given by equations 3.30 and 3.31



$$\sigma = 2.59 + 307 \epsilon; \quad \epsilon < 0.85, \text{ for } \langle 100 \rangle \quad (3.30)$$

$$\sigma = 42.7 + 83 \epsilon; \quad \epsilon < 7.73, \text{ for } \langle 001 \rangle \quad (3.31)$$

where  $\sigma$  is in MPa and  $\epsilon$  is percent strain.

(iii) Strain rate sensitivity

The estimated value of failure stress under compression in the  $\langle 001 \rangle$  direction at 4000 per second is only 374 MPa compared to 628 and 708 MPa at the strain rates of  $10^{-4}$  and 1 per second, respectively.

Values of failure stresses under tension in both  $\langle 100 \rangle$  and  $\langle 010 \rangle$  directions are  $519 \pm 55$  at strain rate of  $10^{-4} \text{ s}^{-1}$  and  $636 \pm 47$  MPa at strain rate of  $1 \text{ s}^{-1}$ , respectively.

(iv) Finally, since GRP does not appear to deform inelastically up to its failure, the complete set of elastic constants data can be used to calculate strain developed in GRP in any arbitrary direction under compressive and tensile loading.

**(f) .Future Work:**

The future work on GRP will be done to determine and to elucidate its shock wave response in the  $\langle 001 \rangle$  direction and to understand the mechanics of delamination under impact loading. The above two facets of deformation of GRP under shock wave loading will be investigated by conducting controlled one dimensional shock wave experiments in which GRP will undergo either a complete compressive and release stress cycle or a complete compressive and release stress cycle followed by another cycle of tensile wave loading and unloading. Care will be taken to recover GRP from these types of shock wave experiments to determine the microstructural changes brought about in the GRP specimens due to the above mentioned stress histories. The idea behind conducting these experiments is to investigate the conditions required to initiate the process of delamination in GRP. It is expected that the results of these experiments will improve our current understanding of delamination process in a transversely isotropic fiber reinforced composite. A few additional two dimensional impact experiments will be carried out delineate the role of confinement on the delamination of this composite.

**REFERENCES**

[3.1] Martin, A. G. 1976. Phase Velocity Measurements in Dispersive Materials by Narrow Band Burst Phase Comparison. Army Materials and Mechanics Research Center, Watertown, MA: AMMRC TR 76-22.

- [3.2] Papadakis, E. P. ,Jr. 1967. J. Acoust. Soc. Amer. 42: 1045.
- [3.3] Love, A. E. H. 1944. A Treaties on the Mathematical Theory of Elasticity. New York, NY: Dover Publications.
- [3.4] Green, J.L, Emsli, J.F,.and Chou, S.C.,The Application of Laser Speckle Interferometry to Measure Strain at Elevated Temperatures and Various Loading Rates, MTL TR 90-23, May 1990
- [3.5] Fazle J., Goeke E.,and Nunes J, Characterization of Thick Glass Rienforced Composites, MTL TR 92-43
- [3.6] Robertson, K.D., Chou, S.C., and Rainey,J.H.,Design and Operating Characteristics of a Split Hopkinson Pressure Bar Apparatus, AMMRC TR 71-49, November 1971

#### **4. STRESS WAVE EXPERIMENT AND ANALYSIS UNDER BALLISTIC CONDITIONS**

##### **(a) Background:**

The shock response of GRP materials is complex in nature. Research efforts to evaluate and determine the stress-strain response in GRP under shock and penetration loading conditions have been minimal.

Unlike in metals, the shock stress amplitude in GRP rapidly attenuates and the wave disperses. Since the amplitude and loading duration greatly influence damage initiation and propagation, it is essential to experimentally measure these quantities and develop an analytical model. For this purpose, we considered an impact test in which a thick GRP target with embedded piezo-resistive (manganin) stress gauges was impacted by a steel projectile of 20 mm diameter and about 7.5 mm length.

One of the difficulties in predicting dynamic behavior of a GRP composite is that the material delaminates during ballistic penetration. Interpretation of the measured stress response will be difficult when several types of damage mechanisms operate inside the target, simultaneously. Therefore, in order to develop a stress wave propagation model, one must establish a threshold stress condition for damage initiation by eliminating 1) fiber-cutting in the target due to projectile penetration, and 2) target delamination.

For this purpose, a threshold level impact velocity of about 350 m/s was experimentally established. When the GRP was impacted at velocities below this threshold level, the stress gauge response was assumed to be entirely due to the shock wave propagation. This assumption was further confirmed by the posttest observations of the impacted panels in which the fiber cutting and delamination were absent.

##### **(b) Test Method:**

The projectile chosen was a modified 20mm FSP (Fragment Simulating Projectile) with a flat face and somewhat rounded back surface as shown in Figure 4.1. The mass was approximately 250 grains (16.2 grams). The projectile was launched by conventional powder gun techniques out of a 20mm gun tube with a 1 in 20 twist.

The basic target configuration consisted of three (front, middle, and rear) GRP laminates with thicknesses, 9.53mm, 9.53 mm, and 25.4 mm respectively. The laminates were roughly 0.3 x 0.3 meter wide. A relatively thicker rear plate was chosen to assure that the release waves from the stress-free rear surface of this plate would not interfere with the stress measurements.

The target configuration is schematically shown in Figure 4.2. Two manganin stress gauges, one on the top surface of the middle plate (plate 2), and another on the top surface of the bottom plate (plate 3) were respectively bonded using Perma-Bond 910 with a catalyst supplied by BLH electronics.

The three plates were then carefully assembled with the impact point aligned along the axis of the stress gauge. The plates were bonded together using Epoxy Patch Kit (0151 clear) supplied by Dexter corporation.

#### **(c) Instrumentation and Data Acquisition**

A two channel pulsed power supply and a digitizing 10 mhz, 12 bit oscilloscope were employed for data acquisition. The pulsed power supply and the Wheatstone bridge combination are shown in Figure 4.3. The power supply has two independent channels so that two gages can be installed each with separate 50 volt excitation sources. Upon triggering, a silicon controlled rectifier (SCR) is activated allowing a 50 volt charging capacitor to be dumped across the bridge powering the manganin gages. Dynasen manganin gages have an element size of 6.35mm x 6.35mm, a lead length of 158.75mm, and a nominal resistance of 47 ohms.

Two "make screen" circuits are used to trigger the data acquisition equipment and to record the time-zero of the impact. The make screen is a 100 mm x 100 mm conductive circuit printed on a 0.05 mm thick mylar sheet. The projectile's contact with the screen completes the circuit which produces a 7 volt square-wave output. The first make screen is placed approximately 75 mm in front of the target to simultaneously trigger both channels of the power supply and the oscilloscope.

The power supplies were triggered in this manner to allow any initial transients and instability in the power supply to subside during the first few microseconds after activation. The second make screen is placed in front of the target to record the impact time-zero to which all subsequent shock pressure signals are measured.

The gages are initially balanced under a no-load condition by repeatedly exciting the bridge and adjusting a balancing potentiometer until a voltage output of zero is achieved. Once the bridge is balanced, the gage is calibrated by a series of resistors of pre-determined values that are used to shunt the bridge to simulate a loaded condition. When the gage is stressed due to shock loading, the resistance change in the gage leads to voltage change with respect to time and this corresponding voltage history is recorded by the oscilloscope. Using calibration factors provided by Dynasen, the voltage data is then converted into stress measurement data.

#### **(d) Test Results**

The accurate impacting of the FSP type projectile at the center of the front plate was accomplished by performing a series of trial and error tests on available E2 glass/polyester panels. However, in the subsequent test series, the S-2 glass/polyester GRP laminates were used. The test details are summarized in Table 4.1.

The surface of the GRP laminates was found to be very rough and uneven. The initial attempt was to keep the bondline between the laminates to be very thin (less than 500 microns). However, when the laminates were bonded together with the gauge package, the interface (glue) layers were seen to be relatively thick (about 1 mm).

The measured stress histories for the two successful tests (see Table 4.1) are shown in Figure 4.4. Since the velocity in test #T41-93-4 was lower by 40 m/s than in test #T41-93-2, the stress amplitude of front gauge was also lower. However, the rear gauge in the lower velocity test registered higher amplitude. The slope of the elastic waves in the front gauge response compared very well between these two tests; however, the rear gauges showed different slopes. Since the impact location in test #T41-93-2 was not exactly at the center, this offset could introduce a significant difference between these two tests. Additional tests with minimum offsets are needed to establish repeatability of the tests as well as the scatter due to material variability.

**Table 4.1: Tests on GRP with S-2 reinforcement**

Test #	Target ID	Target Component Thickness (mm)			Impact Velocity (m/s)	Hit Location (mm)		Comments
		Plate 1	Plate 2	Plate 3		X	Y	
T41-93-1	38381-2-1	9.91	9.93	25.4	411.4	5	12	Projectile hit above gages. No stress wave was detected
T41-93-2	38381-2-2	9.98	10.01	25.4	285.6	4	2	Successful gauge measurements
T41-93-3	38381-2-3	10.16	10.10	25.4	331.9	4	4	First gauge broke during impact
T41-93-4	38381-2-4	9.88	9.42	25.4	246.0	1.5	-1	Successful gauge measurements with a small offset

#### **(e) Preliminary Analysis**

The primary objective of the computational analysis is to determine the critical need for appropriate EOS (Hugoniot) data. The secondary objective is to interpret and analyze the manganin stress gauge data. The 91 version EPIC code [4.1] was employed to accomplish these objectives.

There are two essential requirements in the EPIC-code modeling of GRP laminates under shock and penetration loading conditions. The first requirement is the availability and development of the equation of state (EOS). The EOS describes the thermodynamically based pressure-volume relationship. The second requirement is the constitutive relationship which describes the flow stress variation with respect to strain, strain rate, temperature, and pressure. Therefore, availability of EOS and constitutive models are essential in any realistic and accurate analysis using advanced finite element computer codes. Since the EOS and constitutive models are not readily available for the S2 glass/polyester GRP material system, models that are applicable to metals were used to explore the characteristics of GRP under shock loading.

The EPIC code was employed in the preliminary analysis of the ballistic experiment. The GRP was modeled using simplistic EOS and material descriptions. The GRP was described as an isotropic material using the through-thickness properties reported in Section 3 of this report. These properties are shown in Table 4.2. The EOS was described simply by a linear relationship ( $P = Ke_v$ ) between pressure ( $P$ ) and volumetric strain ( $e_v$ );  $K$  is the bulk modulus.

**Table 4.2. Properties of GRP used in the Simulation**

Density (g/cm <sup>3</sup> ) (from Table 3.1)	Young's Modulus (GPa) (from Table 3.12)	Poisson's Ratio (from Table 3.12)	Average Flow Strength (GPa) (using the quasi- static tests data from Table 3.11)
1.949	12.2	0.2	0.667

Test T41-93-4 was simulated using the 91 version of the EPIC code. The target and projectile were discretized by a finite element mesh with a total of 2345 nodes and 4520 cross-triangle elements [4.1] as shown in Figure 4.5. The steel projectile was modeled as a circular disk with 7.5 mm length and 10 mm radius. The GRP target was assumed to be a plate of 100 mm radius and a total thickness of 44 mm. This radius is sufficiently large enough to delay the arrival of release waves from the lateral boundaries. Thus, similar boundary and loading conditions on the target were employed between the computational modeling and the experiment.

The calculated stress histories at the top and bottom gauge locations are compared with the experimental data in Figure 4.6. The stress levels in the experiments were significantly higher than the calculated levels. The pulse durations between the simulation and the experimental measurements for the two gauges matched well. However, the stress rise time in the test was much larger compared to the simulation. Since we employed a simplistic EOS and strength model, the dispersion of the wave is not realistically modeled in the code. Therefore, it is not too surprising to see smaller rise time in the EPIC simulation.

Since the shock impedance was calculated using the through-thickness elastic properties and material density of the GRP, the calculated stress amplitudes are expected to be higher than the gauge measurements. However, the simulated stress amplitudes were much lower than the measured amplitudes as shown in Figure 4.6. A critical examination of the experimental technique and the code analysis suggested the following areas for future investigation.

1. The gauge package between the two GRP laminates was too thick (1 mm). There is a strong possibility that the gauge responded to the plastic straining in the surrounding bond layer.

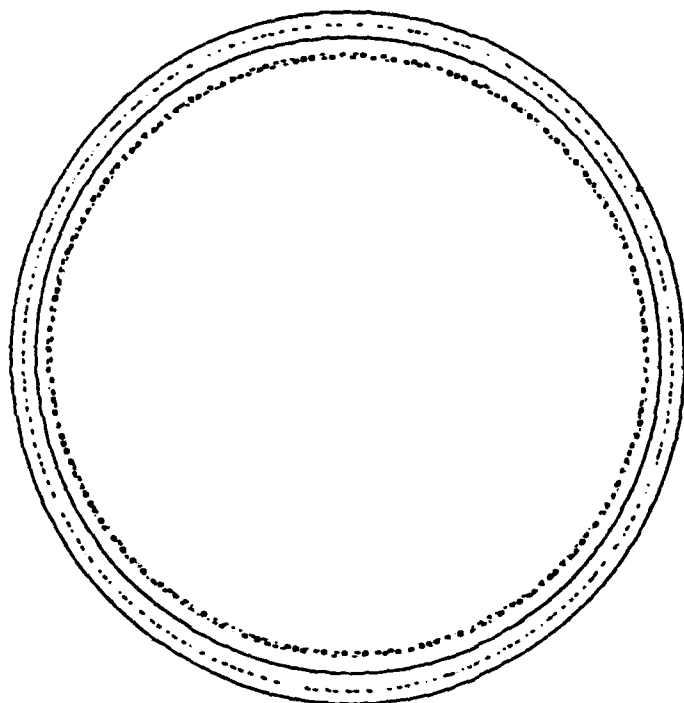
2. The stress gauge calibration had taken into account only the resistance change due to the stress applied normal to the gauge surface. This is always true under a planar impact where the lateral strains are relatively low and the pressure across the gauge surface is uniform.

3. Since the bond layer surrounding the gauge deforms significantly, this deformation introduces stretching of the gauge. Therefore, the recorded voltage includes the effects of both stress and strain. To accurately measure the stress, the strain contribution should be subtracted out from the measured voltage record.

4. In the EPIC simulation, the bond layer was not modeled. Therefore, the rise time in the modeling will be shorter than the rise time in the test. Additional simulation with the modeling of the bond layer is needed to evaluate the effect of this layer on the rise time.

5. Hugoniot data must be obtained from the plate impact experiments for a realistic EOS description for the GRP. The code analysis with an improved EOS will provide meaningful values for the shock amplitude.

**Reference:** [4.1] Johnson, G. R. and Stryk, R. A., "User Instructions for the 1991 Version of the EPIC Research Code," WL/MN-TR-91-53, Eglin Air Force Base, FL, (1991).



Modified FSP Projectile

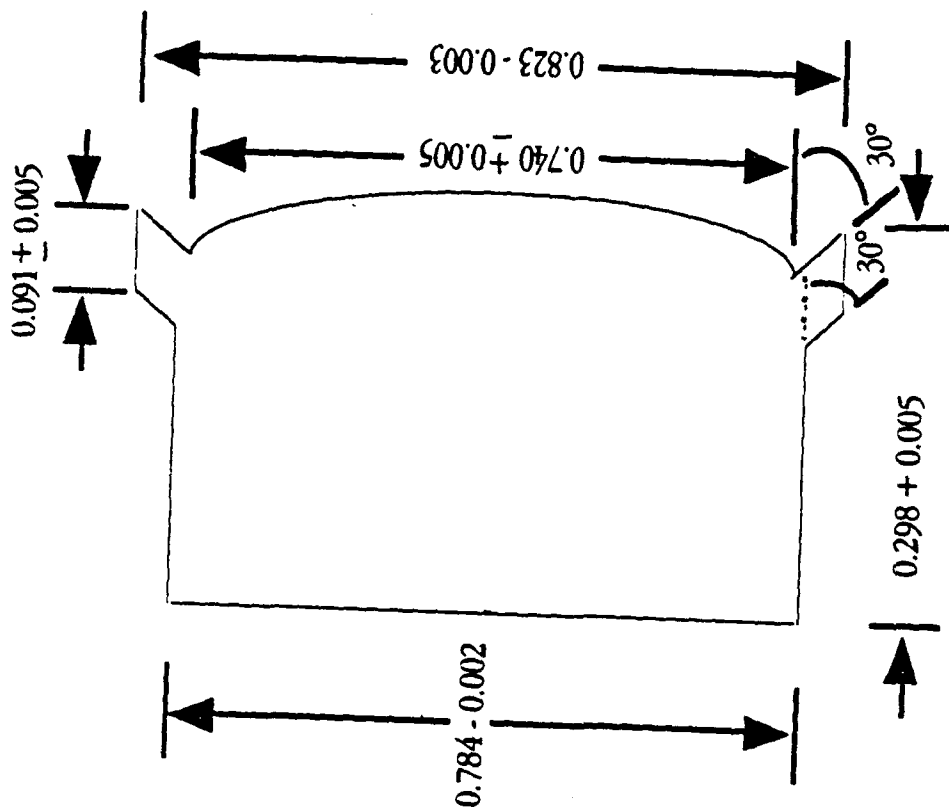


Figure 4.1 Modified FSP projectile.



Manganin Guages

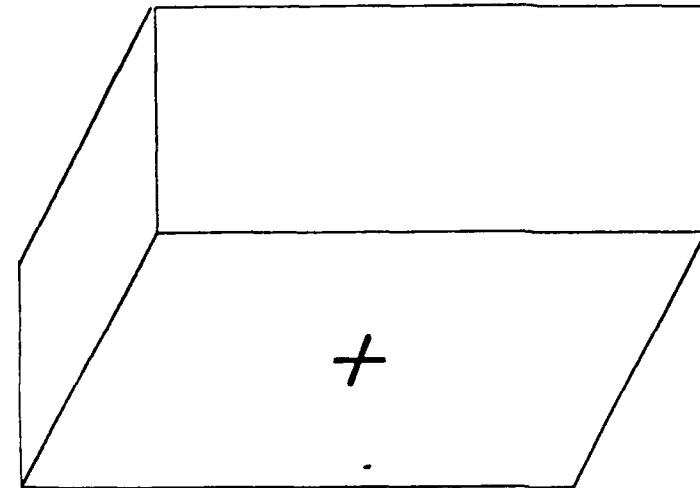
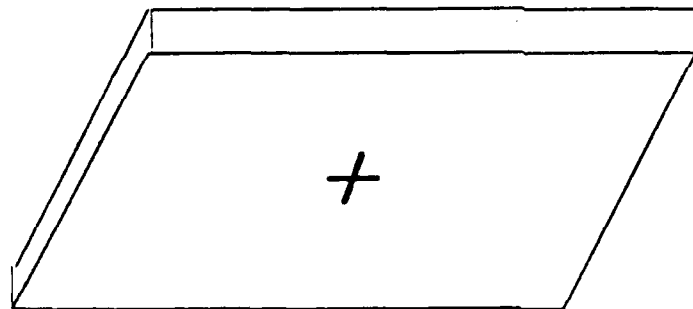
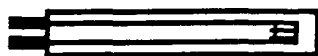


PLATE 1

PLATE 2

PLATE 3

Figure 4.2 Target Configuration

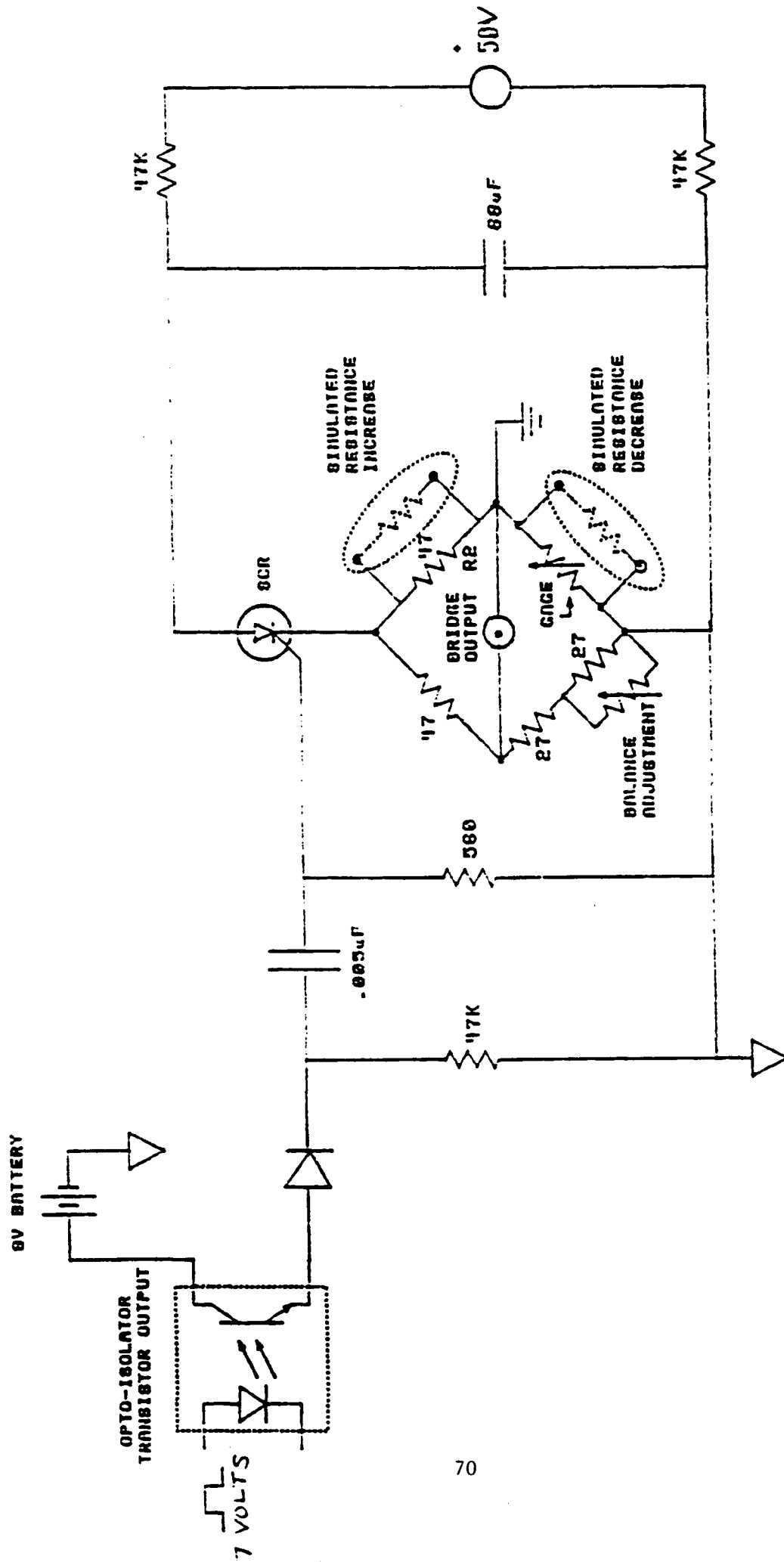


Figure 4.3 Pulsed power supply.

## Stress Measurements in GRP Ballistic Tests

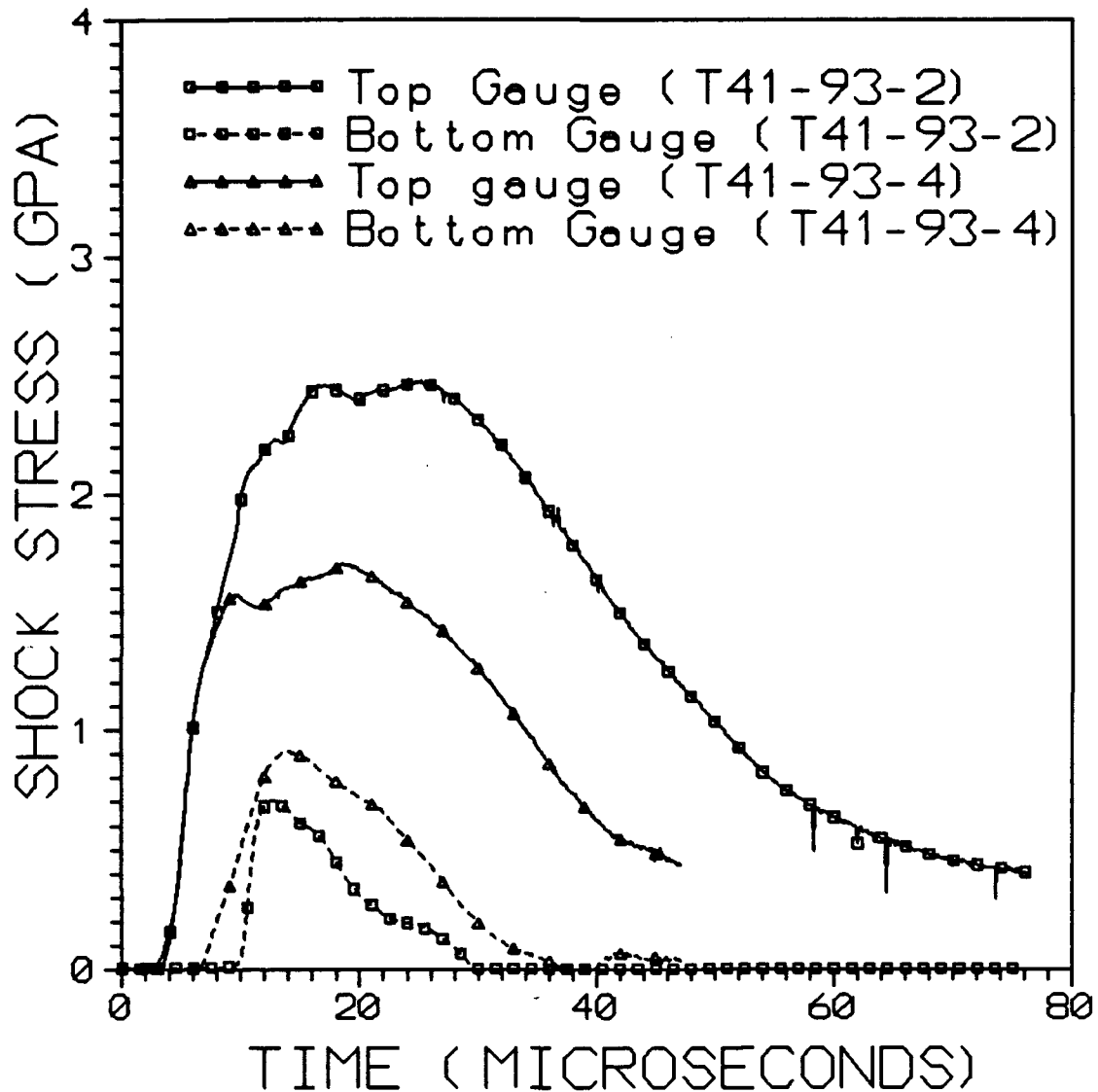


Figure 4.4. Measured stress histories at the gauge locations in tests# T41-93-2 and #T41-93-4.

EPIC POST PROCESSOR, POST1 (1992-2) 15:19:01 12-Oct-93  
2-D AXISYMMETRIC GEOMETRY WITHOUT SPIN

TRIAL , CASE = 1, TIME = .00000000, CYCLE = 0

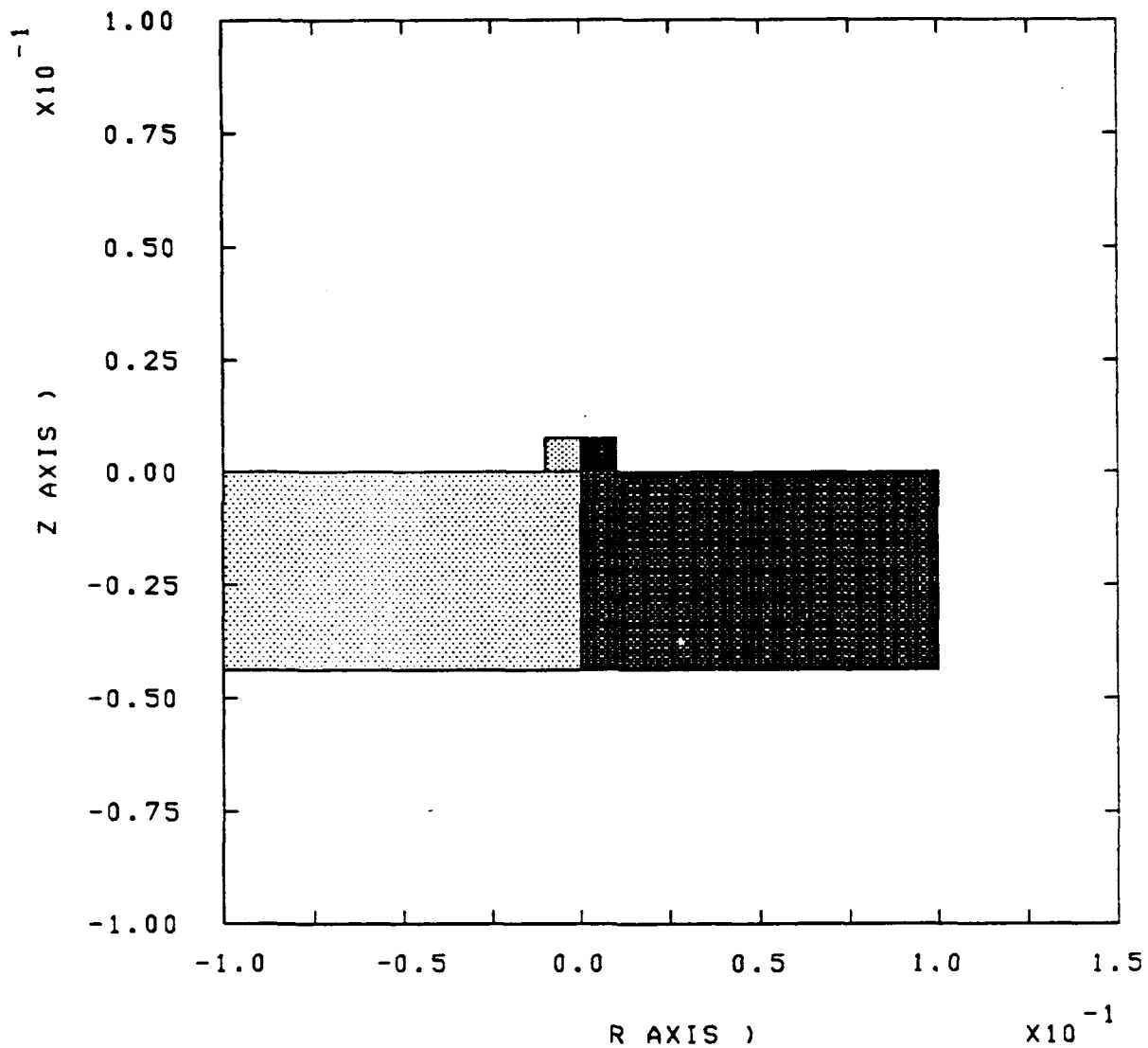


Figure 4.5 Finite element mesh for the projectile-target configuration.

## Comparison of Code Simulation with Data

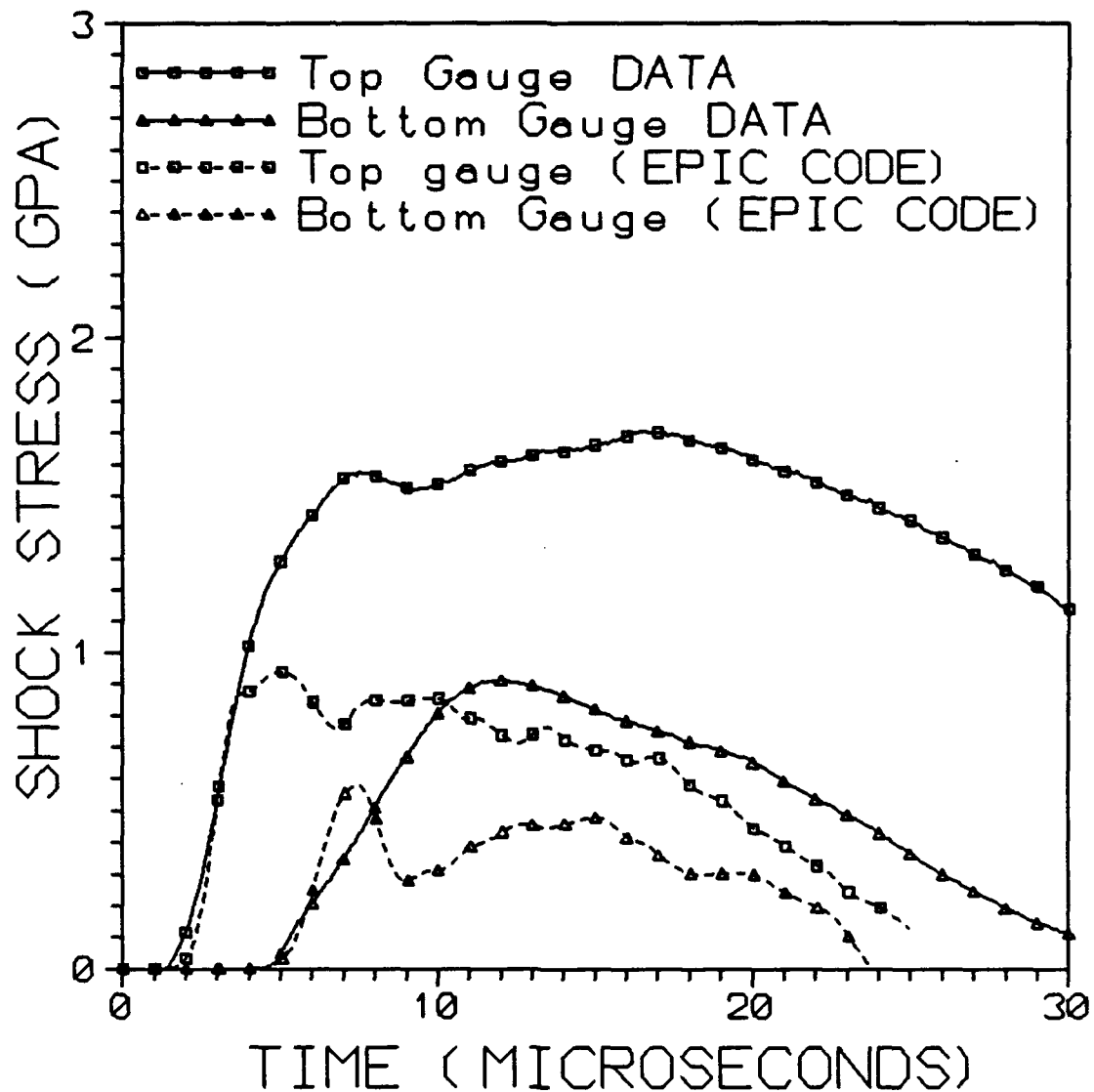


Figure 4.6. Comparison between stress gauge data (#T41-93-4) and EPIC computed stress histories using a simplistic metal-based description for the GRP.

## **5. Summary of Results and Future Work**

### **a. Summary of Results**

The objective of this effort is to develop a predictive methodology for dynamic response of S-2 glass-reinforced plastic (GRP) laminate subjected to impact loading. The technical approach is a combination of experiments and analysis. The effort was divided into three parts:

Ballistic Impact Damage  
Dynamic Characterization  
Stress Wave Experiment and Analysis.

The efforts in ballistic response of GRP provide results of a global manner which could be used for engineering purposes and, more important, as a guideline for developing predictive methodology and eventually as a bench mark or data base to validate predictive capability. The results from dynamic characterization of GRP are necessary for formulating a material model which is an essential ingredient for numerical simulation of material or structural response under impact loading. The other important parameters and information required in developing predictive capability are effects of heterogeneity of the GRP on transient response and those of the multi-dimensional and free boundaries on the stress states in GRP.

The progress of each part is detailed in Chapters (2), (3) and (4) respectively. The findings are collected and summarized here.

#### **(I) Ballistic Impact Damage Evaluation**

Computed tomography inspection of glass-reinforced plastic panels has been shown to provide detailed, quantitative data on internal delamination resulting from fragment ballistic impact.

Corollary results to the fragment impact experiments include data on fragment depth of penetration in S-2 glass-reinforced plastic laminate and maximum transient displacement of GRP laminate rear surface during fragment impact. These results were obtained to assist development of dynamic behavior simulation models for the GRP laminate material.

Compression testing of both undamaged and ballistically damaged S-2 glass-reinforced plastic panels shows that test results are reproducible for replicate experiments and that compressive strength of single-thickness panels after fragment impact can be related to fragment mass and strike velocity.

A correlation of compressive strength of S-2 glass-reinforced plastic panels after ballistic impact with panel average delamination has been found. The correlation shows an immediate drop in compressive strength to approximately 50% of the undamaged value for as little as 5% average delamination volume. However, compressive strength falls off slowly as average delamination increases above five percent. Future work will further test this correlation.

A preview experiment consisting of a fragment impact on a titanium-faced glass-reinforced plastic panel shows that glass-reinforced plastic laminates can suffer extensive delamination and loss of strength without direct impact by a kinetic energy threat. Induced ballistic damage to glass-reinforced laminates behind applique armor will be a major topic for follow-on work.

## **(II) Dynamic Characterization**

The GRP investigated behaves like a transversely isotropic medium with the transversely isotropic plane coinciding with the plane of weave.

A set of six elastic constants required for describing the material behavior in the small strain region has been determined.

The GRP does not appear to deform in-elastically up to its failure; therefore, failure stresses in three directions and the six elastic constants provide a complete set of material parameters required for numerical simulation under a quasi-static loading condition. The dynamic and shock response (determination of equation-of-state) will be a major effort for follow-on work.

The preliminary results indicate that the material possesses a relatively mild strain-rate sensitivity. Further investigation in the future will clarify this issue.

## **(III) Stress Wave Experiments and Analysis**

Experiments of a blunt projectile impacting a GRP plate were conducted. The stress-time history at two locations in the plate along the impact trajectory was recorded. The impact velocity was kept below the threshold of initiating any damage in the GRP plate.

The EPIC code, a hydrodynamic computer program, was employed to perform numerical simulations of the experimental configuration. Due to the lack of precise equation-of-state (EOS) for GRP, a simple linear relationship between pressure and volumetric strain was used in this preliminary attempt.

Results indicate that the trend of stress-time history at the two locations was reproduced; however, the details of stress wave forms were not simulated. This is attributed to the lack of EOS and the effect of anisotropy of the material. These two issues will be explored in follow-on work.

## **b. Future Work**

In the area of ballistic impact damage evaluation the work planned for FY94 will critically test the hypothesis that average percent delamination of a GRP laminate panel determines compressive strength after ballistic impact. Fragment ballistic experiments of Chapter 2 will be repeated for panels of different size and thickness than tested in this work. Specifically, panels of dimensions 30"x30"x1.75" (approximately two times the area of panels tested in Chapter 2) will be subjected to fragment impact as in Chapter 2; panels of dimensions 20"x20"x1" will be tested with fragments of two sizes at strike velocities below the panel limit velocity. The former set of experiments examines the effect of panel size on the results of Chapter 2; the latter examines the effect of panel thickness.

A set of experiments will be conducted to examine damage experienced by a GRP laminate that is the backup component in an applique-type armor. Chapter 2 reported results of a preview experiment on this topic which is necessarily made complicated by the number of possible applique and threat types. For this program, binary armor consisting of a 1"-thick frontal plate of 5083 aluminum alloy backed with a 1-3/4"-thick GRP laminate will be tested with the 830 grain fragment at strike velocities that range up to the limit velocity of the binary; also a ceramic composite armor made up of an array of aluminum oxide tiles backed with a 7/8"-thick GRP laminate will be tested with a 1/2 scale model 30 mm tungsten penetrator at velocities corresponding to service velocity and 500 meters ranges for a 30 mm cannon.

Finally, the question of GRP laminates panel damage resulting from multiple impacts will be addressed by testing panels of dimension 20"x40"x1-3/4" with single and double fragment impacts. The double impacts will be selected to provide both mutually exclusive (disjoint) damage zones and overlapping damage zones to examine the extent to which superposition of damage can be used to determine compressive strength after (multiple) ballistic impact.

Computed tomography inspection will be used to locate and quantify panel internal delamination; compression testing will be used to measure residual strength of GRP laminates after ballistic test. Completion of this work should provide design guidelines on resultant damage and residual compressive strength of thick GRP laminates after ballistic attack.

The future work on dynamic characterization of GRP will be done to determine and to elucidate its shock wave response in the through thickness direction and to understand the mechanics of delamination under impact loading. The above two facets of deformation of GRP under shock wave loading will be investigated by conducting controlled one dimensional shock wave experiments in which GRP will undergo either a complete compressive and release stress cycle or a complete compressive and release stress cycle followed by another cycle of tensile wave loading and unloading.



Care will be taken to recover GRP from these types of shock wave experiments to determine the micro-structural changes brought about in the GRP specimens due to the above mentioned stress histories. The idea behind conducting these experiments is to investigate the conditions required to initiate the process of delamination in GRP. It is expected that the results of these experiments will improve our current understanding of delamination process in a transversely isotropic fiber reinforced composite. A few additional two dimensional impact experiments will be carried out to delineate the role of confinement on the delamination of this composite.

A critical examination of the stress wave experiments and the EPIC code analysis suggests the following areas for future investigation.

The epoxy bond in the gauge package between the two GRP laminates was relatively thick; there is possibility that the bond layer deforms significantly. This deformation induces stretching in the gauge itself, the effect of which must be calibrated for a more accurate measurement of stress levels.

The reason for employing a relatively thick bond layer is to compensate for the roughness of the GRP surfaces. In the preliminary simulation, the bond layer was not modeled which may be one of the causes for the discrepancy between the experimental and calculated results. The effect of this additional bond layer on the stress calculation will be investigated.

Finally, a realistic EOS description for the GRP must be determined and implemented into the computer code for simulation.

## APPENDIX

Final Report

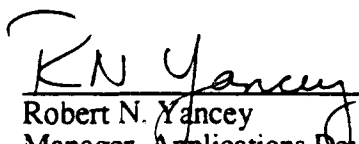
# COMPUTED TOMOGRAPHY INSPECTION OF IMPACTED FIBERGLASS PANELS

Under contract to:

US Army Research Laboratory  
AMSRL-MA-DA

Purchase Order DAAL01-93-M-S390  
ARACOR Project No. D004  
September 27, 1993

Prepared by:



Robert N. Yancey  
Manager, Applications Development Area  
Advanced Research and Applications Corporation

9/27/93  
Date

ADVANCED RESEARCH AND APPLICATIONS CORPORATION  
425 Lakeside Drive  
Sunnyvale, CA 94086

## CT INSPECTION REPORT

### I. ADMINISTRATIVE DATA

**Purpose:** This test report discusses the test methods and results of computed tomography (CT) inspection using the 9-MeV CT System installed at Hill Air Force Base, Utah.

**Background/Objectives:** This study was to investigate the feasibility of using computed tomography (CT) to detect the extent of damage in impacted fiberglass test panels. The purpose is to locate and define the damage zone in each of the shot panels as well as determine the depth of penetration of the projectile. Smaller panels were scanned previously on a 420-keV CT system (LAM/DE) and the results were encouraging. Larger panels were scanned for this study and the size of the panels required that the scans be carried out on a higher energy CT system. The Hill AFB 9-MeV system was chosen for this purpose.

**Test Dates:** 10-13 August 1993

### II. TEST ASSETS

**Description:** Twenty fiberglass panels, 24" x 24" were scanned. Nineteen of the panels were approximately 1.7" thick and one (T45-93-2) was 2.75" thick. All panels had been impacted except for one control panel (K).

**System Serial Number:** A-T

Each plate was given a letter identifier (A-T) and the corresponding filename contained the identifier and the slice number (i.e. A00012). Table 1 gives the letter identifier with the corresponding plate serial number.

TABLE 1. Letter identifiers with corresponding serial numbers

Letter ID	Plate ID	Letter ID	Plate ID
A	T45-93-1	K	Control
B	T44-93-2	L	T28-93-3
C	T44-93-3	M	T28-93-2
D	T44-93-6	N	T27-93-2
E	T7-93-2	O	T27-93-1
F	T44-93-1	P	T26-93-3
G	T45-93-2	Q	T27-93-3
H	T7-93-1	R	T28-93-1
I	T44-93-5	S	T26-93-2
J	T44-93-4	T	T26-93-1

### III. CONFIGURATION

**Mounting:** The panels were mounted flat on four wood mounting blocks. The configuration of the panel is shown in Figure 1 and on the data analysis printouts. The nylon rod to secure one of the wood blocks is always on the edge opposite the edge with the panel serial number. The nylon rod is visible in all of the CT slices. The panels were mounted with the impact side facing up and the scans began at the

bottom of the panel (opposite impact side) and worked their way up the panel. Scans were taken with a 2.0 mm effective slice thickness and the scans were spaced every 2.0 mm to provide full coverage of the panel.

**System Parameters:**

Magnification Factor	2.0
Source Voltage	9.0 MeV
Source Current	N/A

**Scan Parameters:**

Number of CT Scans	~32 per panel
Slice Thickness	2.0 mm (4.0 mm aperture setting)
Field of View	770 mm
Pixel Size	0.75 mm
Image Size	1024 x 1024
Integration Time	1 pulse per channel
Scan Duration	~ 1.5 minutes per slice

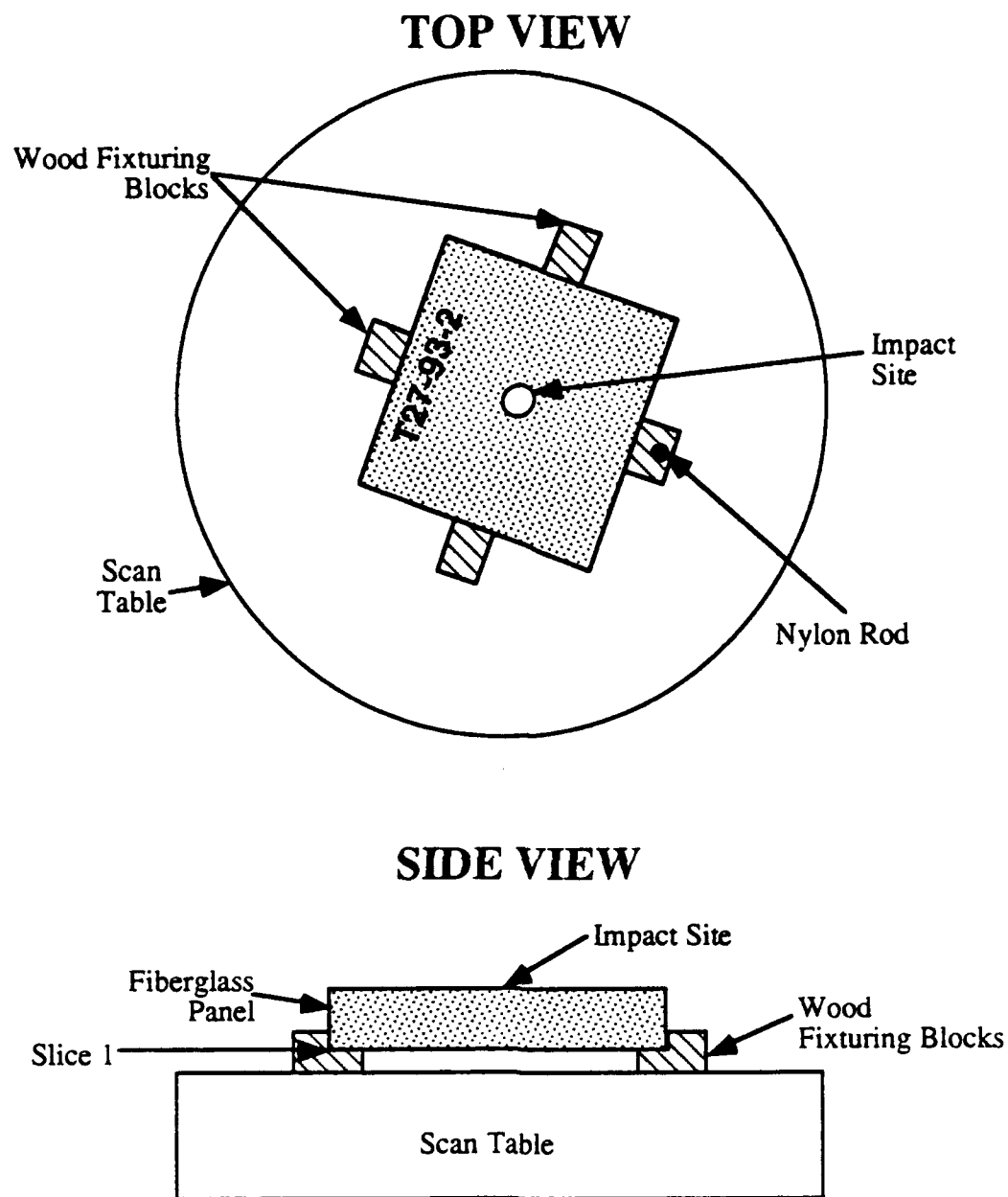


**FIGURE 1.** Mounting Configuration for Fiberglass Impact Panels

#### IV. ANALYSIS OF IMAGERY

A summary sheet is supplied for each panel scanned. The summary sheet includes important scan parameters including the field of view, resolution aperture setting, slice thickness aperture setting, scan height, integration time, and image matrix. The summary sheet also includes notes on certain slices such as location of the slug and the slices where photos were taken. The summary sheet also includes the percent damage calculations for all slices where the entire cross-section of the plate was imaged. A curve of the damage state vs. slice number is shown below. A trapezoidal rule calculation was used to determine the area under the curve which is noted as TOTAL DAMAGE at the bottom right. The summary sheet also includes an illustration of how the panel was positioned on the scan table.

The damage state was determined by applying a median filter to the images to better highlight the damage. An illustration of how the filtering enhanced the damage is shown in Figure 2. As shown, the filtering smoothes the image and eliminates the fiber weave pattern from the thresholded image. After processing with the median filter, a threshold was applied to the image to just the point where the damaged area began to "break up" and become distributed. This is illustrated in Figure 3. The threshold is started too low and slowly increased to just the point where the damage area "breaks up" as shown when the threshold is too high. At this boundary, the threshold is set for calculation of the damaged area. The area of the damaged region was calculated by a routine which simply counts non-thresholded pixels and multiplies that by the area of each pixel. The damaged area was then divided by the total area of the plate at that slice location to calculate the percent damage. Some images included the slug or a high-density region right at the center of the plate. In these cases, that area of the image was erased prior to calculating the damaged region so that those areas were not counted as non-damaged. Also, if damage was present outside of the circular damage zone (e.g pre-existing delaminations), this damage was not considered as damaged in the analysis.

A few issues should be noted when analyzing the images. These are subtle points but can be important when interpreting the images:

- A CT image is a representation of the X-ray attenuation coefficient in the slice plane. At 9-MeV, the X-ray attenuation is due almost entirely to density so for all intents and purposes, the CT image is a density map of the slice plane. If there are any damage states that would not result in a density change, the CT image will not detect it.
- Each slice is 2 mm thick meaning that it represents an average density of the plate through the 2 mm thickness.
- When defining the slice location, the convention used in this study is that the slice location represents the center of the 2 mm slice.
- The images do represent some beam hardening which is an image artifact which makes the outside of the plate appear as higher density than the center. The magnitude of the artifact can be determined from analyzing the control panel. In the future, this can be calibrated out of the images with some additional work, if desired.

#### V. DELIVERABLES

- CT Inspection Report
- 19 - 128-MB Optical Cartridges containing CT scan data and processed CT scan data
- 100 - 8" x 10" Polaroid photographs of selected slices

## **VI. PERSONNEL**

### **CT System Support**

Art McCarty, OO-ALC/TTWND (801) 777-6080

### **Image Analysis**

Robert N. Yancey, ARACOR (513) 427-5485

## **VIII. APPENDICES**

Appendix A: CT System Description

Appendix B: Technical Discussion of Images

Appendix C: Excel Data Summary Sheets for Each Panel

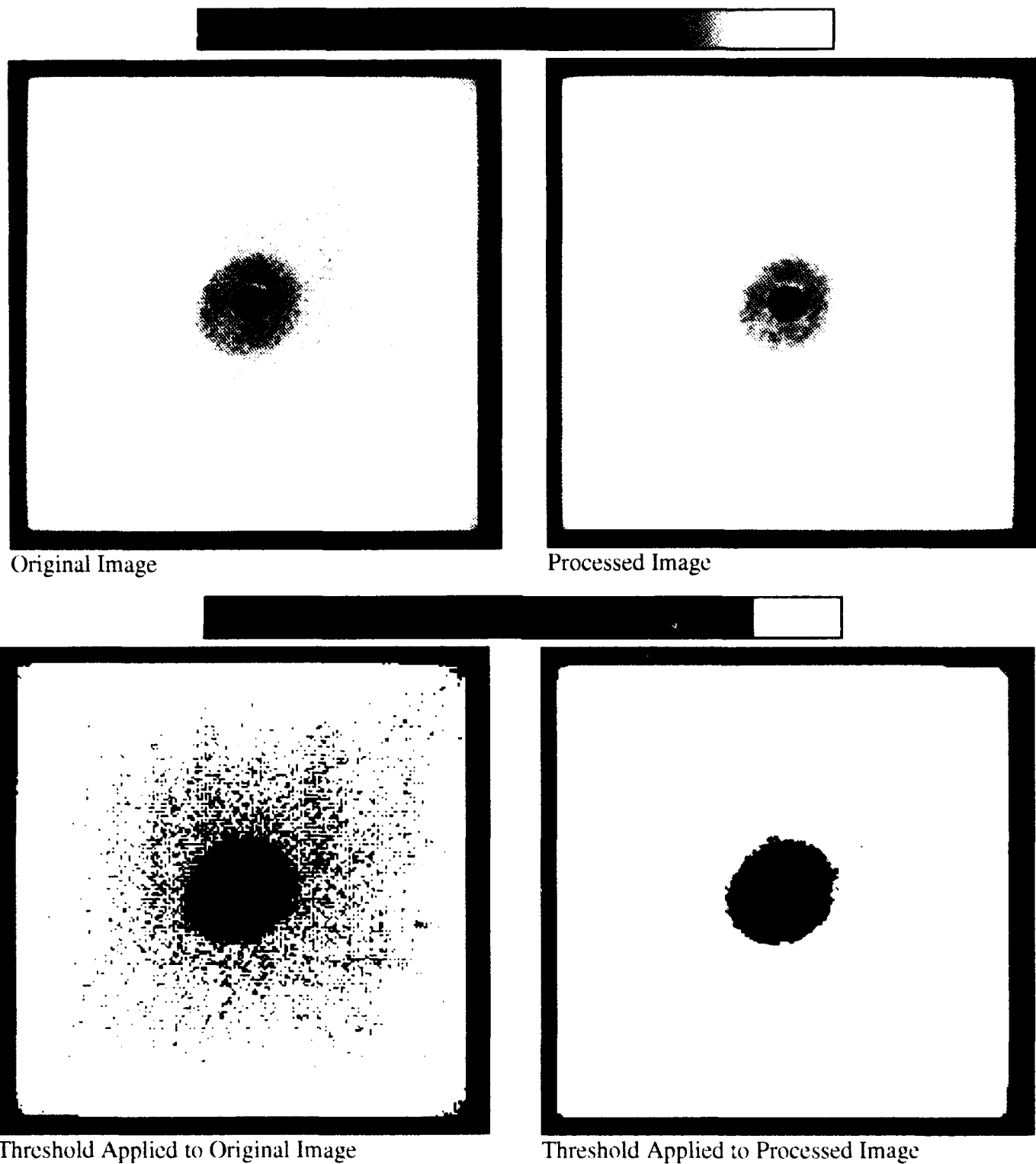
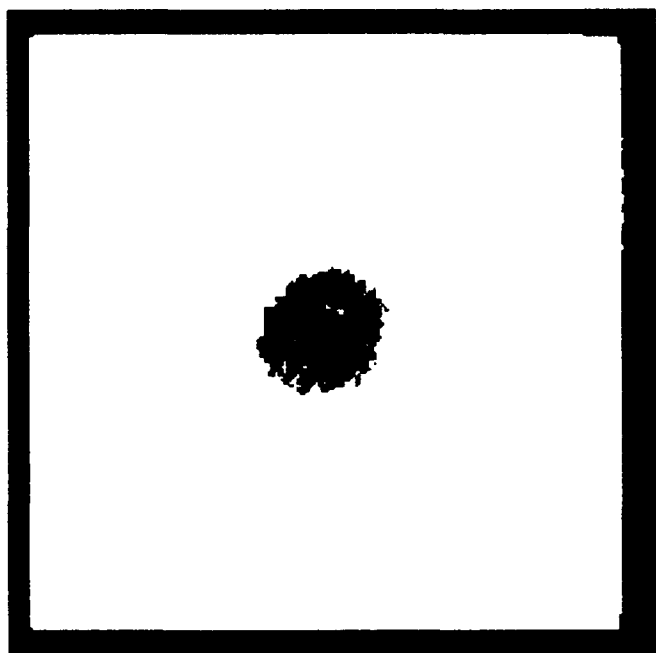
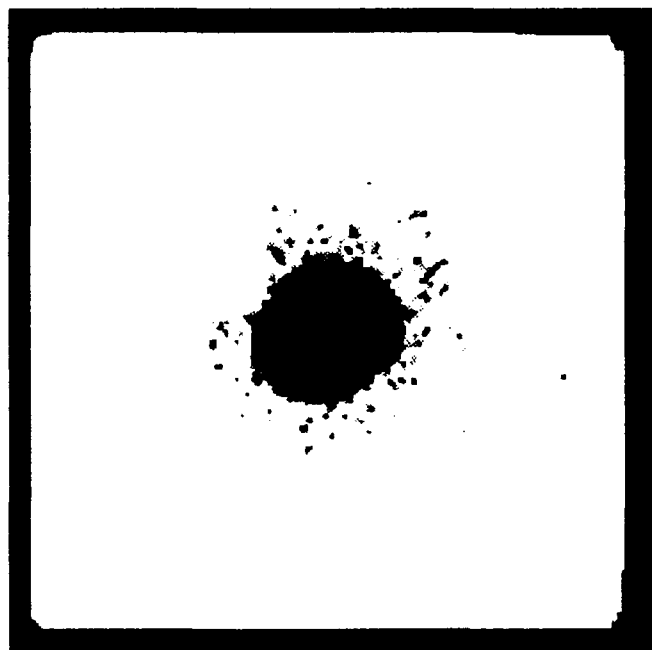


**FIGURE 2.** Processing Image Helps Hilight Damage Zone

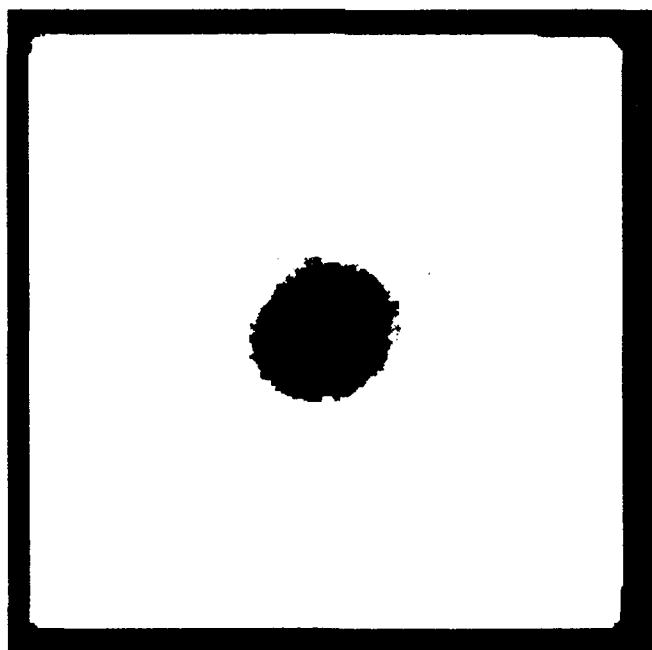




Threshold Too Low



Threshold Too High



Threshold Setting for Damage Calculation

**FIGURE 3.** Determining the Threshold Setting for Damage Calculation

## **APPENDIX A**

### **COMPUTED TOMOGRAPHY DESCRIPTION**

#### **CT SYSTEM DESCRIPTION**

The Hill AFB 9-MeV CT System installed at the Hill AFB, Ogden, UT was designed principally for the inspection of Minuteman rocket motor components. The Hill CT system has two modes of operation. First, conventional CT non destructively inspects the internal characteristics of a component at a specified area. Second, the system generates Digital Radiographic (DR) images that represent the through body radiographs of the object.

The Hill 9-MeV system is a second generation CT scanner that has been operational in its current configuration since 1989. Second-generation CT scanners obtain data by a translate-rotate technique. For a conventional CT scan, the component to be inspected is mounted on a turntable located between the X-ray source and detector array. The component translates past an X-ray energy source that transmits X-rays through the object in a horizontal plane. The component then rotates the fan beam angle between each traverse and repeats the traverse. This process is repeated until 180° worth of data are obtained (Figure A1).

The detector array measures attenuated beam strength and passes these measurements to a data acquisition computer where the data are pre-processed and arranged in a raw data set called a sinogram. Reconstruction software applies sophisticated mathematical algorithms (computed tomography) to the sinogram producing a cross-sectional image of the component scanned (Figure A2). The display subsystem allows display and analysis of the resulting reconstructed CT image.

The current system configuration allows for inspection of components with physical dimensions of 1500 mm in diameter, 2600 mm in height and up to 18,000 kgs in weight. The radiation source is a Varian Linear Accelerator capable of a maximum voltage of 9-MeV.

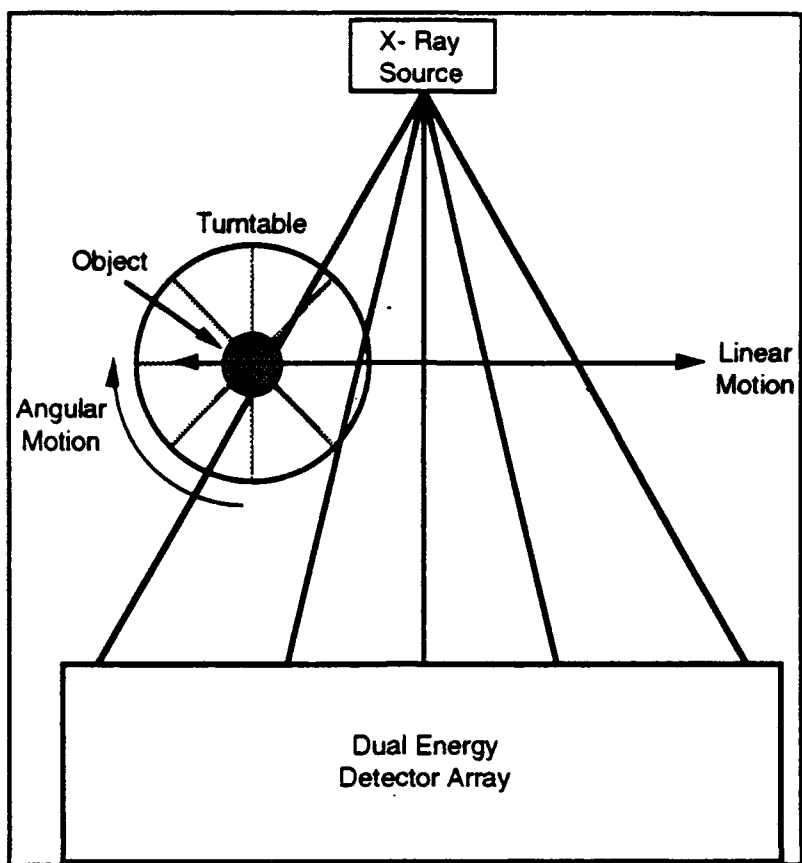


Figure A1

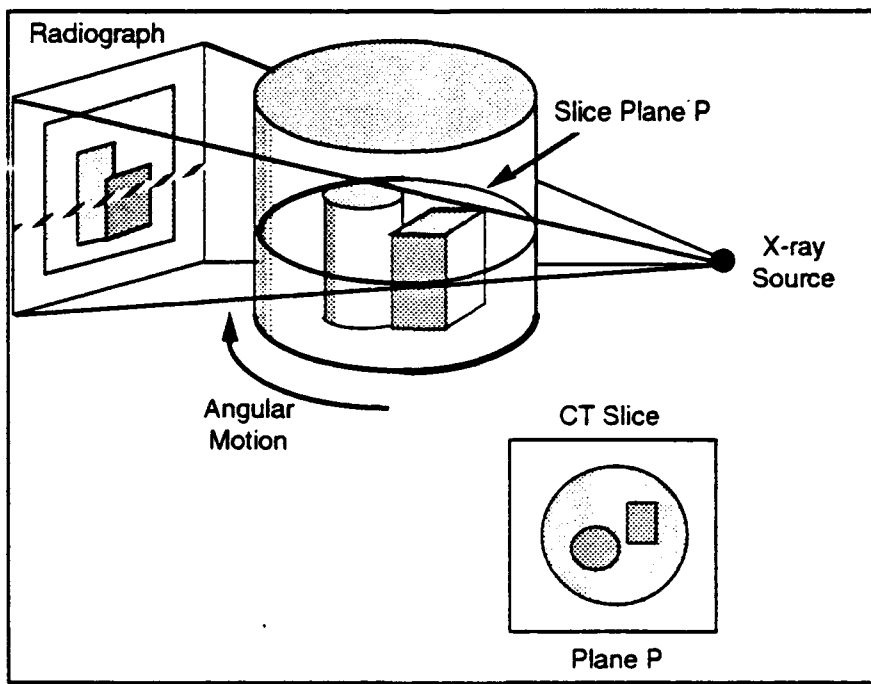


Figure A2

## APPENDIX B

### TECHNICAL DISCUSSION OF IMAGES

#### Photographs

The supplied photographs are reproductions of the images obtained from LAMDE. On the top left corner of the images is the image filename for the displayed image and the parameters for the inspection. The parameters on the left read as follows:

1. COLS/ROWS:	Matrix reconstruction size (in pixels)
2. X-SIZE/Y-SIZE	Field of View of the Inspection (in mm)
3. Z-GANT	Handling System Slice Height (in mm)
4. RES AP	Width of exposed detector (in mm)
5. THICK	Thickness of the slice collimator (in mm)
6. SLICE #	Slice number in sequence of scans
7. INTEG	Integration time in # of pulses
8. SCAN	Scan time in minutes
9. CTMIN	Minimum CT number in image
10. CTMAX	Maximum CT number in image

On the right side is a color bar legend that identifies the color for a range of CT values. Red corresponds to lower density and white corresponds to higher density. On the top (white) and bottom (red) of the color bar are numbers that correspond to the top and bottom of the scale respectively.

#### Viewing Images on the Macintosh

The CT images taken with this study have been loaded onto 128-MB optical cartridges. The CT image files are raw data files with no header information. Each image file is a 1024 x 1024 data set written as 16-bit signed integers with the bytes swapped in DEC order format. The images can be read into *NIH Image* using the import command under the **File** menu. In order to view the images in the same orientation as the images in the photographs, the images must be flipped vertically by using the Flip Vertical command under the **Edit** menu. The processed images have been flipped and rotated so that images will be oriented with the nylon rod at the bottom of each image.

For viewing in *DIP Station*, use the open command under the **File** menu and select the first slice image in the set. This will then bring up a dialog box where you set the rows and columns to 1024 each and enter the number of consecutive slices in the set. You should then choose the "By Pattern Rule" checkbox which will bring up another dialog box which should be set correctly. Click "OK" which returns you to the original dialog box. The Header info should be set to 0's and the Pixels should be set to "16-bit signed (byte swapped)" and the Alignment set to "None". Clicking "OK" will bring up the first image in the set. Like with *NIH Image*, to view the images in the same orientation as in the

photographs, the images need to be flipped vertically. Clicking the "+" or "-" buttons on the left of the image allows you to go to the next or previous slice respectively. Typing "s" will bring up a dialog box allowing you to go to any slice in the set. *DIP Station* is much faster than *NIH Image* and has much more flexibility. Any significant analysis of the images should be done with *DIP Station* which is sold by Hayden Image Processing Group in Colorado for approximately \$595. They can be reached at (303) 449-3433.

### **Label Files**

Included with the data files are label files for each slice. The label files are denoted by the "\$LA" suffix. The label files are ASCII files which contain information on the scan parameters and calibration constants used. Most of this information is not important for analysis of the data but a few parameters may be of interest. The first part of a sample label file is attached. Some of the parameters of interest are as follows:

COLUMNS	Number of columns of data in the image
ROWS	Number of rows of data in the image
INCCOL	Pixel width in millimeters
INCROW	Pixel height in millimeters
R_SCALE	Scale factor used to convert raw image values to CT number values. CT numbers correspond to density in milligrams per cubic centimeter. Raw image values should be divided by R_SCALE to calculate CT number values.
BEGSEC	Slice height location in millimeters
APERTURE	Resolution aperture setting in millimeters
THICK	Slice thickness aperture setting

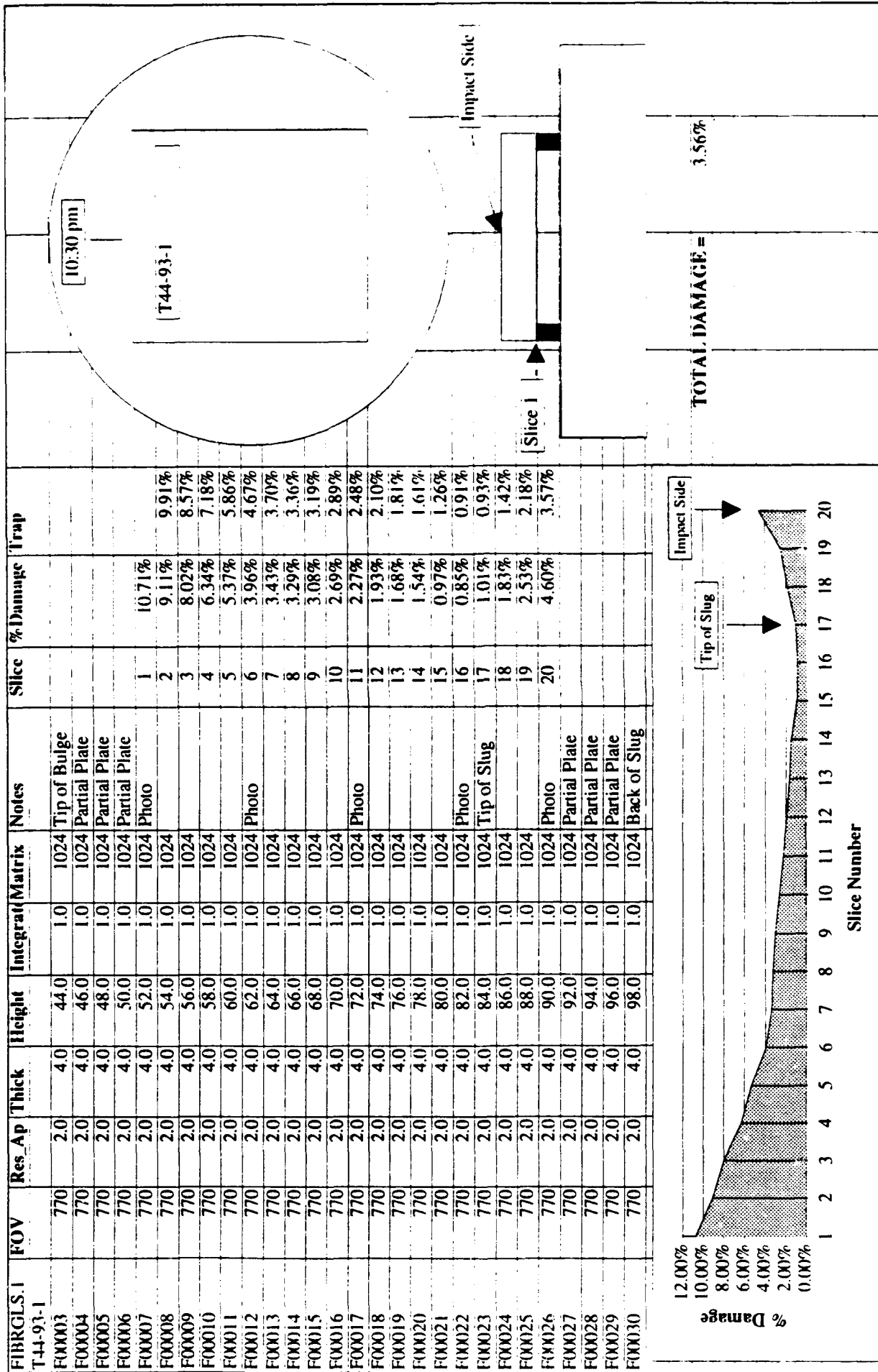
# SAMPLE LABEL FILE

```

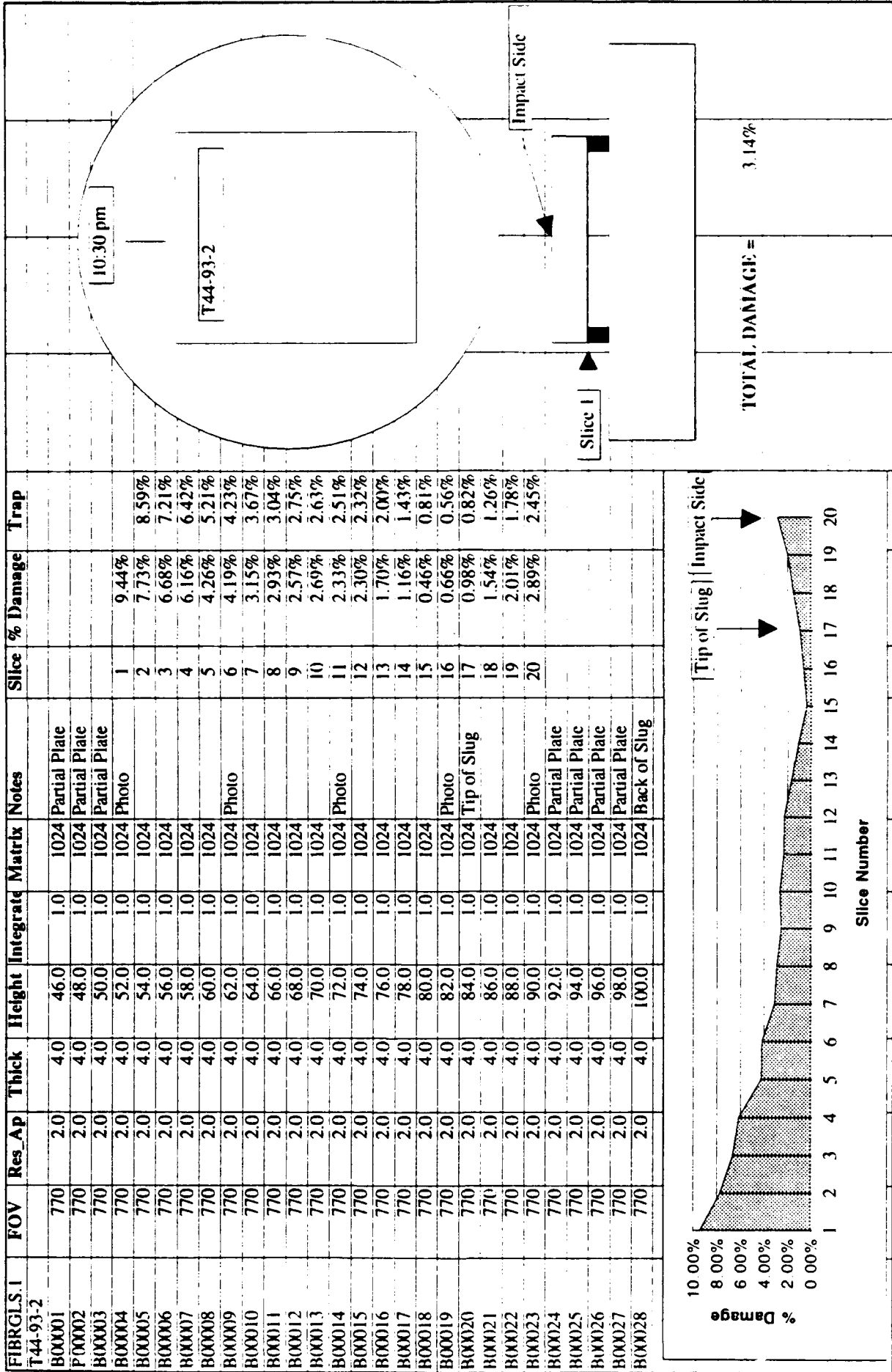
VERSION : 3
SITE :HILL9
MACHINE :ICT-1500
NIMHDR : 228
NSCHDR : 106
TITLE :FIBRGLS T27-93-2
TITLE :
TITLE :
PROGRAM :RECO
OPERAT :Reconstruction
IMTYPE :Reconstruction
RELATED :
X_UNITS :mm
Y_UNITS :Degrees
Z_UNITS :mm
R_UNITS :CT Numbers
DATE :16-AUG-1993
TIME :09:38:36.92
COLUMNS : 1024
ROWS : 1024
SECTIONS: 1
COLREC : 2
ROWREC : 1024
SECREC : 784
BEGCOL : -385.3764
BEGROW : -385.3764
BEGSEC : 54.00000
INCCOL : 0.7526882
INCROW : 0.7526882
INCSEC : 4.000000
R_SCALE : 8.000000
Z_REFRNC: 0.00000000E+00
NCAL : 0
N_DET : 112
N_TRAV : 7
SERIES : 10
KV : 420
MA : 4
MSEC : 4.081633
APERTURE: 2.000000
SPOT : 1.500000
THICK : 4.000000
NTRIG : 1
LOLEV : -4545
HILEV : 17077

```

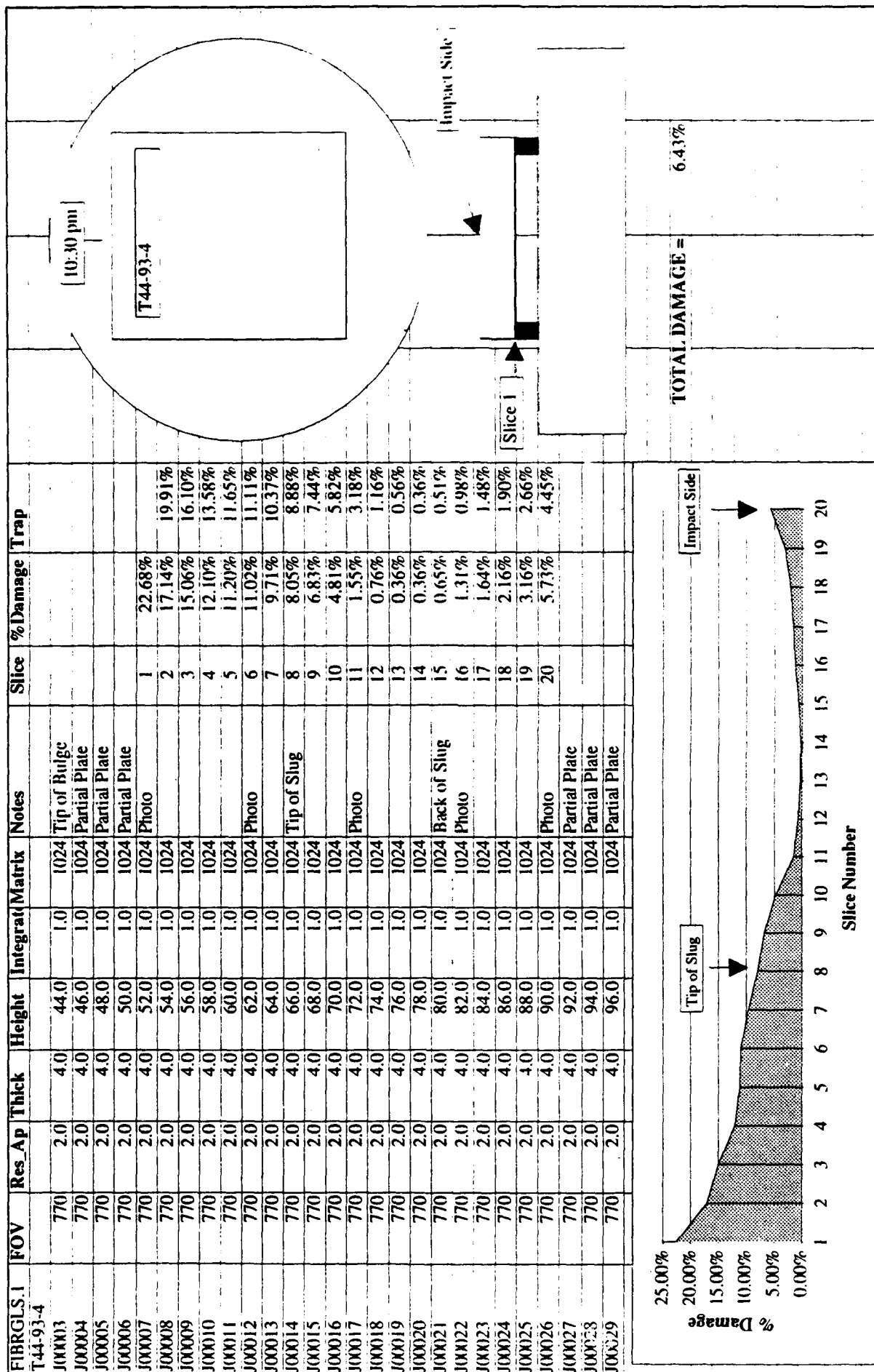
**APPENDIX C**  
**EXCEL DATA SUMMARY SHEETS**

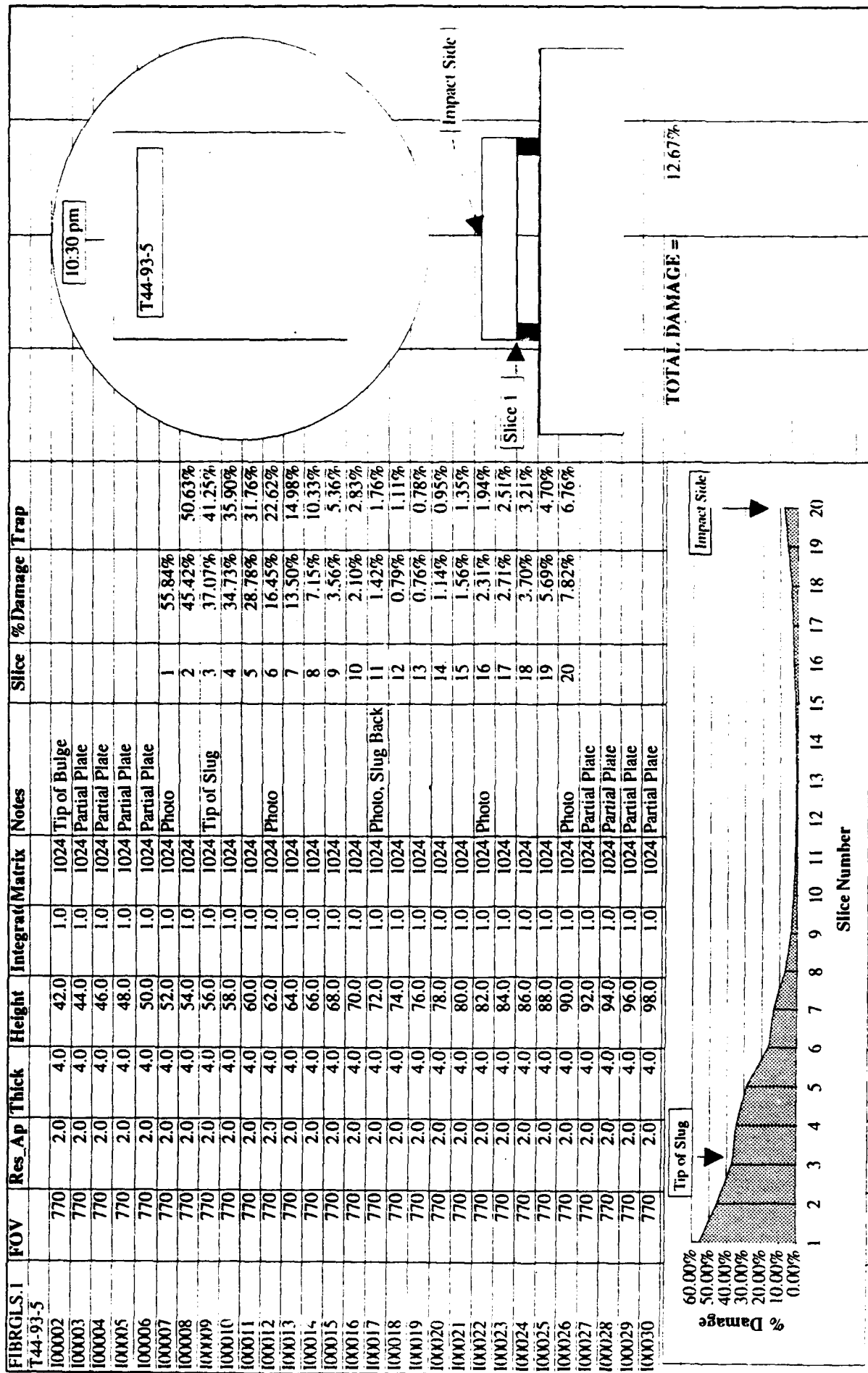


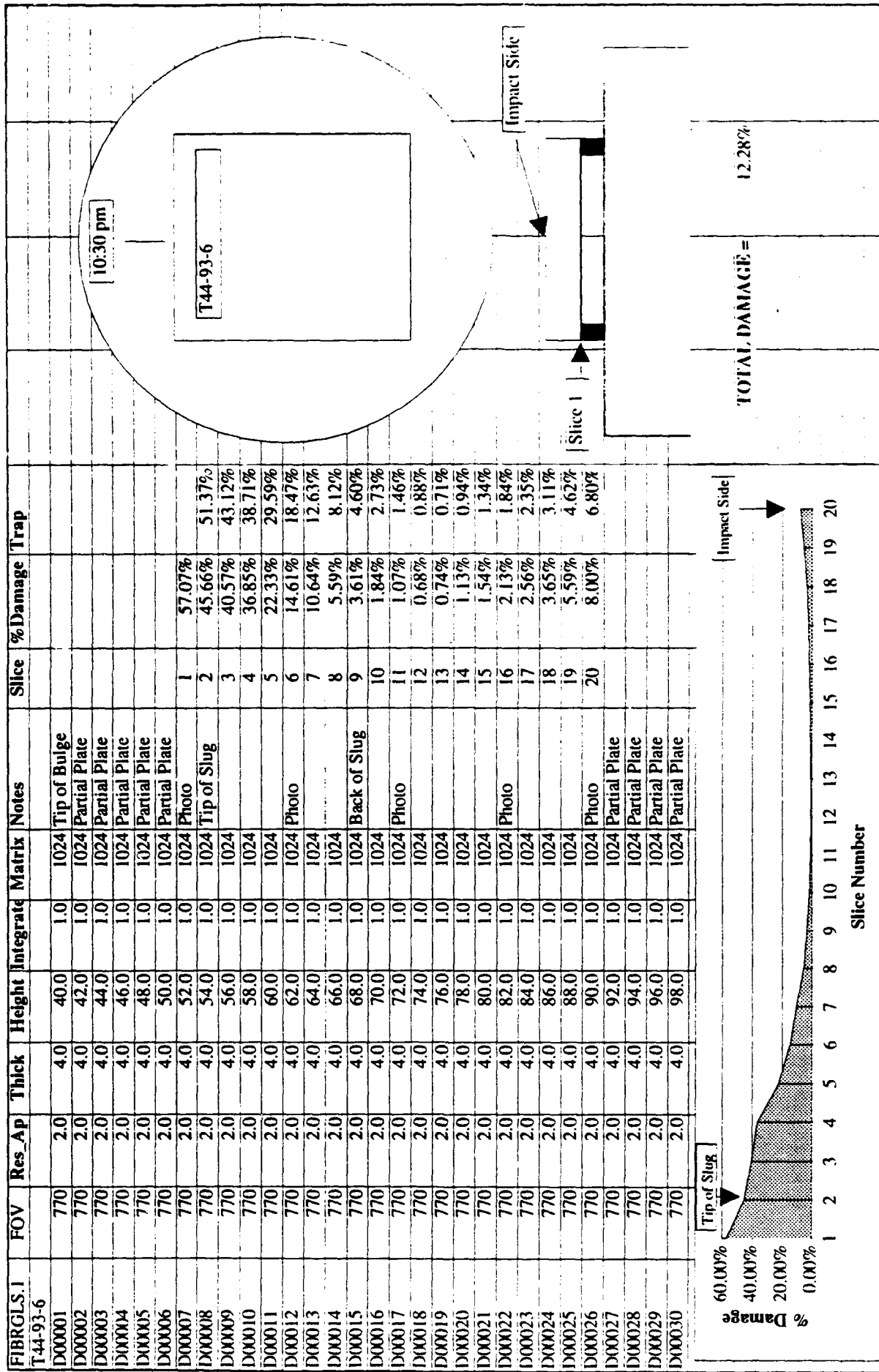


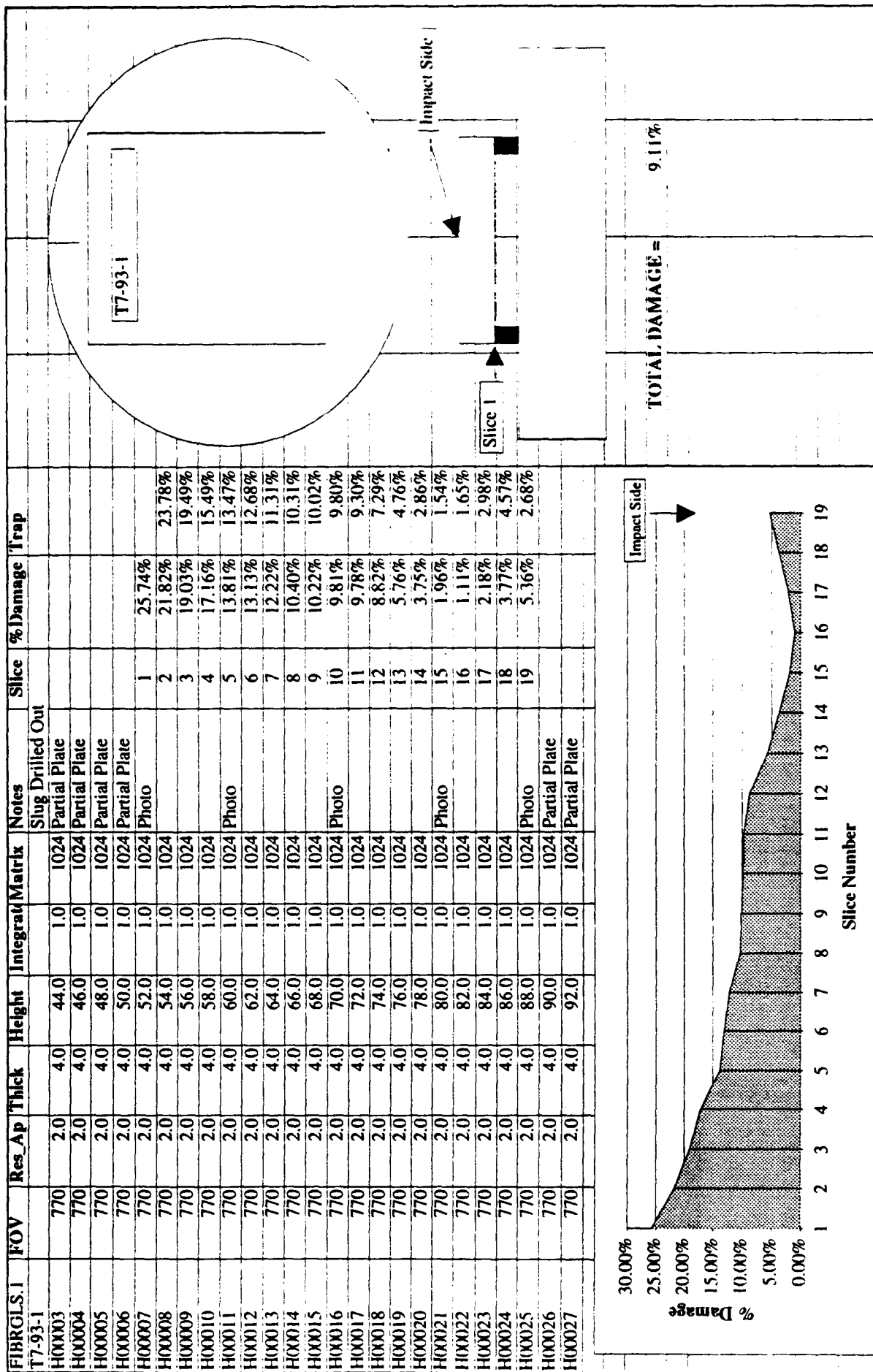


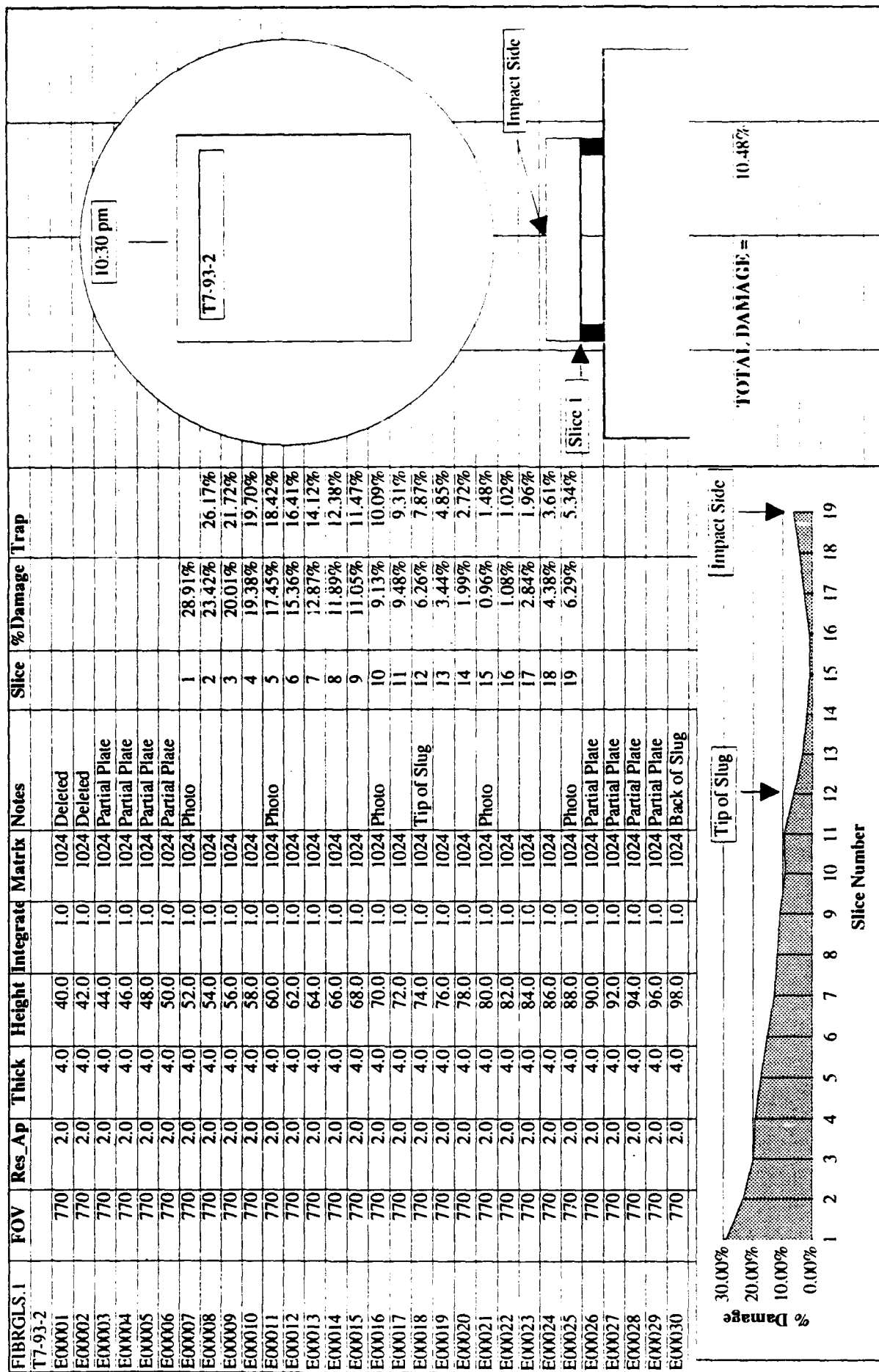


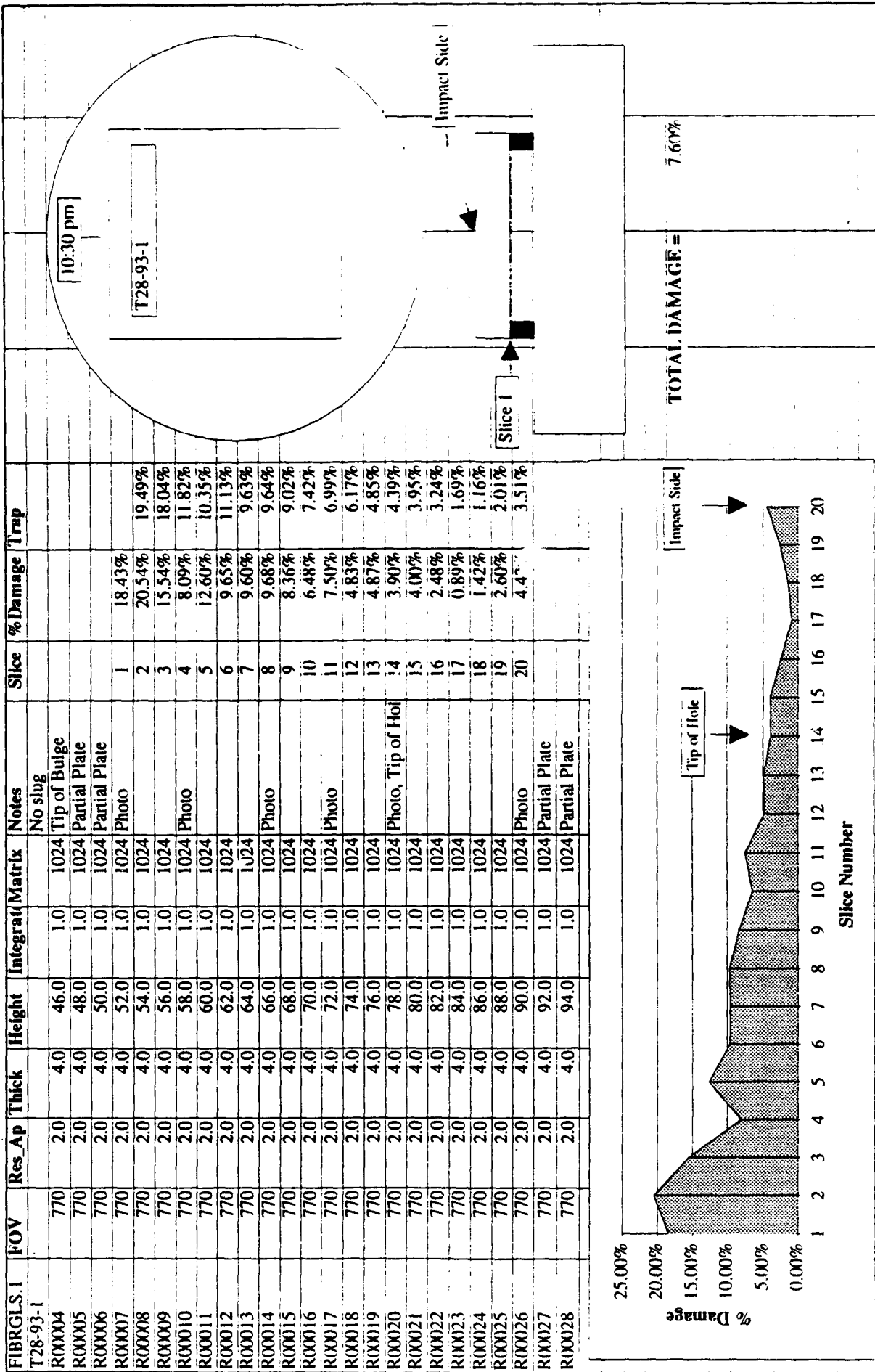




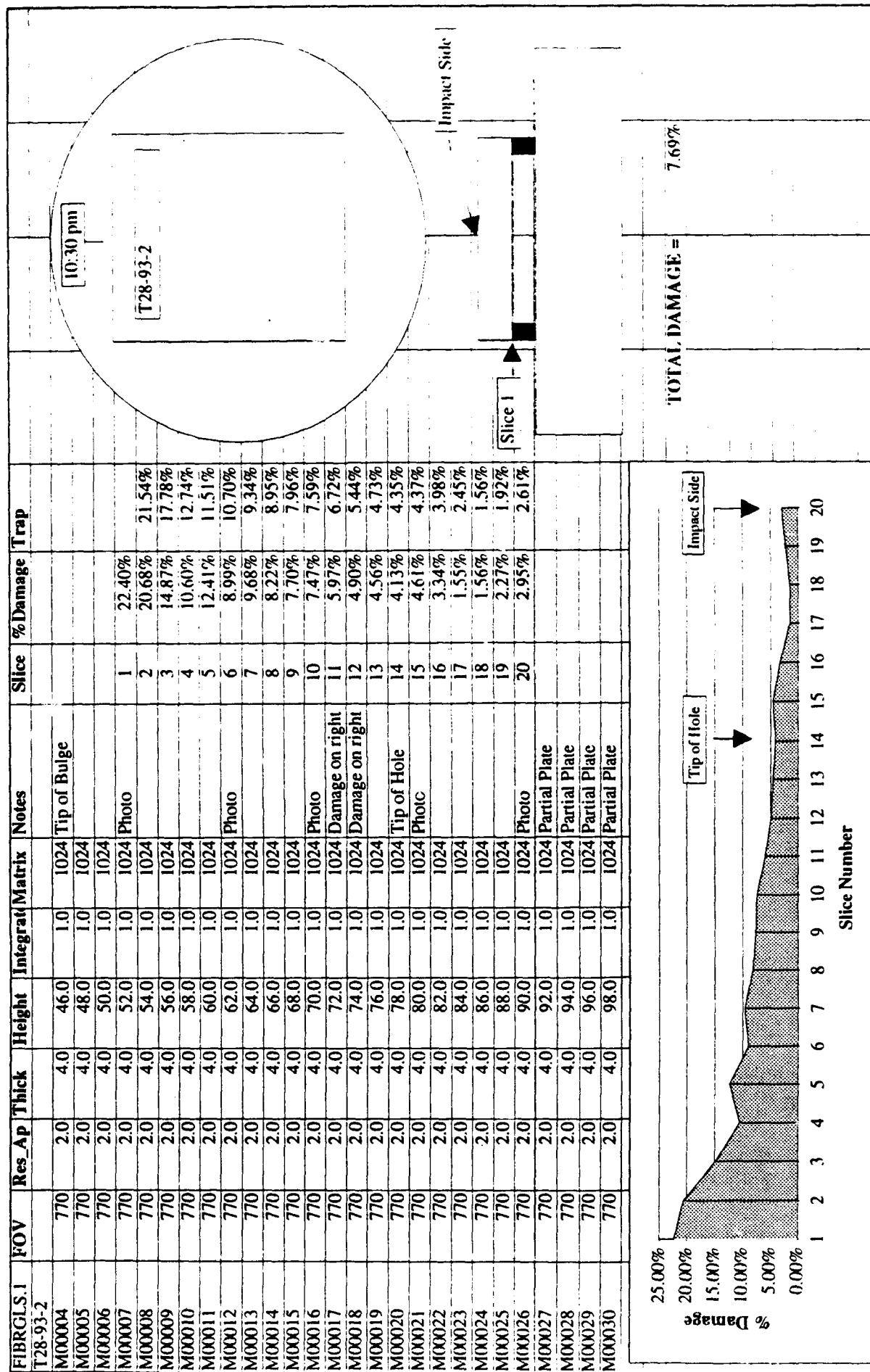


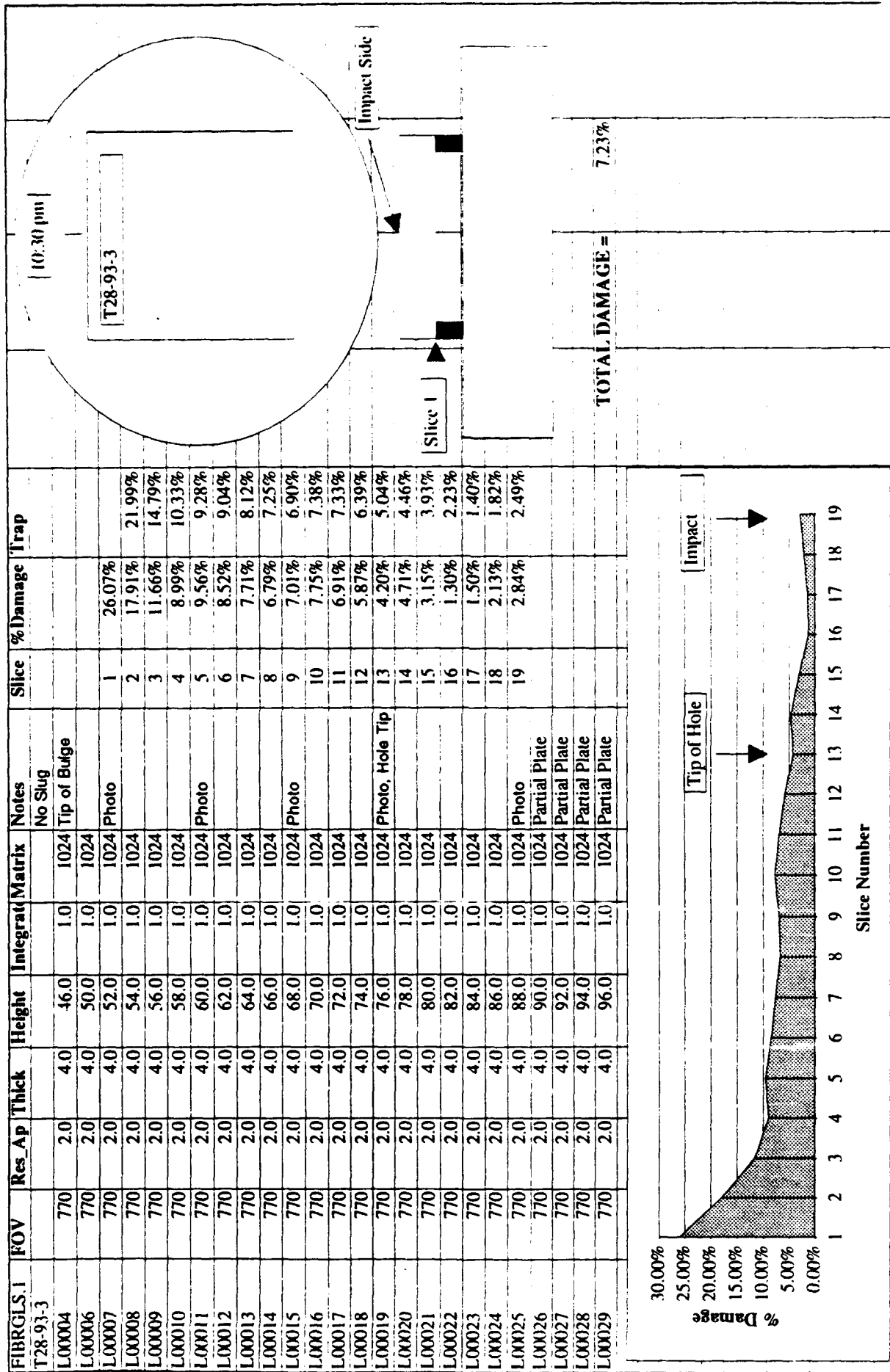


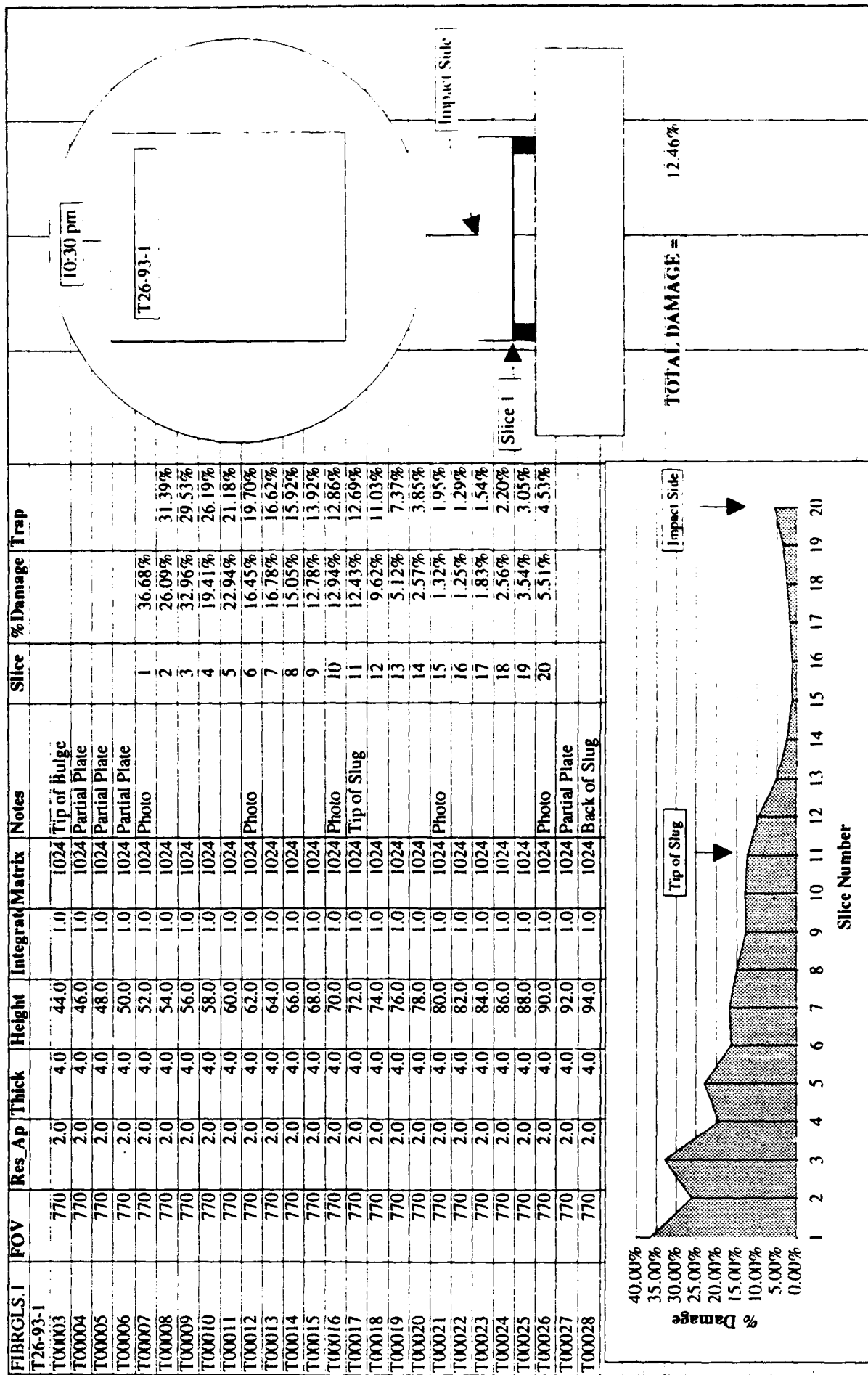


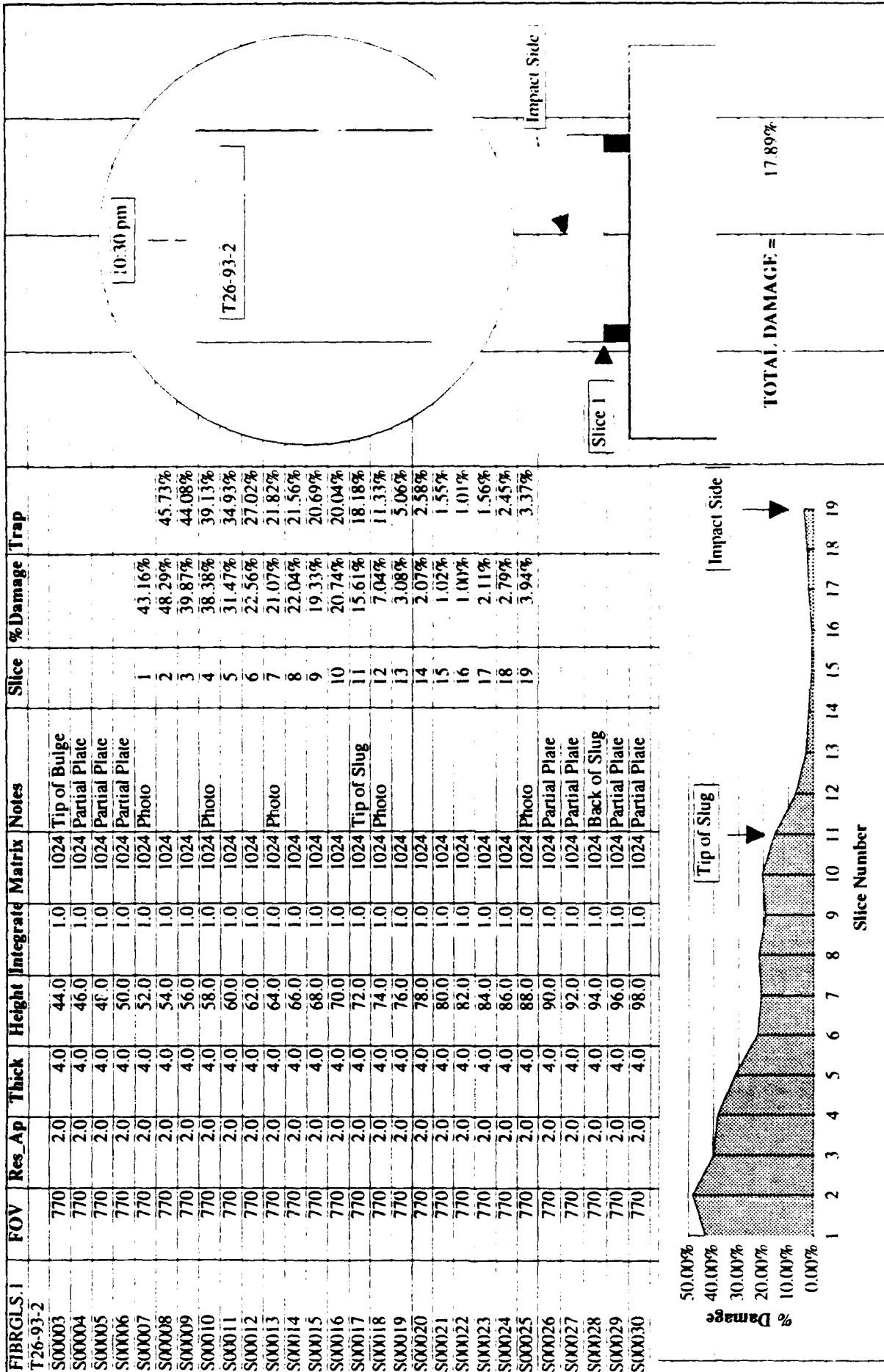


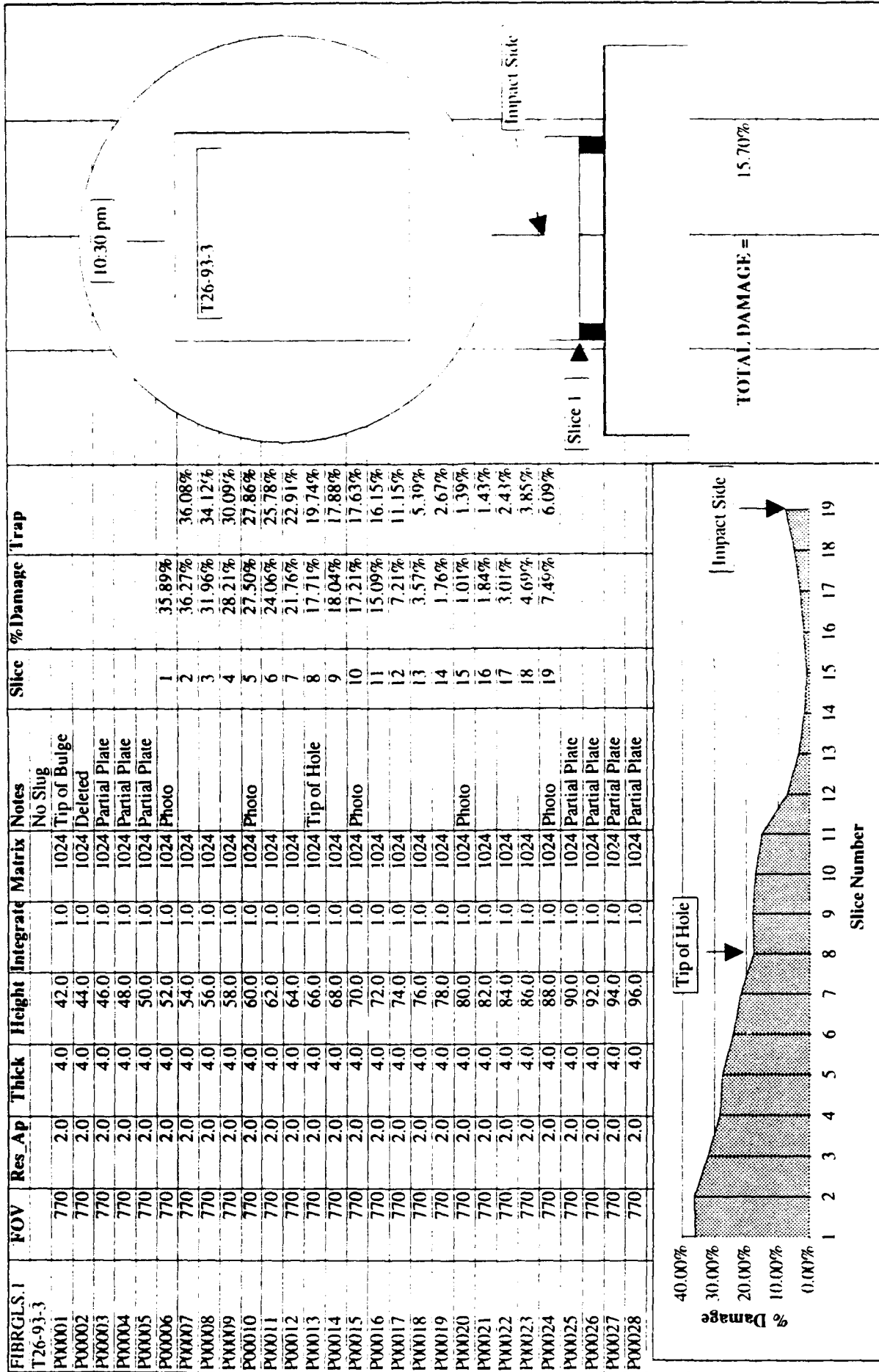




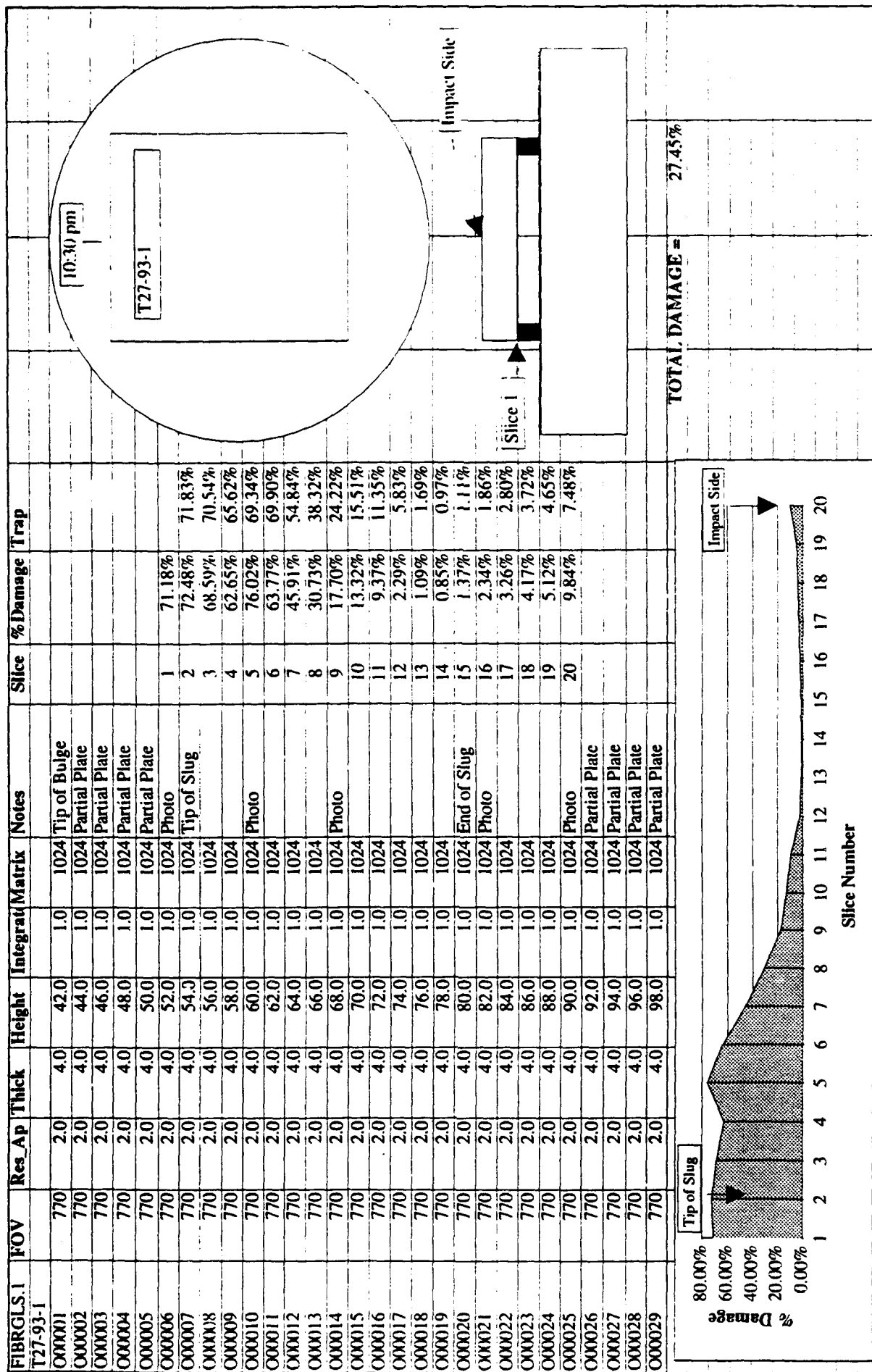


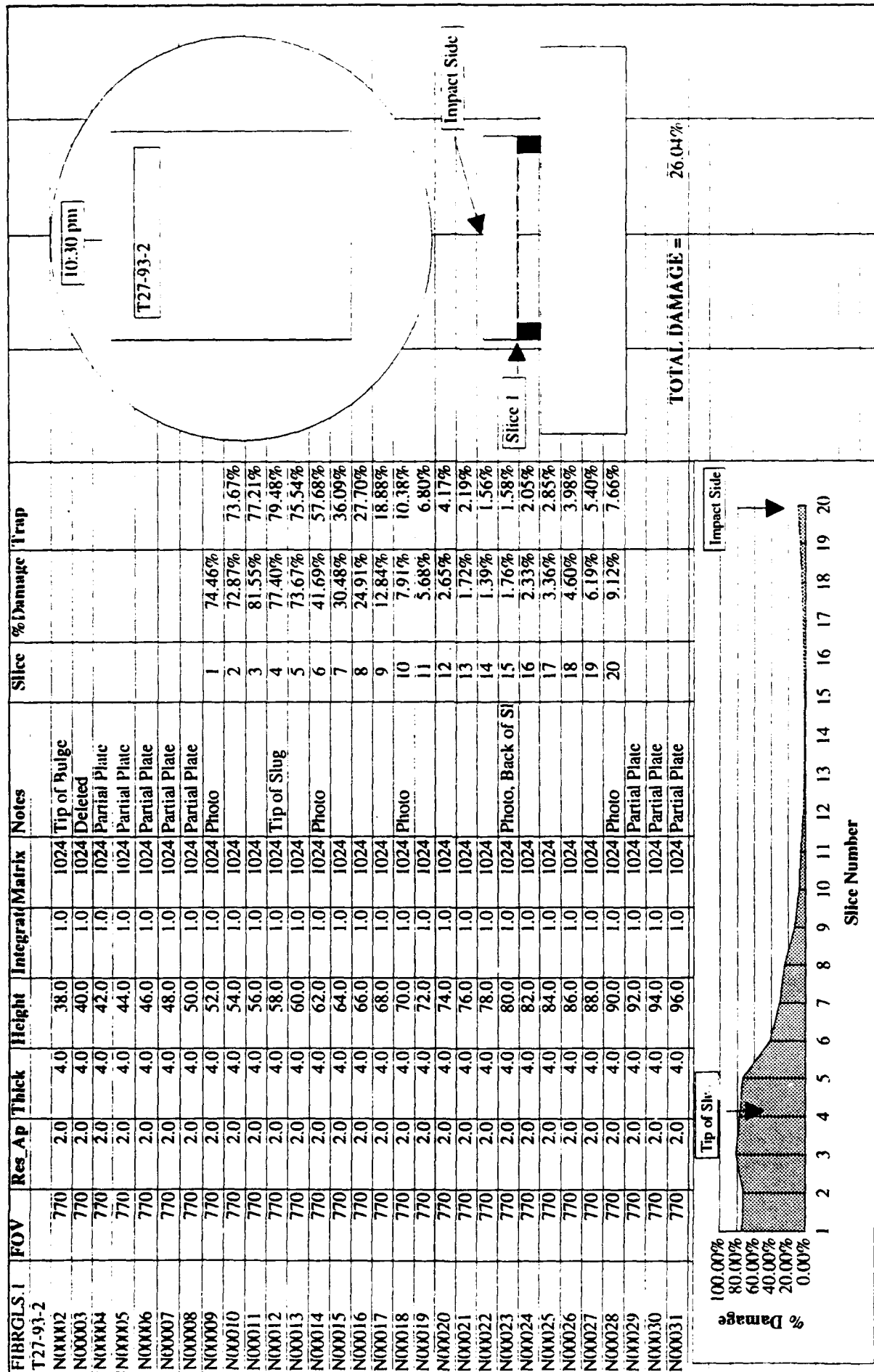


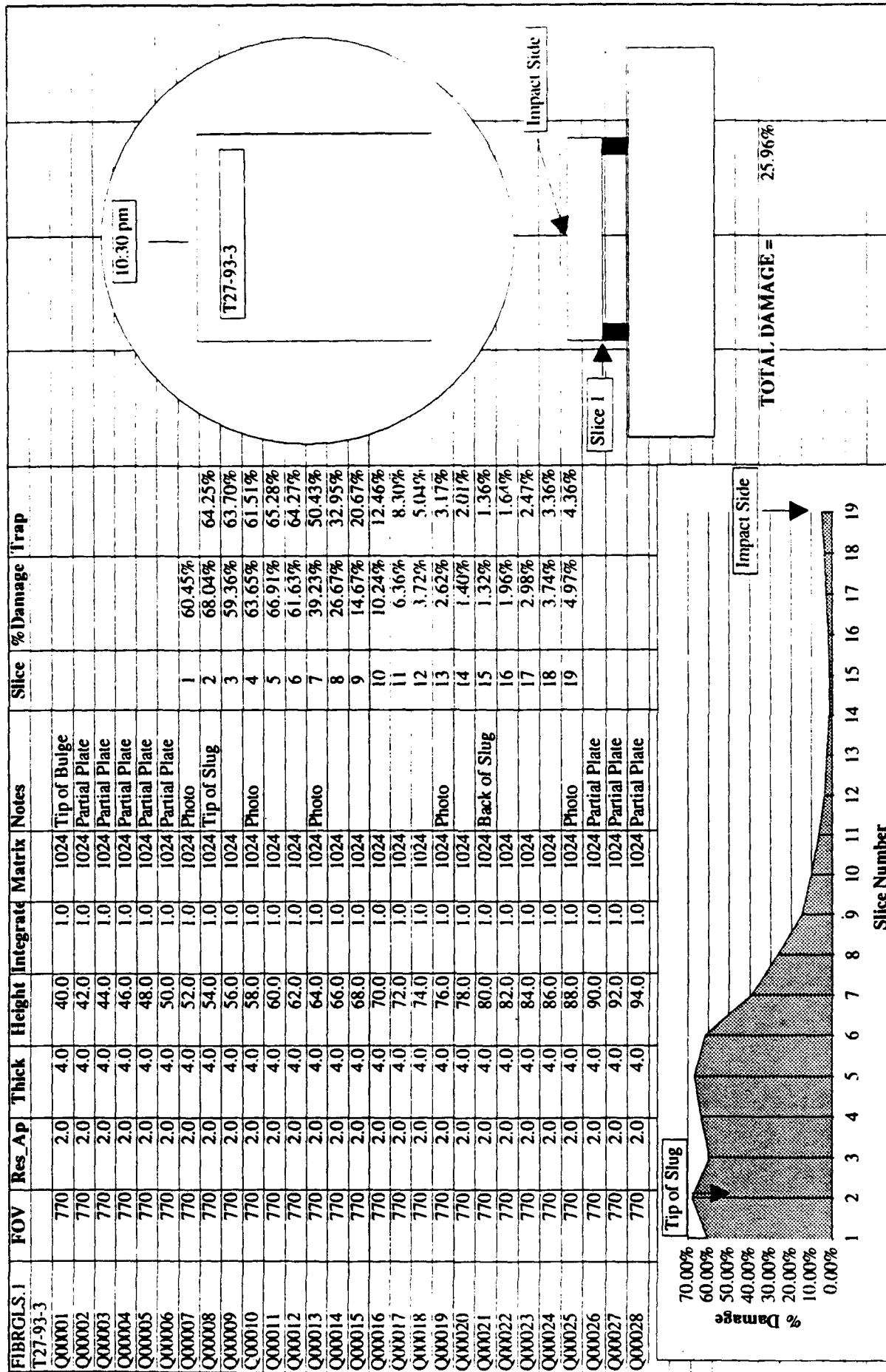




TOTAL DAMAGE = 15.70%

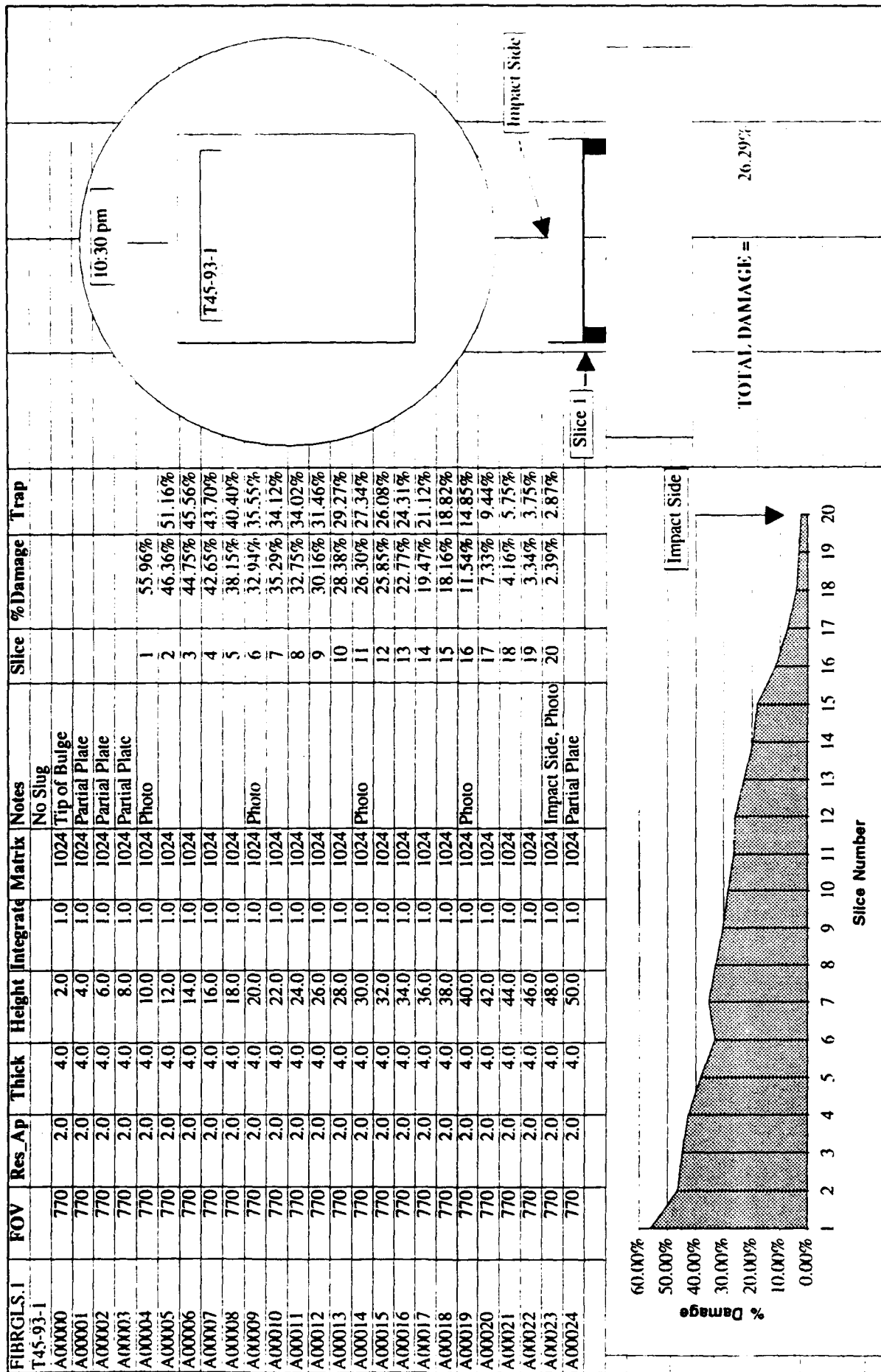








A-T45-93-1 Panel

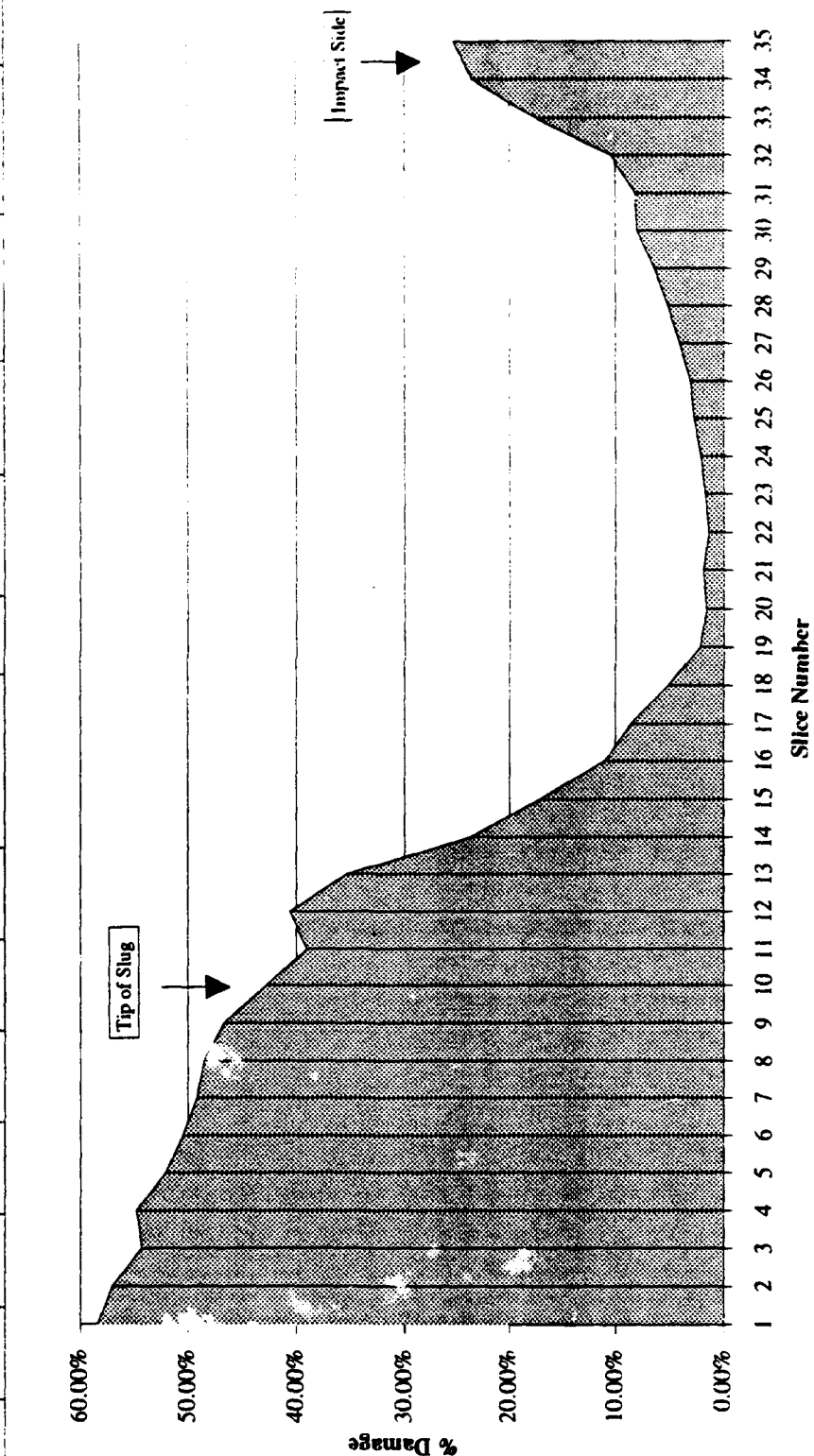


FIBRGLS.1	FOV	Res.Ap	Thick	Height	Integrat	Matrix	Notes	Slice	%Damage	Trap
T45-93-2										
G00002	870	2.0	4.0	37.0	1.0	1024	Tip of Bulge			
G00003	870	2.0	4.0	39.0	1.0	1024	Partial Plate			
G00004	870	2.0	4.0	41.0	1.0	1024	Partial Plate			
G00005	870	2.0	4.0	43.0	1.0	1024	Partial Plate			
G00006	870	2.0	4.0	45.0	1.0	1024	Partial Plate			
G00007	870	2.0	4.0	47.0	1.0	1024	Partial Plate			
G00008	870	2.0	4.0	49.0	1.0	1024	Partial Plate			
G00009	870	2.0	4.0	51.0	1.0	1024	Photo	1	58.40%	
G00010	870	2.0	4.0	53.0	1.0	1024		2	57.07%	57.74%
G00011	870	2.0	4.0	55.0	1.0	1024		3	54.31%	55.69%
G00012	870	2.0	4.0	57.0	1.0	1024		4	51.82%	54.57%
G00013	870	2.0	4.0	59.0	1.0	1024		5	2.08%	53.45%
G00014	870	2.0	4.0	61.0	1.0	1024		6	50.49%	51.29%
G00015	870	2.0	4.0	63.0	1.0	1024		7	49.23%	49.86%
G00016	870	2.0	4.0	65.0	1.0	1024		8	48.57%	48.90%
G00017	870	2.0	4.0	67.0	1.0	1024	Photo	9	46.69%	47.63%
G00018	870	2.0	4.0	69.0	1.0	1024	Photo, Slug Tip	10	42.83%	44.76%
G00019	870	2.0	4.0	71.0	1.0	1024		11	39.07%	40.95%
G00020	870	2.0	4.0	73.0	1.0	1024		12	40.64%	39.86%
G00021	870	2.0	4.0	75.0	1.0	1024		13	35.35%	38.00%
G00022	870	2.0	4.0	77.0	1.0	1024		14	23.76%	29.56%
G00023	870	2.0	4.0	79.0	1.0	1024		15	17.21%	20.49%
G00024	870	2.0	4.0	81.0	1.0	1024		16	11.01%	14.11%
G00025	870	2.0	4.0	83.0	1.0	1024		17	8.60%	9.81%
G00026	870	2.0	4.0	85.0	1.0	1024	Photo	18	5.14%	6.87%
G00027	870	2.0	4.0	87.0	1.0	1024		19	2.24%	3.69%
G00028	870	2.0	4.0	89.0	1.0	1024	Back of Slug	20	1.64%	1.94%
G00029	870	2.0	4.0	91.0	1.0	1024		21	1.93%	1.79%
G00030	870	2.0	4.0	93.0	1.0	1024		22	1.43%	1.68%
G00031	870	2.0	4.0	95.0	1.0	1024		23	1.75%	1.59%
G00032	870	2.0	4.0	97.0	1.0	1024		24	2.17%	1.96%
G00033	870	2.0	4.0	99.0	1.0	1024		25	2.76%	2.47%
G00034	870	2.0	4.0	101.0	1.0	1024		26	3.13%	2.95%
G00035	870	2.0	4.0	103.0	1.0	1024	Photo	27	4.13%	3.63%
G00036	870	2.0	4.0	105.0	1.0	1024		28	5.19%	4.66%
G00037	870	2.0	4.0	107.0	1.0	1024		29	6.43%	5.81%
G00038	870	2.0	4.0	109.0	1.0	1024		30	8.03%	7.23%
G00039	870	2.0	4.0	111.0	1.0	1024		31	8.19%	8.11%
G00040	870	2.0	4.0	113.0	1.0	1024		32	10.48%	9.34%
TOTAL DAMAGE =									22.93%	

10:30 pm

T45-93-2

G00041	870	2.0	4.0	115.0	1.0	1024		33	17.63%	14.06%	
G00042	870	2.0	4.0	117.0	1.0	1024		34	23.63%	20.63%	
G00043	870	2.0	4.0	119.0	1.0	1024	Photo	35	25.43%	24.53%	
G00044	870	2.0	4.0	121.0	1.0	1024	Partial Plate				
G00045	870	2.0	4.0	123.0	1.0	1024	Partial Plate				
G00046	870	2.0	4.0	125.0	1.0	1024	Partial Plate				
G00047	870	2.0	4.0	127.0	1.0	1024	Partial Plate				



# DISTRIBUTION LIST

No. of  
Copies

To

1 Office of the Under Secretary of Defense for Research and Engineering,  
The Pentagon, Washington, DC 20301

Director, U.S. Army Research Laboratory, 2800 Powder Mill Road,  
Adelphi, MD 20783-1145

1 ATTN: AMSRL-OP-CI-AD, Technical Publishing Branch  
AMSRL-OP-CI-AD, Records Management Administrator  
AMSRL-SS

Commander, Defense Technical Information Center, Cameron Station,  
Building 5, 5010 Duke Street, Alexandria, VA 22304-6145

2 ATTN: DTIC-FDAC

Commander, Army Research Office, P.O. Box 12211, Research Triangle  
Park, NC 27709-2211

1 ATTN: Office of Research and Technology Integration AMXRO-RT

1 Dr. Andrew Crowson, AMXRO-MS

1 Dr. Kailasam Iyer, AMXRO-MS

1 Dr. Gary Anderson, AMXRO-EN

Commander, U.S. Army Materiel Command, 5001 Eisenhower Avenue,  
Alexandria, VA 22333-0001

1 ATTN: AMCSCI, Dr. R. Chait

Commander, U.S. Army Materiel Systems Analysis Activity, Aberdeen  
Proving Ground, MD 21005

1 ATTN: AMXSY-CR

1 AMXSY-RM

Commander, U.S. Army Missile Command, Redstone Arsenal, AL 35809

1 ATTN: AMSMI-RD-ST, Dr. L.C. Mixon

Commander, U.S. Army Armament, Research, Development and Engineering  
Center, Picatinny Arsenal, NJ 07806-5000

1 ATTN: SMCAR-AET, Dr. W. Ebihara

Commander, U.S. Army Natick Research, Development and Engineering  
Center, Natick, MA 01760-5010

1 ATTN: Technical Library

1 STRNC-ICA, R.F. Kinney

Commander, U.S. Army Tank-Automotive Command, Warren, MI 48397-5000

1 ATTN: AMSTA-ZE

1 AMSTA-TSL, Technical Library

1 AMSTA-RSK, Samuel Goodman

1 AMSTA-RS, J. Thompson

1 AMSTA-RTC, R.A. Brynsvald

1 AMSTA-RTC, S. Kramer

1 AMSTA-RTC, D. Ostberg

1 AMSTA-RTC, L. Hinojosa

No. of  
Copies

To

1 Commander, White Sands Missile Range, NM 88002-5000  
ATTN: AMSRL-VA-DV, J.J. Wade  
(SLCVA-DV)

1 Director, U.S. Army Research Laboratory, Aberdeen Proving Ground, MD  
21005-5066  
ATTN: AMSRL-WT, Dr. J. Fraiser  
1 AMSRL-WT-TA, W. Gooch  
1 AMSRL-WT-TA, G.L. Filbey, Jr.  
1 AMSRL-WT-TC, W. de Rosset  
1 AMSRL-WT-TD, Thomas W. Wright  
1 AMSRL-WT-PD, B. Burns  
1 AMSRL-WT-WA, B.R. Moore

1 Director, Defense Intelligence Agency, Washington, DC 20340-6053  
ATTN: ODT-5A (Mr. Frank Jaeger)

1 Air Force Armament Laboratory, Eglin Air Force Base, FL 32542-5434  
ATTN: J.C. Foster, Jr., AFATL/DLJW  
1 W.H. Cook, AFATL/DLJW

1 Naval Post Graduate School, Monterey, CA 93943-5100, Dept. of  
Aeronautics  
ATTN: Prof. E.M. Wu, Code NC4 (67WT)

1 Naval Research Laboratory  
ATTN: Dr. R. Badalian, Code 6380, Washington, DC 20375

1 Naval Surface Warfare Center, Silver Spring, MD 20903-5000  
ATTN: F.J. Zerilli, Code R13  
1 R.H. Garrett, Jr.

1 Southwest Research Institute, 6220 Culebra Road, San Antonio,  
TX 78238  
ATTN: Dr. C.E. Anderson

1 Director, Benet Weapons Laboratory, Army Armament RDE Center,  
Watervliet, NY 12189-4050  
ATTN: SMCAR-CCB, Dr. W. Kitchens  
1 SMCAR-CCB, Dr. J. Vasilakis

1 Commander, U.S. Army Foreign Science and Technology Center, 220 7th  
Street, N.E., Charlottesville, VA 22901-5396  
ATTN: AIFRTC, Applied Technologies Branch, Gerald Schlesinger

1 Commandant, U.S. Army Quartermaster School, Fort Lee, VA 23801  
ATTN: Quartermaster School Library

1 Materials Directorate, Wright Laboratory, Wright-Patterson Air Force  
Base, OH 45433-7718  
ATTN: WL/MLSA, Mr. W.E. Berner, (Bldg. 652)

1 Committee on Marine Structures, Marine Board, National Research  
Council, 2101 Constitution Avenue, NW, Washington, DC 20418

No. of  
Copies

To

Plastics Technical Evaluation Center, PLASTEC, ARDEC, Bldg. 355N,  
Picatinny Arsenal, NJ 07806-5000

1 ATTN: Harry Pebly

Department of the Army, Vehicle Structures Directorate, MS-266,  
Langley Research Center, Hampton, VA 23665-5225

1 ATTN: AMSRL-VS, W. Elber  
1 AMSRL-VS-S, F. Bartlett  
1 AMSRL-VS-S, G.L. Farley  
1 AMSRL-VS-S, K. O'Brien  
1 AMSRL-VS-L, J. Pritchard

RARDE, Fort Halstead - Sevenoaks, TN14 7BP Kent, England

1 ATTN: Dr. Phillip Church

Department of FV&S7, DRA (Chertsey), Chobham Lane, Chertsey, Surrey,  
KT16 0EE, England

1 ATTN: Dr. Anthony Hawkins  
1 Dr. I.G. Crouch  
1 Dr. L.T. Greaves

Institute for Advanced Technology, 4030-2 West Braker,  
Austin, TX 78759-5329

1 ATTN: Stephen Bless

University of Dayton, Building JPC 201, Dayton, OH 45469

1 ATTN: Mr. David J. Grove

Sandia National Laboratories, P.O. Box 5800, Albuquerque, NM 87185

1 ATTN: E.P. Chen, Div 1561  
1 P. Yarrington, Div 1533

ARPA/Materials Science Office, 1400 Wilson Boulevard,  
Arlington, VA 22209-2308

1 ATTN: B. Wilcox

ARPA/TTO, 3701 North Fairfax Drive, Arlington, VA 22203-1714

1 ATTN: Robert Kocher

Director, U.S. Army Research Laboratory, Watertown, MA 02172-0001

2 ATTN: AMSRL-OP-WT-IS, Technical Library  
10 AMSRL-MA-PD, E. DeLuca